Characterizing Infrared Excess Sources in the Galactic Center with Adaptive Optics

Sitarski, Breann Nicole

2016

University of California
Los Angeles

Characterizing Infrared Excess Sources in the Galactic Center with Adaptive Optics

A dissertation submitted in partial satisfaction
of the requirements for the degree
Doctor of Philosophy in Astronomy

by

Breann Nicole Sitarski

2016

Abstract of the Dissertation

Characterizing Infrared Excess Sources in the Galactic Center with Adaptive Optics

by

Breann Nicole Sitarski

Doctor of Philosophy in Astronomy

University of California, Los Angeles, 2016

Professor Andrea M. Ghez, Chair

This thesis presents Adaptive Optics (AO) imaging and spectroscopic measurements of infrared excess sources in the Galactic Center to determine if they are similar to G2, the first example of a spatially-resolved object interacting with the supermassive black hole at the center of the Galaxy, Sgr A*. Our goal is to understand the debated nature of these infrared excess sources and to understand their relationship with the supermassive black hole. Our objects have been monitored with AO from he past decade (2004 - 2015) and are within the inner $1\farcs75$ of the supermassive black hole.

We initially focus on one source, G1, which gets comparably close to the supermassive black hole compared to G2 ($a_{min} \sim 200 - 300$ AU) and lies on a very eccentric orbit ($e_{G1} = 0.99$). While G2 has been tracked before and during periapse passage ($T_0 \sim 2014.2$), G1 has been followed since soon after emerging from periapse ($T_0 \sim 2001.3$). Our observations of G1 double the previously reported observational time baseline, which improves its orbital parameter determinations. G1's orbital trajectory appears to be in the same plane as that of G2, but with a significantly different argument of periapse ($\Delta\omega = 21\pm4$ degrees). This suggests that G1 is an independent object and not part of a gas stream containing G2 as has been proposed. Furthermore, we show for the first time that: (1) G1 is extended in the early epochs (those closest to periapse) along the direction of orbital motion and (2) G1 becomes significantly smaller over time, changing from 450 AU in 2004 to less than 170 AU in 2009 and thereafter. Based on these observations, G1 appears to be the second example of an object tidally interacting with a supermassive black hole. G1's continued survival 14 years after periapse, along with its compactness in epochs further from the time of periapse, suggests that this source is stellar in nature and may be consistent with a black-hole driven stellar binary merger induced by the Kozai mechanism.

We then observationally characterize several other infrared excess sources to see whether or not they share similar properties. We find another source, G3, has nearly identical observation properties to G1 and G2 but lies further away from Sgr A$*$. G3 does not lie on the same orbital plane to G1 or G2 at all, suggesting that these objects do not necessarily all come from the same region. G3 does not lie on a highly eccentric orbit at all ($e \sim 0.4$) and its periapse passage distance is significantly further away than G1 or G2 ($a_{min} \sim 5000$ AU). Several other sources also exhibit Br-γ emission, but also do not lie on the same orbital plane as G1 or G2.

G3 and other infrared excess sources supports the hypothesis that there is a population of objects that share similar observational qualities to G1 and G2 – high infrared luminosities, cold dust temperatures, and Br-γ emission line features. These new objects might therefore exist as a new population of sources in the Galactic center, and might not necessarily have the same physical manifestation.

The dissertation of Breann Nicole Sitarski is approved.

Edward Donald Young

Michael P. Fitzgerald

Mark R. Morris

Andrea M. Ghez, Committee Chair

University of California, Los Angeles

2016

To my wonderful family and friends who keep me happy and healthy

Table of Contents

List of Figures

List of Tables

Acknowledgments

I feel so lucky to have worked with so many wonderful people during my time in graduate school, and this thesis would never have happened without them. First and foremost, I want to thank my family, without whom I would never have finished this or graduate school. Thank you for always listening to me talk about what was going on, what I needed to do, being excited about what I was doing, listening to numerous practice talks and presentations, and, most of all, for showing me how life is an adventure. I thank all of you so much.

I want to thank all of the graduate students at UCLA–both those presently there and past students. To my incredible officemates, Tom Esposito and Michael Topping, who helped me out so many times when I was stuck on research and truly made it fun to come into work everyday. It was awesome to be able to have girl talk with you too, obviously. To Laura Haney, my carpool, *Astronomy Live!*, and apartment complex buddy: thank you for always looking out for me, hanging out with me, and having crazy writing sessions where we were so productive! To Shane Frewen, my fellow *Astronomy Live!* leader: I am so privileged that we were able to work on outreach together and expand *Astronomy Live!*. To Emily Martin: we basically are the same person, and I feel so honored that I got to work on so many things like the many workshops we lead together. I triangle you!!! To Fred Davies: your excitement about astronomy and everybody's research was so motivating, and I will always appreciate the help you gave me when I was stuck in my research. To Ryan Sanders: Thanks for always talking basketball and football with me, and for being an awesome director of the summer workshop. To Anna Boehle and Sarah Logsdon: Thank you both for always being there when I needed to talk, and for all the fun adventures we had! To Nate Ross, Shane Frewen, and Tom Esposito: I was so honored to have all three of you as close friends in the class above me, as you were always an inspiration.

There are definitely others within the field that have helped me put this thesis together and have kept up my motivation by constantly encouraging me. To Gunther Witzel: I really don't think I would have ever grasped the intricacies of the L' data set or finish the phase map interpolation without you. Thank you for being a wonderful mentor! To Tuan Do:

Thank you for advising me and helping me navigate the tricky waters of the Galactic Center when I was stuck. To Greg Mace and Kristin Kulas: Thank you both for starting such a truly wonderful group with *Astronomy Live!* and for your positive feedback and help! To Cyndie and James Larkin: Thank you so much for all the help and support you both have given me throughout the years, from when I was a wee undergrad to now. To the UCLA IR Lab: Thank you for all the wonderful talks we'd have about Star Wars and Disney, and, of course, IRLDLD!!

There are those outside the field as well that I must thank. To Sophia Hocini, who has been one of my closest friends since the fourth grade: thanks for always making me feel like I do really cool science and for talking about everything! To Nick and Rachel Barnett: Thank you both for hosting me on my many visits to Texas for writing retreats and thinking that I was some sort of cool scientist! To Alexx Perloff, my best friend: Thank you for being supportive, encouraging, and calling in to check on me so often! You are amazing and I can't wait to see what you do (and finally have free time to visit)! Finally, I would like to thank Ronnie Izzo for your patience, love, support, understanding, and for pushing me to do my best. Thank you for believing in me and believing I could finish this.

I'd like to thank my advisors, Andrea Ghez, Mark Morris, and Mike Fitzgerald for their support on all the various projects I have finished (or attempted)! It was wonderful being able to work with such inspirational people who helped me grow as a scientist.

Support for much of this work was provided by NSF grants AST-0909218 and AST-1412615, the Levine-Leichtman Family Foundation, the Preston Family Graduate Fellowship, the Keck Foundation, and the UCLA Graduate Division Dissertation Year Fellowship. Most data taken for this thesis was obtained at the W. M. Keck Observatory, which is operated as a scientific partnership among the California Institute of Technology, the University of California, and the National Aeronautics and Space Administration. I wish to recognize that the summit of Mauna Kea has always held a very significant cultural role for the indigenous Hawaiian community. I am most fortunate to have the opportunity to observe from this mountain. The Observatory was made possible by the generous financial support of the W. M. Keck Foundation.

Chapter 2 of this thesis is a version of a recently submitted paper, Sitarski et al. (2016). I would like to thank my collaborators on this project: Gunther Witzel, Andrea Ghez, Mark Morris, Tuan Do, Jessica Lu, Smadar Naoz, Anna Boehle, Greg Martinez, Sam Chappell, Rainer Schödel, Leo Meyer, Sylvana Yelda, Eric Becklin, and Keith Matthews.

Chapter 4 of this thesis is a version of Sitarski et al. (2014) and Sitarski et al. (2016). I would like to thank my many collaborators on this work: Gunther Witzel, Jessica Lu, Michael Fitzgerald, Tuan Do, Andrea Ghez, Greg Doppman, Jim Lyke, Randy Campbell, Marc Kassis, Luca Rizzi, Keith Matthews, Scott Lilley, Rachel Rampy, Max Service, Matthew Britton, Mark Morris, Eric Bekclin, Peter Wizinowich, and Sam Ragland.

Vita

2010	B.S. (Astrophysics), UCLA, Los Angeles, California.
2012	M.S. (Astronomy), UCLA, Los Angeles, California. NSF Graduate Research Fellowship Program Honorable Mention
2011, 2012, 2013	Teaching Assistant, Department of Physics and Astronomy, UCLA
2015	Preston Family Graduate Fellowship
2015-2016	Dissertation Year Fellowship, University of California, Los Angeles
2016	Block Award, Aspen Center for Physics

Publications

Sitarski, B. N., Witzel, G., Ghez, A. M., Morris, M. R., Do, T., Lu, J. R., Naoz, S., Boehle, A., Martinez, G., Chappell, S., Schödel, R., Meyer, L., Yelda, S., Becklin, E., E., Matthews, K. *The Post-Periapse Evolution of Galactic Center Source G1: The Second Case of a Resolved Tidal Interaction with a Supermassive Black Hole.* Submitted to ApJ.

Service, M., Lu, J. R., Campbell, R. D., Sitarski, B. N., Ghez, A. M., Anderson, J. *A New Distortion Solution for NIRC2 on the Keck II Telescope.* 2016, PASP, 128, 5004.

Stephan, A. P., Naoz, S., Ghez, A. M., Witzel, G., Sitarski, B. N., Do, T., Kocsis, B. *Merging Binaries in the Galactic Center: The eccentric Kozai-Lidov mechanism with stellar evolution.* 2016, MNRAS, 460, 3494.

Boehle, A., Ghez, A. M., Schödel, R., Meyer, L., Yelda, S., Albers, S., Martinez, G. D., Becklin, E. E., Do, T., Lu, J. R., Matthews, K., Morris, M. R., Sitarski, B. N., Witzel, G. *An Improved Distance and Mass Estimate for Sgr* A^* *from a Multi-Star Orbit Analysis.* Submitted to ApJ.

Witzel, G., Ghez, A. M., Morris, M. R., Sitarski, B. N., Boehle, A., Naoz, S., Campbell, R., Becklin, E. E., Canalizo, G., Chappell, S., Do, T., Lu, J. R., Matthews, K., Meyer, L., Stockton, A., Wizinowich, P., Yelda, S. *Detection of Galactic Center Source G2 at 3.8* μm *during Periapse Passage.* 2014, ApJ, 796, 8.

Sitarski, B. N., Witzel, G. Fitzgerald, M. P., Meyer, L., Ghez, A. M., Campbell, R. D., Lu, J. R., Matthews, K., et al. *Modeling Instrumental Field-Dependent Aberrations in the NIRC2 Instrument on the Keck II Telescope.* 2014, SPIE Proceedings, 9148, 6.

Meyer, L., Ghez, A. M., Witzel, G., Do, T., Phifer, K., Sitarski, B. N., Morris, M. R., Boehle, A., Yelda, S., Lu, J. R., Becklin, E. *The Keplerian Orbit of G2.* 2014, IAU Symposium Proceedings, 303, 264

Sitarski, B. N., Morris, M. R., Lu, J. R., Duchene, G., Stolte, A., Becklin, E. E., Ghez, A. M., Zinnecker, H. *Keck Adaptive Optics Observations of the Protostellar Disk around Radio Source I in the Orion Kleinmann-Low Nebula.* 2013, ApJ, 770, 134.

Fitzgerald, M. P., Witzel, G., Britton, M. C., Ghez, A. M., Meyer, L., Sitarski, B. N., Cheng, C., Becklin, E. E., Campbell, R. D., Do, T., Lu, J. R., et al. *Modeling Anisoplanatism in the Keck II Laser Guide Star AO System.* 2012, SPIE Proceedings, 8447, 24.

Burgasser, A., Sitarski, B. N., Gelino, C. R., Logsdon, S., Perrin, M. D. *The Hyperactive L Dwarf 2MASS J13153094-2649513: Continued Emission and a Brown Dwarf Companion.* 2011, ApJ, 739, 49

CHAPTER 1

Introduction

The center of the Galaxy provides a unique laboratory to study the environment around the nearest example of a supermassive black hole (Sgr A*) to Earth. At a distance of ~8 kpc, the Galactic Center (GC) is the only place where the orbital motion of individual stars have provided accurate measurements of the mass and distance to a galactic nucleus ($M = 4 \times 10^6$ M$_\odot$, $d = 8$ kpc; Eckart & Genzel 1996, 1997; Genzel et al. 1996; Ghez et al. 1998, 2000, 2003, 2005b, 2008; Schödel et al. 2002, 2003; Eisenhauer et al. 2003, 2005; Gillessen et al. 2009; Boehle et al. 2016). The heart of the Galaxy not only hosts a supermassive black hole, but it further serves as a home for an enigmatic environment and stellar population whose presence has been revealed by the advent and advancement of Adaptive Optics (AO) technology and high-resolution imaging and spectroscopy facilities. The chaotic environment surrounding Sgr A* consists of a central cluster of young stars (the so-called "S-star cluster"; see Figure 1.1), a significant amount old, cool giants, variable infrared emission from Sgr A*, and a series of cold, dust-enshrouded objects whose physical nature is still unclear.

A large fraction of the stars within the central parsec are old (>1 Gyr), cool (T ~3500-3700 K) giants of intermediate mass (Genzel et al., 2010). The stellar profile of the central 0.5 pc of the Milky Way nuclear cluster was predicted to have a Bahcall-Wolf cusp with a predicted power law of $\rho(r) \propto r^{-\gamma}$, with r being the distance from the supermassive black hole and γ ranging from 7/4 to 3/2 (Bahcall & Wolf, 1976, 1977; Do et al., 2013b). Recent work by Do et al. (2009a, 2013a,b) has shown that the density profile is actually much shallower (γ=$0.05^{+0.29}_{-0.60}$), implying that there are less old stars than originally thought and that the nuclear star cluster might be unrelaxed. This could stem from secular or disruptive events, including resonant relaxation (e.g., Madigan et al. 2011), infall of a black hole (e.g.,

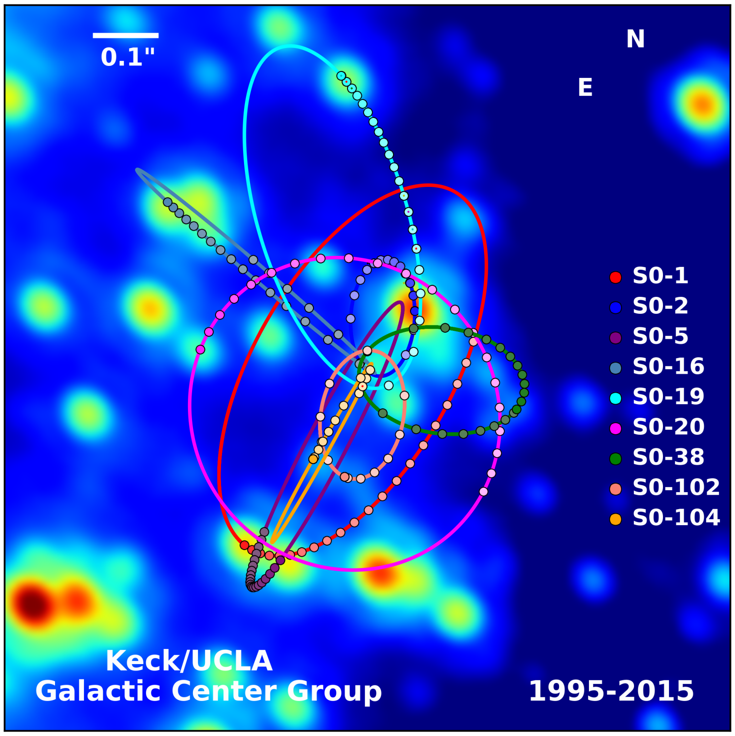

Figure 1.1 S-Stars in the central arcsecond of the Galactic Center with the orbits drawn from our ~20 years of astrometric monitoring. We have observed three of these stars orbit completely around the central supermassive black hole: S0-2, S0-102, and S0-38.

Merritt et al. 2010), and collisions between the stars (e.g., Dale et al. 2009). Buchholz et al. (2009) also find a dearth in the number of old stars detected within the central arcsecond.

While most of the stars in the Galactic Center are old, late-type stars, there are many young ($\leq$10 Myr), massive OB and Wolf-Rayet (WR) stars in the central parsec. Some of these massive, young stars orbit in a clockwise disk around Sgr A* (e.g., Allen et al. 1990; Najarro et al. 1997; Ghez et al. 2003; Paumard et al. 2006a; Do et al. 2009a; Bartko et al. 2009a; Lu et al. 2009, 2013; Yelda et al. 2014), and others are members of the central S-Star cluster and are on high-velocity orbits that have an isotropic distribution in eccentricities, angular momentum vectors, and apoapse directions (Ghez et al., 2005b). The origin of these young sources is unknown: the gas densities in the Galactic Center are currently far too low for a recent epoch of star formation ($\rho_{now} \sim 10^4$ cm^{-3}; Morris 1993), but the density may have been higher in the past, like during the most recent epoch of star formation (~6 Myr ago; Paumard et al. 2006a). The young stars could have instead formed further away from Sgr A* and migrated inwards as remains of a dissolved young stellar cluster (Gerhard, 2001; Kim & Morris, 2003; Hansen et al., 2003). Alternatively, the young stars could have formed *in situ* (Levin & Beloborodov, 2003), particularly since it is thought that ~50% of stars in nuclear star clusters form *in situ* (Antonini, 2014). If the young stars did form at the Galactic Center during the most recent episode of star formation, some of the young stars may still harbor their protoplanetary disks. This would be similar to the Arches and Quintuplet clusters, where there is evidence for circumstellar disks in chaotic environments (Stolte et al., 2010, 2014). Alternatively, the stars could be old stars that appear to be young due to interactions with the environment and have just migrated inwards (e.g., Morris 1993; Genzel et al. 2003). The identity of these stars, including their birthplace, has remained a mystery.

In addition to this "paradox of youth" and lack of old stars in the central arcsecond, the presence of a very faint, but highly variable, near-infrared and x-ray emission has been detected that is believed to be associated with the black hole's accretion flow (e.g., Witzel et al. 2012b and references therein). There is additionally a correlation between the near-infrared, submillimeter, and X-ray regime flares emanating from the area around Sgr A*, suggesting that the emission originates from the immediate surroundings of the supermassive black hole. Its variability in the near-infrared is particularly important, as it can rise from extremely faint levels (undetectable at 2.2 μm) to flux levels greater than that of S0-2, one of the brightest stars near Sgr A* ($K'_{dereddened} = 11.6$; e.g., Meyer et al. 2014). X-rays flares can be $\sim$100 times higher than the base-line flux levels. Both these wavelength regimes have therefore been used to probe accretion activity from the supermassive black hole.

The most recent Galactic Center discovery from high-resolution infrared observations that has attracted a considerable amount of attention is G2, a cold object ($\sim$550 K; Gillessen et al. 2012) that very recently passed through periapse ($T_{0,G2} = 2014.21 \pm 0.13$; Meyer et al. 2014). It is only detected in the thermal infrared (3.8 μm and 4.7 μm) as a compact source and has Br-γ emission elongated along its orbital trajectory. Much controversy surrounds the physical description of G2, as it is both a large (>2 AU) and cold object that remained compact through and post-periapse passage (Witzel et al., 2014; Valencia-S. et al., 2015). This is at odds with the predictions associated with the original hypothesis that G2 is a 3 Earth-mass gas cloud, as G2 did not dissociate after periapse, its flux remained constant with pre-periapse levels (Witzel et al., 2014), and there was no change in the flaring state of Sgr A* (Gillessen et al., 2012; Burkert et al., 2012; Schartmann et al., 2012; Pfuhl et al., 2015; Haggard et al., 2014). With limited observations, the physical description of G2 remains a mystery. In this thesis, I will characterize other sources that have similar observational properties to G2.

Near-infrared observations of the Galactic Center with laser guide star AO (LGSAO) systems are crucial for exploring and understanding the environment surrounding Sgr A*. With visual extinction levels as high as $A_V \sim 40$ (e.g., Gao et al. 2013), it is not feasible to cut through the dust extinction from the Galactic disk to obtain high-resolution images of the Galactic Center at visible wavelengths. However, extinction levels are significantly less in the near-infrared regime as the observing wavelength becomes large enough to cut through the dust (e.g., $A_{K(2.2\mu m);SgrA^*} = 2.46$; Schödel et al. 2010). In this thesis, I use high-angular resolution imaging and integral field spectroscopy data taken with the W. M. Keck I and II telescopes and LGSAO and natural guide star AO (NGSAO) systems over a baseline ranging from 2003 to 2015 to understand the characteristics and physical properties and dynamic evolution of the cold, infrared-excess sources at the Galactic Center.

1.1 Infrared Excess Sources in the Galactic Center

The discovery of G2 by Gillessen et al. (2012) introduced the first spatially-resolved interaction of a point source with the supermassive black hole at the Galactic Center. Perhaps the most peculiar aspect of G2 is its still-debated physical nature. As a 3 Earth-mass gas cloud, G2 was projected to tidally disrupt with Sgr A*, dissipate over time, have shock interactions, and possibly accrete onto Sgr A* (e.g., Gillessen et al. 2012; Burkert et al. 2012; Schartmann et al. 2012; Pfuhl et al. 2015).

Observations of G2 after periapse passage have challenged the gas cloud hypothesis. First, it survived as a compact source in the dust continuum (L' imaging measurements at 3.8μm; Witzel et al. 2014) and possibly as a compact source in the gas (Br-γ spectroscopic measurements; Valencia-S. et al. 2015, but see Pfuhl et al. 2015). This leads to the idea that there is a central stellar source embedded in G2, but there are several hypotheses of the nature of central source, including both stellar and gas-cloud based models.

One of the key issues arising from the 3-Earth mass pure gas cloud model is that it implies that the gas cloud was formed in 1995, which is alarmingly close to when observations of the Galactic Center began (e.g., Ghez et al. 1998) and may therefore present some underlying bias. In a chaotic environment like the Galactic Center (and in particular where G2 is located; see Figure 1.3), there is a large amount of UV radiation and gravitational forces that can destroy pure gas clouds. Burkert et al. (2012) proposed a different gas-based hypothesis where G2 instead exists as a spherically symmetric ring; this gives an earlier formation date, but the likelihood of a spherically symmetric ring existing in the Galactic Center is very low.

Shortly after G2 was discovered by Gillessen et al. (2012), numerous conjectures were proposed that instead have G2 have some sort of massive, stellar component internal to the gas and dust that was observed. These have a wide range of internal stellar objects. The first proposed was by Murray-Clay & Loeb (2012), where the observed dusty/gassy G2 that

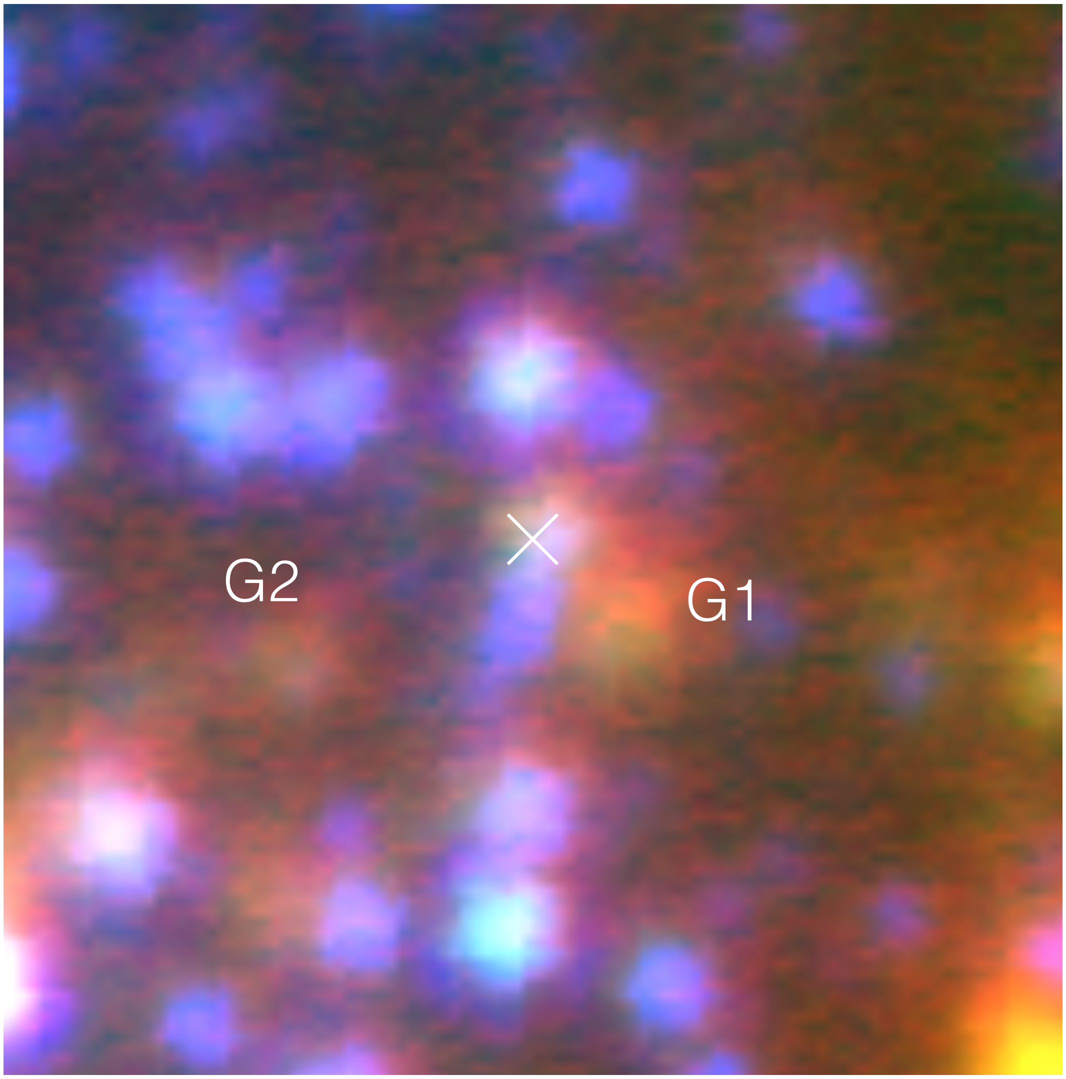

Figure 1.2 A three-color image produced from high-resolution data from W. M. Keck Observatory where blue signifies K' (2.2 μm), green shows our L' (3.8 μm) data, and red highlights our Ms (4.7 μm) data. G2 is evidently very red compared to nearby sources.

we see is a disrupted proptolanetary disk. As the young stellar population in the Galactic Center is ∼6 Myr (see previous section), ∼10% of new stars still have dusty disks at large radii (Pfalzner et al., 2014). In this picture, ionizing photons from nearby O stars heat the disk surface, driving an ionized wind, and radiative recombination balances photoionization in outer part of the disk. Most (but not all) the emission that is observed at Br-γ and L' arises from near the disk surface. One issue with this hypothesis, though, is that the Br-γ emission arising from G2 has not increased as G2 approaches periapse passage (Pfuhl et al., 2015; Valencia-S. et al., 2015). Miralda-Escudé (2012) proposed that G2 is a disrupted disk around an older star that formed as a stellar-mass black hole passed close to the star and tidally disrupts its outer envelope. This disk has survived many passages close to Sgr A*. However, this model would imply an increased infrared luminosity around periapse passage, but this has yet to be seen (e.g., Witzel et al. 2014). Scoville & Burkert (2013) surmised that G2 is the observed envelope of a T Tauri star that loses mass as it passes close to Sgr A*; bow shocks form as the stellar winds impact the X-ray gas that is close to the black hole. While this scenario has G2 surviving periapse passage, it does predict brighter emission at and after periapse passage, which is not observed at either L' or Br-γ (Witzel et al., 2014; Valencia-S. et al., 2015; Pfuhl et al., 2015). Additionally, based on L' (3.8 μm), Ks (2.2 μm), and H-band (1.65 μm) measurements, Eckart et al. (2013) thought that G2 could be a dust cloud or a dust-embedded star that may have part of its extension blown away from the wind associated with Sgr A*. While a dust-embedded star cannot be excluded based on observations of G2, there has been no measured interaction of G2 with Sgr A* and measured in the X-ray regime (e.g., Haggard et al. 2014, but see Ponti et al. 2015). Valencia-S. et al. (2015) hypothesize that G2 could be an embedded pre-main sequence star, but this suggests that part of the envelope may have accreted onto Sgr A* and the flaring rate would increase, but this has not been observed, as stated before.

Phifer et al. (2013), Witzel et al. (2014), Prodan et al. (2015), and Stephan et al. (2016) infer that G2 could instead be a binary merger product induced by the Kozai-Lidov (KL) mechanism Kozai (1962); Lidov (1962), which is a natural explanation for many of the observed peculiar phenomena seen in the Galactic Center, including the S-star cluster and the lack of observed binaries at the Galactic Center (see Pfuhl et al. 2015 and comprehensive exam paper by Abhimat Gautam). A recent theoretical study by Stephan et al. (2016) posit that if the last episode of star formation was indeed 6 Myr ago, then direct mergers (where the binary components cross each other's Roche lobes) might be G2-like objects, and they should have dust shells and gas envelopes surrounding them. In fact, they find that $\sim$13% of the binary population should have merged after 6 Myr, and their products create G2-like objects. While G1 and G2 have been found to have high orbital eccentricities (e.g., Gillessen et al. 2012, 2013b; Phifer et al. 2013; Meyer et al. 2014; Pfuhl et al. 2015; Sitarski et al. 2016), Stephan et al. (2016) find that direct binary mergers can exist across all orbital eccentricities and do not necessarily have to have high ($e > 0.8$) eccentricities.

Pfuhl et al. (2015) report an orbital analysis of of G1, a source with similar observational properties to G2, that recently went through periapse passage ($T_0 = 2001.3$; Sitarski et al. 2014, 2016). They physically tie G1 and G2 together as two objects that are part of the same gas streamer on one orbital trajectory, as they conclude that the Keplerian orbital elements of G1 and G2 are the same. While G1 went through periapse $\sim$13 years prior to G2. They therefore predict that G2's orbit will follow G1's observed orbit within the few years after the completion of this dissertation. Other studies draw upon this physical model, including Madigan et al. (2016) and McCourt & Madigan (2015), both of which use G1 and G2 as probes to constrain the properties of the accretion flow surrounding Sgr A* to better constrain the small flaring rate.

In Chapter 2, I pursue the putative connection of G2 with G1, one of the closest objects, in projection, to our Galaxy's supermassive black hole. In several ways, G1 resembles G2: it has an unusually red color and exhibits Br-γ line emission (Ghez et al., 2005a; Clénet et al., 2004). Additionally, G1 is spatially resolved, and while it was initially interpreted as a hot dust feature that was locally heated by nearby stars surrounding the position of Sgr A*, new observations suggest that it moves on a Keplerian orbit with orbital characteristics similar to G2 and other stars in the vicinity (Pfuhl et al., 2015; Sitarski et al., 2014). G1 also passed through periapse $\sim$13 years ago (Pfuhl et al., 2015; Sitarski et al., 2014), and therefore high-resolution observations only exist *post*-periapse passage while we have observations of

G2 prior to, through, and post-periapse passage. If G1 and G2 are indeed similar, then G1 can be used to further explore the physical nature of G1 and G2. I explore the evolution of G1's spatial extent, its brightness, and its orbital motion over the last decade. We further investigate the connection between G1 and G2, and whether these objects indeed can be merged binary systems.

Recent models of G2 as a gas cloud used to probe the inflow near Sgr A* find that if G2 is indeed the originally-hypothesized 3 Earth-mass gas cloud, its periapse time could actually be in August of 2014 instead of March of 2014 due to a drag force from a background accretion flow (Madigan et al., 2016). Thus therefore puts the post-periapse observational results from Witzel et al. (2014) and Valencia-S. et al. (2015) into question. However, 2015 observations, which are presented in Chapter 3, will directly nswer whether G2 survived periapse passage, even if it is affected by the accretion flow.

While G1 and G2 both get within ~300 AU of Sgr A*, there is a group of other red sources that exist in the heart of the Galaxy ($r \leq 1.75''$). Eckart et al. (2006) originally pointed out 8 (including G1) objects that within the central $1''.3$ that contribute to dust emission and are observed at wavelengths longer than 2.2 μm. Eckart et al. (2013) followed up on several of these sources and measure their proper motions, and posit that they are young, dusty stars and that the Galactic Center is currently (and has been) forming stars for quite awhile. Morphologically, several of these sources are elongated, and a few have been identified with K'-detected stars.

The analysis presented in Eckart et al. (2013) is primarily based on proper motion results from L' data taken over a period of ~10 years. An additional time baseline and spectroscopic measurements would allow for full Keplerian orbital determination. If they are indeed young, dusty stars, it would be interesting to see if they follow orbits similar to the clockwise disk or the S-star cluster.

As these sources are observationally similar to G1 and G2 with their infrared excess sources, they may also physically be G2-like objects. In chapter 3, I discuss using observations of these sources to measure the frequency of G2-like objects. I also determine the kinematic structure of these sources to see if they are consistent with an isotropic distribution like the S-star cluster, if they are instead consistent with orbits along the clockwise disk, or if they lie on the same orbital plane as G1 and G2.

1.2 Adaptive Optics Observations of the Galactic Center: Astrometry with Spatially Variable PSFs

High-resolution observations of the Galactic Center have only been available with the advent of adaptive optics technology coupled with large, 10-meter class telescopes such as those available at the W. M. Keck Observatory. All the work reported in this thesis makes use of this technology; for most of the observations and data sets used, we rely on Laser Guide Star Adaptive Optics (LGSAO). As stated before, the Galactic Center has ∼30 magnitudes of visual extinction. The natural guide star adaptive optics (NGSAO) system at Keck requires a visible-light source of at least $R = 12$ magnitudes (van Dam et al., 2004) to obtain diffraction-limited observations within $20\overset{\prime\prime}{.}0$ of stars, but having bright stars this close to the Galactic Center is extremely hard with the nearly 30 magnitudes of visual extinction present. However, in 2005, the LGSAO system came online at Keck, and any object within $60\overset{\prime\prime}{.}0$ of a bright ($R = 19$ mag) tip-tilt star could be obtained (van Dam et al., 2006; Wizinowich et al., 2006). For our Galactic Center observations, there is a wavefront reference star ($R = 14.0$ mag) about $19\overset{\prime\prime}{.}3$ away from Sgr A^*.

While this technology has led to numerous significant scientific discoveries, there are still limitations to it that inhibit further scientific progress. One such limitation is anisoplanatism, which arises when the guide star in an adaptive optics (AO) system is sufficiently far from the science target and a different part of the atmosphere is therefore probed than what distorts the science observations. Anisoplanatism in single-conjugate AO systems leads to spatially-dependent aberrations and spatial variation of the point spread function (PSF); while this can be somewhat overcome with multi-conjugate captive optics systems, the costs of those systems are far beyond what can currently be funded at Keck Observatory.

Spatial variation of the PSF is the primary source error limiting our astrometric mea-

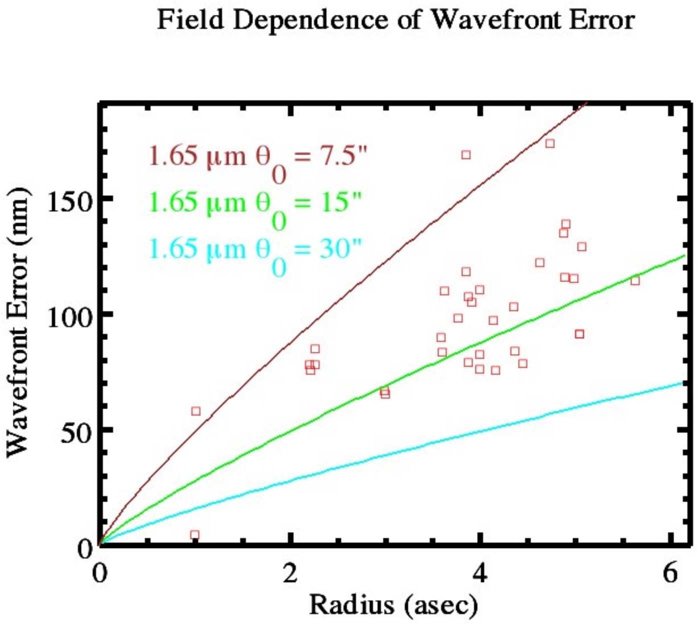

Figure 1.3 Plot showing the instrumental wavefront error (red squares) in comparison to the atmospheric wavefront error. At large θ_0, these two terms become comparable or dominated by the instrumental contribution to the wavefront error.

surements in the Galactic Center. Due to the nature of a spatially varying PSF, no single reference PSF can be used to obtain the photometry and astrometry of individual point sources, particularly in a crowded field like the Galactic Center. However, this field dependence can be corrected in the post-processing phase: the measurements of the atmospheric turbulence profile ($C_n^2(z)$) can be measured and used to model the field dependence of the atmospheric response to the anisoplanatism, which has already been demonstrated at Palomar Observatory (Britton, 2006). More specifically, measurements from the MASS/DIMM system currently at the summit of Mauna Kea can give the atmospheric turbulence profile as a function of height in the atmosphere.

In addition to atmospheric anisoplanatism, the instrumental field aberrations arising from non-common path errors from the telescope, adaptive optics system, and instrument (short: instrumental aberrations) also need to be taken into account as they can be comparable to the atmospheric contribution to the wavefront error (see Figure 1.3). Effects from the instrumental and atmospheric contributions to the measured spatial variability of the PSF can be combined as follows (Fitzgerald et al., 2012):

$$\mathrm{OTF}(\mathbf{f};\vec{\alpha},t) = \mathrm{OTF}_{\mathrm{on-axis}}(\mathbf{f};t) \cdot \mathrm{OTF}_{\mathrm{inst-off}}(\mathbf{f};\vec{\alpha},t) \cdot \mathrm{OTF}_{\mathrm{aniso}}(\mathbf{f};\vec{\alpha},t). \tag{1.1}$$

where OTF denotes the optical transfer function, or the Fourier transform of the point spread function; $\vec{\alpha}$ denotes the field angle vector; $\mathbf{f}$ denotes the spatial frequency; and t denotes the time. The total OTF is therefore a combination of the contributions of three independent terms: an on-axis, or reference, OTF; an instrumental OTF that describes the field dependence of the instrumental aberrations; and the atmospheric OTF describing the field dependence of angular anisoplanatism. The atmospheric OTF calculation has been largely described in Britton (2006) for the NGS case and Witzel et al. (2012a) for the LGS case. The on-axis OTF can be estimated by other means, such as on-sky phase diversity (e.g., Jolissaint et al. 2014; Ragland et al. 2014) or through crowded-field estimation.

The instrumental term is, in general, a function of field angle. As shown in Fitzgerald et al. (2012), this is dependent on the pupil function and the phase aberration between some reference point ($\vec{\alpha}$=0) and the field position. The latter term can be empirically calculated with fiber phase diversity taken across the field of view of the science detector of the instrument being used. For the two cases presented here, one using the near-infrared facility camera NIRC2 (PI: K. Matthews) and the other using the integral field spectrograph OSIRIS (Larkin et al., 2006), we can use a steerable fiber source in the Nasmyth focus of the telescope.

This chapter is described as follows: section 2 describes our fiber phase diversity data collection; section 3 describes the wavelength dependence of the grid of data taken; section 4 describes the time variability studies performed on the data; section 5 describes the alignment of NIRC2 and affects on the grid; section 6 details the application of the methodology to the OSIRIS imager and spectrograph; section 7 presents on-sky tests and validation; and section 8 discusses interpolation modeling of the phase diversity grids.

CHAPTER 2

The Post-Periapse Passage of Galactic Center Source G1

2.1 Introduction

As the capabilities of high-resolution imaging facilities have advanced, the center of our Galaxy has become a unique laboratory for studying the nearest supermassive black hole (SMBH; Ghez et al. 1998, 2008; Gillessen et al. 2009) and has revealed many unexpected results. This includes the presence of young stars where none were expected (e.g., Levin & Beloborodov 2003; Genzel et al. 2003; Paumard et al. 2006b; Bartko et al. 2009b; Lu et al. 2009; Yelda et al. 2014), a lack of old stars where many were predicted (e.g., Buchholz et al. 2009; Do et al. 2009a), and very faint, but highly variable, infrared emission believed to be associated with the black hole's accretion flow.

The most recent Galactic Center discovery from high-resolution infrared observations that has attracted considerable attention is the very red, infrared source G2, which recently went through closest approach where its tidal interaction should have been maximal ($T_{0,G2}$ = 2014.21 ± 0.13; Meyer et al. 2014). It was originally hypothesized to be a 3 Earth-mass gas cloud, and as it went through closest approach to the supermassive black hole, Sgr A*, it was projected to tidally disrupt, shock and to possibly contribute to an enhanced accretion episode onto the black hole (Gillessen et al., 2012; Burkert et al., 2012; Schartmann et al., 2012; Pfuhl et al., 2015). Observations of G2 after periapse passage have challenged the gas cloud hypothesis. First, it survived as a compact source in the continuum imaging measurements at 3.8 μm (Witzel et al., 2014) and possibly as a compact source in the gas (Br-γ spectroscopic measurements; Valencia-S. et al. 2015). This has favored the alternative hypothesis that there is a central stellar source embedded in G2. There are several variants of the stellar hypothesis, including: a disrupted protoplanetary disk (Murray-Clay & Loeb, 2012); a disrupted disk around an old star (Miralda-Escudé, 2012); a mass-loss envelope from a young T Tauri star (Scoville & Burkert, 2013); a Wolf-Rayet star (Eckart et al., 2013); spherically symmetric winds from an embedded object (Ballone et al., 2013); a binary merger product (Phifer et al., 2013; Witzel et al., 2014; Prodan et al., 2015); and an embedded pre-main sequence star (Valencia-S. et al., 2015).

More recently, another object – G1 – has been recognized to bear a close relationship to G2. G1 was originally found to be another very red, extended infrared source that was interpreted as a spatially-resolved, stationary hot dust feature that is locally heated by nearby stars surrounding Sgr A* (Clénet et al., 2004, 2005; Ghez et al., 2005a). In addition, Pfuhl et al. (2015) noted that G1 has observational properties similar to those of G2, including Br-γ emission as well as a very red color. Also, G1 passed through periapse $\sim$13 years ago (Pfuhl et al., 2015; Sitarski et al., 2014), and therefore high-resolution observations only exist *post*-periapse passage while we have observations of G2 prior to, through, and post-periapse passage. The observations in Pfuhl et al. (2015) also suggest that G1 moves on a Keplerian orbit with orbital characteristics similar to G2 (Sitarski et al., 2014). These similar orbits and observational characteristics led Pfuhl et al. (2015) to hypothesize that G2 and G1 are part of a gas streamer on the same trajectory.

In this paper, we explore the evolution of G1's observed properties and orbital motion over the last decade, the longest time baseline reported thus far for this object. We investigate the evolution of G1 with time and position from Sgr A* to characterize its tidal interactions. With our longer time baseline, we test the theory that G1 and G2 are part of the same gas streamer.

This paper is organized as follows: Section 2 describes our data sets and data reduction techniques; section 3 details our astrometric and photometric calibration, and our orbital fitting procedure; section 4 presents our results; and section 5 discusses our findings in the context of G2 and evidence that these are self-gravitating objects. One scenario that we consider is the binary merger hypothesis. Section 6 summarizes our conclusions.

2.2 Data Sets

Near-infrared, high-angular-resolution images and spectra of the Galactic Center region containing G1 have been obtained as part of the long-term program at the W. M. Keck Observatory (WMKO), carried out by our group, to study the Galactic Center black hole and its environs. In this paper, the primary data sets are WMKO images that have been acquired through the L' ($\lambda_0 = 3.8\ \mu$m) broadband filter that were obtained over a thirteen-year period with NIRC2, the facility near-infrared camera (PI: K. Matthews) fed by the Keck II laser guide star adaptive optics system (LGSAO; Wizinowich et al. 2006; van Dam et al. 2006). Ten of the twelve epochs have been previously reported by us and are part of our group's archive of fully calibrated data sets (Ghez et al., 2004, 2005a; Hornstein et al., 2007; Phifer et al., 2013; Witzel et al., 2014). Two additional epochs of observation, 2013 August and 2016 May, are reported here for the first time. The pixel scale for these data sets is 9.950 mas/pixel (Yelda et al., 2010), which corresponds to an oversampling factor of ∼9 for typical point spread function. Table 1 summarizes all the L' imaging data sets for this study.

The new L' data sets were observed and calibrated using the same techniques described in the papers reporting our other L' data sets (Stolte et al., 2010; Phifer et al., 2013; Witzel et al., 2014). This followed standard techniques with one exception, which was the treatment of the sky exposures, which were taken with the same range of the field rotator mirror angles. For each L' science exposure in epochs after our 2004 observation, a series of sky exposures was subtracted such that the sky and science exposures had angles on the field rotator mirror that matched to within ∼2 degrees in order to accurately subtract the thermal emission from dust on the mirror optics (e.g., Stolte et al. 2010). Once the data were fully calibrated, selected individual frames were combined into an average map (main map). The individual frames were selected based on the image quality as measured by the full-width at half-maximum of the PSF ($\mathrm{FWHM} \leq 1.25 \times \mathrm{FWHM}_{\mathrm{min}}$, where $\mathrm{FWHM}_{\mathrm{min}}$ is the minimum measured FWHM of all the data) and were weighted by the Strehl ratio of each image. We additionally created three independent subset images (sub-maps) that are of equal quality and weighted by the Strehl ratio to determine astrometric and photometric uncertainties for the images.

For this study, we also draw upon two other types of imaging data sets. The first are two *Ms* ($\lambda_0 = 4.67\mu$m) observations obtained on 2005 July 16 (previously published by Hornstein et al. 2007) and another obtained on 2016 May 21. These were added to enhance our photometric characterization of G1. Second, we used all of our group's K' data sets, which cover the central 10" × 10" of our Galaxy, and that have been obtained to track the orbital motions of stars at the Galactic Center (Ghez et al., 1998, 2000, 2003, 2005b, 2008; Lu et al., 2009; Yelda et al., 2010; Meyer et al., 2012; Yelda et al., 2014; **?**). In addition to the previously published K' data sets, two new data sets, obtained on 2013 July 20 and 2016 May 21, are included in this work. The first data set was taken in an identical way to all previous K' astrometric maps (e.g., Yelda et al. 2014), consists of 193 frames of data, and its final combined image has a point spread function having a FWHM of 58.5 mas and strehl ratio of 0.36. The second was taken similarly to our L' observations, in which we stare at the central field. This map consists of 21 frames of data, and its final combined image has a PSF with a FWHM of 68 mas and a strehl ratio of 0.26. The K' data are used for both the photometric and astrometric characterization of G1.

Additionally, we utilize a spectroscopic data set obtained at W. M. Keck Observatory with OSIRIS (Larkin et al., 2006) This data set, which was originally published in Ghez et al. (2008), consists of 28 frames taken 2006 June 18 and 30 and 2006 July 01 through the narrow-band Kn3 filter ($\lambda_0 = 2.166$ μm) with the 35 mas pixel scale. These observations have a spatial resolution at Br-γ of 67 mas and a spectral resolution of ∼3600. These OSIRIS data constitute some of our deepest Kn3 observations prior to 2012[1], with a total integration time of ∼7 hours, and while at that time G1 was near Sgr A*, it was sufficiently separated ($r = 0.114 \pm 0.009$ arcseconds) for the position of Sgr A* and G1 to be disentangled.

---

[1] OSIRIS was moved from Keck 2 to Keck 1 in January 2012 and the grating was upgraded in January 2013; there have been small reduction artifacts that affect the detection of faint emission-line objects in crowded fields.

Table 2.1. Summary of Keck/NIRC2 L' ($\lambda_0 = 3.8\mu$m) Data

UT Date	Decimal Date	$t_{int}\times$ coadds	Frames Taken	Frames Used	Array Size	Dithered FOV	PSF FWHM (mas)	Strehl	L'_{lim} [a] (mag)	δ_x (mas)	Original Publication[b]
2002 May 31	2002.413	0.50 × 40	53	25	10” × 10 ”	11.″6 × 10.″5	100	0.26	12.0	2.2	0
2003 Jun 10	2003.440	0.50 × 40	12	6	10” × 10”	12.″8 × 10.″2	85	0.41	13.3	1.4	0
2004 Jul 26	2004.567	0.25 × 120	11	11	10” × 10”	10.″7 × 9.″8	80	0.42	14.4	0.4	1
2005 Jul 30 & 31	2005.580	0.50 × 60	62	56	10” × 10”	10.″3 × 9.″5	81	0.36	14.4	0.3	1
2006 May 21	2006.385	0.50 × 60	19	19	10” × 10”	11.″4 × 11.″3	82	0.38	14.4	0.4	2
2009 Jul 22	2009.556	0.50 × 60	4	4	10” × 10”	13.″1 × 12.″3	85	0.38	13.2	0.1	3
2012 Jul 20-23	2012.551	0.50 × 30	1316	1231	2.″64 × 2.″64[c]	2.″6 × 2.″8	92	0.51	15.3	0.2	3
2013 Aug 13	2013.616	0.50 × 60	249	245	2.″64 × 2.″64[c]	2.″7 × 2.″6	90	0.54	15.2	0.1	4
2014 Mar 20	2014.216	0.50 × 60	21	21	10” × 10”	10.″3 × 9.″3	91	0.51	14.4	0.4	5
2014 May 11	2014.359	0.50 × 60	9	9	10” × 10”	10.″1 × 9.″3	90	0.53	13.2	0.4	5
2014 Jul 2	2014.503	0.50 × 60	20	20	10” × 10”	10.″2 × 9.″3	91	0.34	14.1	0.4	5
2014 Aug 4	2014.590	0.50 × 60	28	28	10” × 10”	10.″2 × 9.″4	92	0.50	13.7	0.4	5
2016 May 21	2016.376	0.50 × 60	25	25	10” × 10”	10.″6 × 9.″3	85	0.38	13.8	0.4	4

[a] This is defined as the 95% quantile of the distribution of magnitudes of detected stars with *StarFinder*.

[b] References: (0) Ghez et al. 2004; (1) Ghez et al. 2005a; (2) Hornstein et al. 2007; (3) Phifer et al. 2013; (4) This work; (5) Witzel et al. 2014.

[c] For our smaller field of view data (L' in 20012 July and 2013 August and *Ms*), a PSF support size of 1” × 1” is used instead of our standard 2” × 2” support size in order to avoid edge effects. Comparisons on the larger field of view showed that his had no significant effect on the astrometry and photometry of G1.

2.3 Analysis

2.3.1 Imaging Analysis

Our imaging analysis is divided into two parts: (i) astrometric analysis using the PSF fitting tool *StarFinder* and (ii) photometric and size calculations using a PSF convolved with a 2D elliptical Gaussian. Both measurements are described in detail below.

2.3.1.1 Astrometry

G1 is visually identified in every L' and Ms image (see Figure 1). Its astrometric properties in every image were obtained using the PSF fitting program *StarFinder* (Diolaiti et al., 2000) in a manner similar to what has been outlined in previous works (Yelda et al. 2014 and references therein). We initially ran *StarFinder* using a correlation threshold of 0.8 and 0.6 in the main image and sub-images, respectively, to identify candidate sources in our images. This resulted in G1 detections in 2004, 2005, 2006, 2012, and 2013 in the L' data. In 2003, 2009 and all 2014 L' epochs and in both the Ms data sets, a different approach was necessary to capture G1 due to poorer data quality, although G1 can be visually identified (Figure 1). We therefore altered the search criterion to seek a point source within a three-pixel box centered at the point of the highest flux count, at the approximate position of G1 using a modified version of *StarFinder* that searches for additional sources at a lower correlation (**?**). We do not use the 2016 L' data for astrometry as we use the orbital model from 2003 - 2014 to predict the position of G1 in the 2016 data (see our photometric analysis described in Section 3.1.2). With this modified procedure, G1 was detected in all epochs.

While G1 is extended in the early epochs (Section 4.2), we still use the *StarFinder* astrometry that reliably determines G1's centroid, as the residual maps in each epoch look symmetric. Two-dimensional Gaussian fits convolved with a point spread function to G1 yielded peaks consistent with the positions extracted from *StarFinder*.

The point sources identified in each epoch are matched across all epochs and transformed to a common coordinate system in which Sgr A* is at rest (see Phifer et al. 2013; Yelda et al.

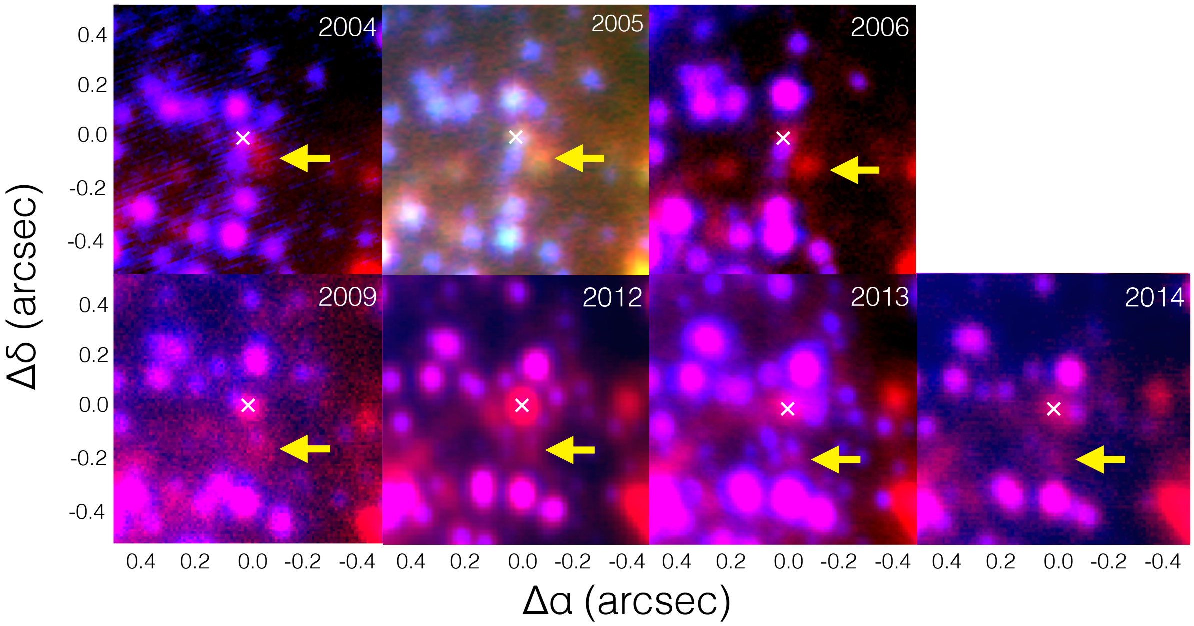

Figure 2.1 Two-color images made by combining NIRC2 images at K' (2.2 μm, in blue) and L' (3.8 μm, in red). The images have been aligned using the coordinates of S0-2 from our respective *StarFinder* rufns for each filter during each epoch; the 2014 data are from our March 2014 observation. The position of Sgr A* is denoted by the white "×", and the position of G1 is denoted by a yellow arrow. The 2005 panel shows a three-color image that includes our 2005 *Ms* data as well (2.2 μm in blue; 3.8 μm in green; 4.7 μm in red). G1 and G2 are distinctly red sources. Other red sources exist within the inner 0.5 arcseconds of Sgr A* as well and will be explored by Sitarski et al. (in preparation). It is apparent that Sgr A* varies considerably. For contour plots of G1, see Figure 6.

2010, 2014). Specifically, each L' list of stellar positions (short: star list) is aligned to the K' star list that is nearest in time with translation, rotation, and affine first-order transformation that is independent in x and y. The transformed G1 position is added to the K' star list and the K' star lists from 1995 to 2014 are aligned as described in our earlier works (e.g., Ghez et al. 2008; Yelda et al. 2014) using measurements of infrared astrometric secondary standards taken through 2012 (Yelda et al., 2010, 2014; Boehle et al., 2016). Table 2 lists the astrometry for G1 in each epoch prior to 2016.

2.3.1.2 Photometry and Size Measurement

Magnitudes of all point sources at K' were calculated using PSF fitting with *StarFinder* procedure (see previous section). We chose IRS 16C, IRS 16NW, and IRS 16CC as our photometric calibrators, which is part of our standard K' calibration procedure (e.g., Yelda et al. 2014).

As G1 seems extended in 2004, 2005, and 2006 at L' and Ms, we tested several photometric procedures to obtain reliable photometry. To confirm whether the individual photometric procedure during the epochs when G1 was visibly extended yielded reliable results, we planted a 2D elliptical Gaussian model for the 2004 size in our data in three distinct regions: a high-background region, a low-background region, and near the position of G1. We planted the source with different brightnesses($\mathrm{mag}_{L'}$ = 10-16) to determine whether we could recover their magnitudes and physical extent.

We tested three different photometric procedures: (1) *StarFinder* with a PSF support array of 2.0 arcseconds (200 pixels), following our standard K' procedure; (2) *StarFinder* with a PSF support array of 0.9 arcseconds (90 pixels) to make the PSF more robust against background artifacts at larger distances from the core; (3) intrinsic extended elliptical Gaussian source convolved with an empirical PSF model. The planting simulations returned significantly decreased fluxes with respect to their original planted magnitude in the case of *StarFinder* PSF fitting with both PSF sizes [(1) and (2)]. However, (3) reliably recovered the fluxes and observed extent of the planted sources to within 20% at the faintest magnitude tested ($\text{mag}_{L'} = 16$).

We applied method (3) to every single L' and Ms epoch (prior to 2016) using the IDL procedure *mpfit2dfun*. To prepare the images for model fitting, we first subtracted all L'-detected *StarFinder* sources. We then used the aligned L' and K' *StarFinder* star lists to find the position of K'-only detected sources and used the forced *StarFinder* algorithm from **?** to find the fluxes of these sources at L'. We subtracted these sources as well as the *StarFinder* generated backgrounds from the original image. In our 2D elliptical Gaussian model, we allowed the position angle to vary and allowed for the FWHM to range between 0.3 and 10.0 pixels. If the FWHM of G1 fell below 0.3 pixels (∼3 mas) in an epoch, then a PSF without a Gaussian component was used instead. Our photometry is reported in Table 2. A comparison of the astrometry between the three methods yielded identical positions of G1 within 1σ errors.

To photometrically calibrate our L' and Ms data, we used S0-2, S0-12, S1-20, and S1-1 and their L' magnitudes from Schödel et al. (2010). These sources were chosen because they are all in the field of view for every epoch, including our subarrayed epochs (see Table 1). Similarly to Schödel et al. (2011), the Ms data were calibrated using the same magnitudes as L', which is acceptable since the relative colors of the calibrators are close to 0. The magnitudes of these calibrators were taken from Schödel et al. (2010). The overall zero-point error from the Schödel et al. (2010) magnitudes is 0.15 magnitudes at L'. Neither the errors arising from the Schödel et al. (2010) calibrator magnitudes or the calibrator zero points are taken into account in Table 2 or Figure 3 because they affect all photometric points in the same way.

No K' counterpart was detected for G1 and star-planting simulations were performed to determine an upper magnitude limit. We used the L' position of G1 in the 2013 August image, where G1 is an isolated point source (see Figure 1) and transformed that into the 2013 July K' coordinate system. The star-planting simulations were carried out using our modified version of *StarFinder* (Phifer et al., 2013; Boehle et al., 2016). There is a K' source near G1 in 2013, S0-37, but it contributes at most 0.3 mJy to the overall L' flux of G1 (assuming the dereddening law outlined in Schödel et al. (2010) and that S0-37 has the same

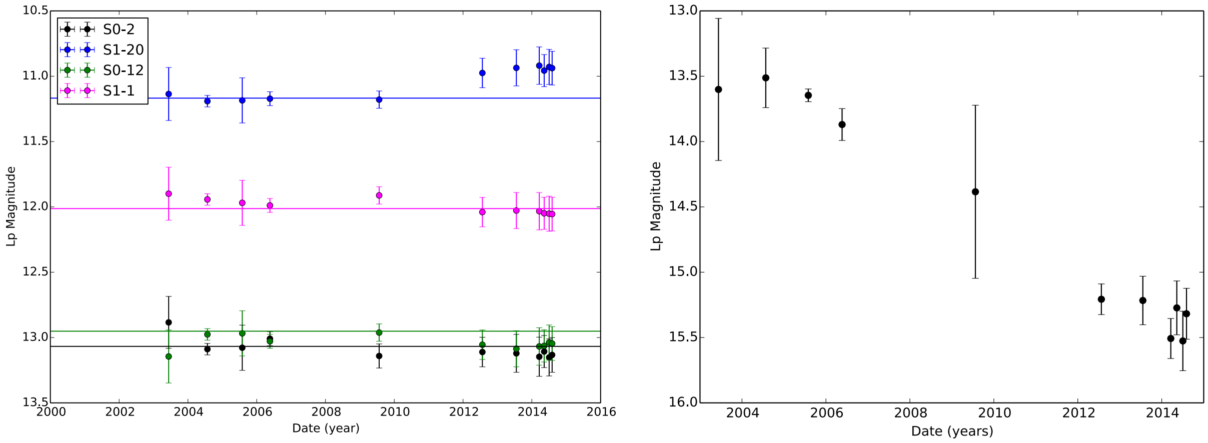

Figure 2.2 *Left*: L' photometry on each of our four calibration sources. The solid line denotes the reported magnitude from Schödel et al. (2011). *Right*: L' photometry of G1 a a function of time. The magnitude of the source has decreased significantly, and varies directly with the size of the source presented in Figure 4.

colors as S0-2). All photometry in each bandpass is reported in Table 2.

The recovered sizes of G1 from our model show that G1 is extended between 2004 and 2006, but is consistent with a point source from 2009 through 2014 (see Table 2). The magnitudes and sizes of G1 as a function of time are shown in Figures 2 and 3, respectively, while Figure 4 shows the elongation of G1 in the direction of orbital motion in 2004. The major axis angle of the 2D elliptical Gaussian is consistent with a tangent line to the orbit in 2004 and 2005 (10.4±4.0 degrees [tangent to orbit = 12.3±2.8] and 27.4±4.8 degrees [tangent to orbit = 21.0±2.4] west of north, respectively; see Figure 4).

In order to be able to infer the blackbody properties of G1 in a later epoch when the source is compact, we utilize L' and *Ms* data from 2016. As G1 is in a confused region in this epoch, we adopt a different methodology to recover its K' upper limit and L' and *Ms* flux densities. The *StarFinder*-generated backgrounds are subtracted from each main map and we subtract all *StarFinder* identified point sources in the vicinity of our predicted position for G1. We then use the *StarFinder*-generated PSF to do an iterative Lucy-Richardson deconvolution (with 10,000 iterations). Aperture photometry is then performed after beam

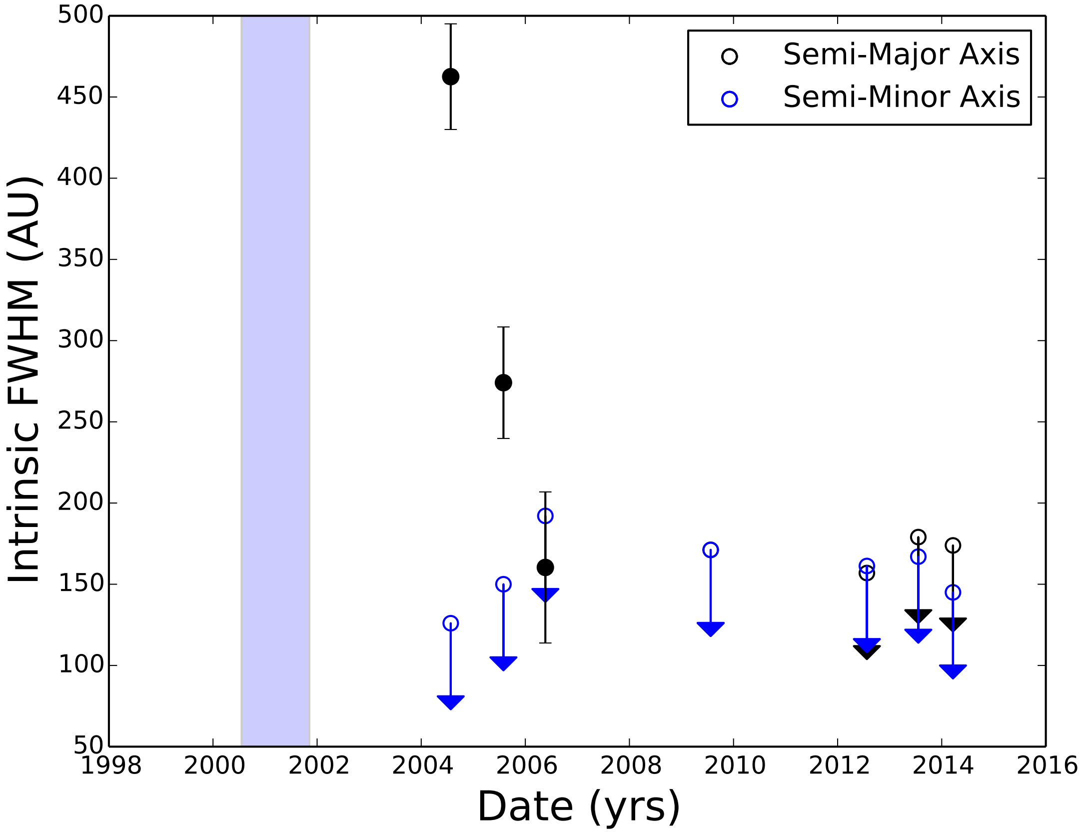

Figure 2.3 Size of G1 as a function of time since periapse passage ($T_0 \sim 2001.3$) in both the semi-major axis and semi-minor axis directions. In the epochs when G1 is resolved, we can get an actual measurement of the semi-major axis of the source; the last four epochs are upper limits on G1's size obtained by first subtracting out the closest neighboring sources in that epoch (S0-2 and Sgr A*), and then comparing the 2-dimensional Gaussian profile of G1 to the point spread function.The light blue bar denotes the FWHM of the 1D marginalized probability distribution function for the periapse passage time.

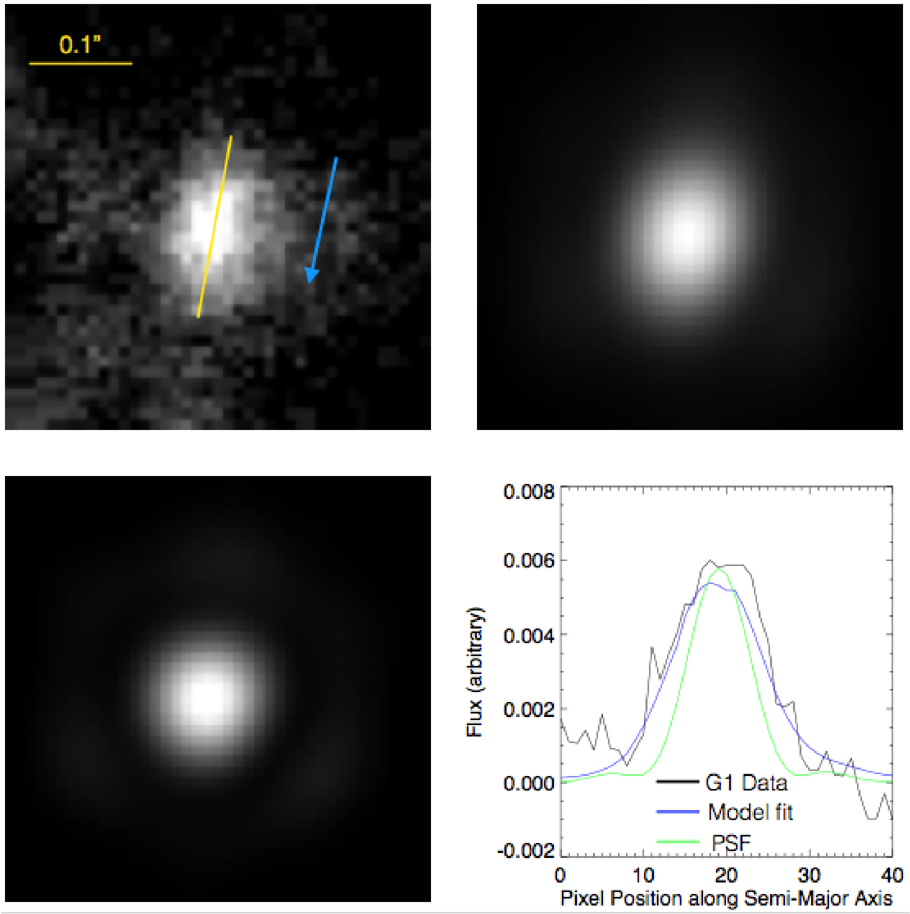

Figure 2.4 *Upper Left*: G1 in 2004 after subtracting all L' *StarFinder*-detected point sources. The angle of the semi-major axis is denoted by the yellow line. The blue arrow shows a line tangent to the direction of orbital motion in 2004. *Upper Right*: Image of 2-D Gaussian fit to the data found using *mpfit2dpeak*. *Lower Left*: PSF model from 2004 as extracted from *StarFinder*. This panel, the upper left, and the upper right panel are all normalized so their peaks are on the same color table and scale; all panels are also on the same physical scale. *Lower Right*: Slice along the semi-major axis for our data (black line), the 2-D Gaussian fit (blue line), and the PSF (green line). It is evident that the 2-D Gaussian fit is an acceptable model for the L' extension and it is much larger than the PSF.

Table 2.2. Data and Observed Properties of G1

Date	ΔRA (arcsec)	ΔDec (arcsec)	K' (mag)	L' (mag)	Ms (mag)	L' Semi-Major Axis Intrinsic Size (AU)	PA of Gaussian 2D fit (deg)
2003.44	-0.077±0.009	-0.059±0.009		13.60±0.54			
2004.57	-0.073±0.009	-0.068±0.008		13.51±0.23		460±30	10.4±4.0
2005.58	-0.069±0.007	-0.860±0.006		13.64±0.05	12.71±0.30	270±30	27.4±2.4
2006.39	-0.065±0.006	-0.103±0.006		13.87±0.12		160±50	16.0±9.8
2009.56	-0.035±0.006	-0.131±0.010		14.38±0.66		<170	
2012.56	-0.029±0.006	-0.162±0.007		15.21±0.12		<160	
2013.55	-0.012±0.006	-0.169±0.006	>18.8	15.22±0.19		<180	
2014.22	0.002±0.006	-0.183±0.009		15.51±0.15		<170	
2014.36	0.003±0.006	-0.196±0.006		15.27±0.21			
2014.50	0.003±0.006	-0.193±0.007		15.53±0.23			
2014.59	0.006±0.006	-0.185±0.007		15.32±0.19			
2016.38	0.017±0.004[a]	-0.202±0.004[a]	>18.2[b]	15.50±0.36[b]	14.81±0.23[b]		

[a] These positions come from our orbital solution derived from our L' data taken from 2003 through 2014. See section 3.3 for more information on our orbital fit.

[b] The photometry in 2016 was derived using deconvolved images rather than *StarFinder*, as done in previous epochs. See section 3.1.2 for more information.

Table 2.3. Radial Velocity Data

Date	Radial Velocity km/sec	PSF FWHM mas at Br-γ	Orig. Publication
2004.6	-2043$\pm$150		Pfuhl et al. 2015
2006.2	-1594$\pm$163		Pfuhl et al. 2015
2006.5	-1558$\pm$60	67	This Paper
2008.3	-1123$\pm$159		Pfuhl et al. 2015

restoring at the predicted position of G1 based on its derived orbit from the 2003 - 2014 data. The photometry of the 2016 L' data matched well with the 2014 epochs.

2.3.2 Spectroscopic Analysis

The radial velocity for G1 was obtained using a similar approach to that developed by Phifer et al. (2013) for G2. Specifically, a spectrum of G1 was extracted at a location in our OSIRIS data that was found by transforming the 2005 L' star list, which is high quality and close in time (as the OSIRIS data is from 2006.497), to the OSIRIS reference frame using a second-order polynomial transformation. The spectrum was extracted using an aperture radius of 1 pixel (corresponding to 35 mas) and doing a local sky subtraction in an area clear of known contaminating stars (e.g., Do et al. 2013b). The extracted spectrum was calibrated using the standard techniques (Do et al., 2009b), and the peak in the resulting spectrum was fit with a Gaussian model to derive an observed radial velocity and full-width at half-maximum. The resulting heliocentric radial velocity was corrected by 3.64 km sec^{-1} to correspond to an LSR velocity of -1568 ± 60 km sec^{-1} on the date of the observation (see Table 3). The FWHM of the spectral line is 185 ± 41 km sec^{-1}. The spectrum and the corresponding point source in the line emission map are shown in Figure 5.

We compute the Br-γ line luminosity similarly to Phifer et al. (2013) by comparing S0-2's flux density to G1's flux density. We estimate S0-2's dereddened flux density to be 14.1 ± 0.2 mJy (assuming the extinction prescription outlined in Schödel et al. 2010 and the flux

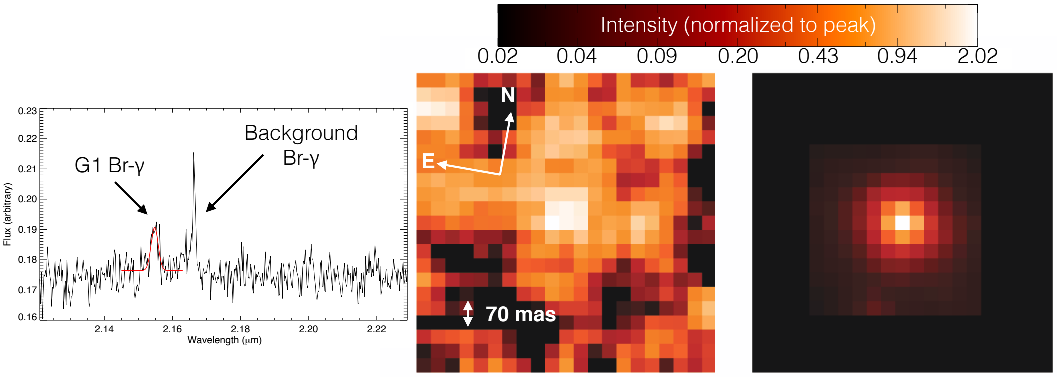

Figure 2.5 *Left*: Continuum-subtracted spectrum of G1. The emission line at 2.154 μm corresponds to a radial velocity of -1568 ± 60 km/sec. This spectrum was extracted using an aperture of 1 pixel (35 mas) radius from our 2006 OSIRIS data cube. The overplotted red line shows the 1-dimensional Gaussian fit. *Center*: Continuum-subtracted OSIRIS data cube collapsed over a Δv of 267 km/sec centered on -1568 km/sec (LSR-corrected) and smoothed over 2 spatial pixels. *Right*: Br-γ point spread function extracted from our 2006 OSIRIS data cube. Both the PSF and the collapsed cube are displayed on the same physical scale and same logarithmic color scale where we normalize each figure to its respective peak.

density from Ghez et al. 2008) and compute an expected luminosity of S0-2 over the 2.15 - 2.159 μm bandpass to be 0.16$L_{\odot}$. We then integrate over the same bandpass on the S0-2 and G1 spectra to get a final Br-γ luminosity of G1 of 1.48 ± 0.17 milli-$L_{\odot}$. To check for consistency, we followed this same procedure to integrate over the same bandwidth for G2 (2.17 - 2.179 μm), which yields a Br-γ luminosity of 1.36 ± 0.25 milli-$L_{\odot}$, consistent within 1σ of the 2006 G2 luminosity reported in Phifer et al. (2013).

Using this dereddened Br-γ line luminosity from 2006 (in an epoch where G1 is resolved), we can estimate what the Lyman-α emission luminosity. We used the relationship between the Br-γ emission and the free-free emission given in **?** and solved for the Lyman-α luminosity using the formulae summarized in **?** and **?**. We estimate that the Lyman-α luminosity is ∼2 $L_{\odot}$.

2.3.3 The Orbital Determination of G1

To derive the orbital properties of G1, we jointly fit for the Keplerian orbital parameters of S0-2, S0-38, and G1 (period, epoch of periapse passage, eccentricity, position angle of the ascending node, argument of periapse, and inclination for each source) and the black hole parameters (the two-dimensional position, the three-dimensional velocity, and the mass of and distance to Sgr A*; see Table 4). S0-2 and S0-38 have complete orbital phase coverage and drive the black hole parameter fit. We use the same astrometry and radial velocities of S0-2 and S0-38 as reported in Boehle et al. (2016) with additional 2014 data added to reflect the longer time baseline of our observations. Jointly fitting the three sources maximizes the amount of information we currently have available, particularly since G1 does not have enough kinematic information to independently fit for the black hole parameters due to the lack of orbital phase coverage. We impose uniform, flat priors on each of the orbital parameters for G1 as follows: [0, 360] degrees for the argument of periapse (ω); [0, 180] degrees for the position angle of the ascending node (Ω); [0, 180] degrees for the inclination; [0, 1] for the eccentricity; [0, 6000] years for the period; and [1990, 2010] for the time of periapse passage. We fit only bound Keplerian orbits. In order to characterize possible

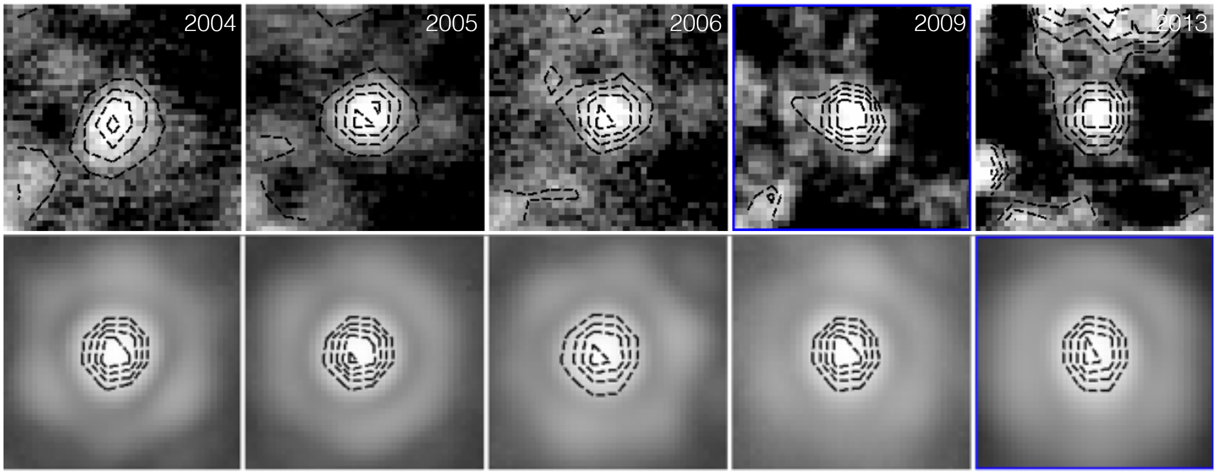

Figure 2.6 *Top*: Source-subtracted images centered on G1 that are 0.4 arcseconds on a side. Each image is photometrically normalized to a constant flux. *Bottom*: Point spread functions corresponding to the epochs in the top row. The contours show intensity levels on the same levels as those in the top row. G1 is extended in 2004 - 2006, whereas G1 is compact after 2009.

systematic sources of uncertainty, we perform an additional analysis with fixed black hole parameters (the position and velocities are fixed at zero).

The G1 astrometry consists of 11 data points (see Section 3.1), including our newest astrometric measurements. Source confusion is a significant source of systematic error in our orbital fits and the formal uncertainties are therefore underestimated. In order to account for this, we fit a second-order polynomial to our astrometric data points and add a single additive value in quadrature to the formal errors until the final reduced chi-squared of the second-order fit (that includes position, velocity, and acceleration) is equal to 1.0. The resulting additive value is 5.5 mas which is roughly comparable to the formal uncertainties. For this orbital fit, we also we used three radial velocity measurements reported in Pfuhl et al. (2015) and our new measurement (Section 3.2; Table 3).

Table 2.4. S0-2 + S0-38 Black Hole Parameter Values

Orbital Parameter	Peak Fit[a]
X-Position of Sgr A* (x_0, mas)	$2.1^{+0.5}_{-0.3}\pm1.90$
Y-Position of Sgr A* (y_0, mas)	$-4.4\pm0.4\pm1.23$
ΔRA Velocity of Sgr A* (V_x, mas/yr)	$-0.12^{+0.03}_{-0.02}\pm0.13$
ΔDec Velocity of Sgr A* (V_y, mas/yr)	$0.68\pm0.05\pm0.22$
Radial Velocity of Sgr A*(V_z, km/sec)	$-20.4\pm6.3\pm4.28$
Distance to Sgr A* (R_0, kpc)	7.87 ± 0.11
Mass of Sgr A* (M, Millions of $M_\odot$)	$3.93^{+0.07}_{-0.13}$
S0-2 Parameters:	
Time of closest approach (T_0, years)	2002.346 ± 0.003
Eccentricity (e)	$0.892^{+0.002}_{-0.001}$
Period (P, years)	$15.93^{+0.02}_{-0.05}$
Angle to periapse (ω, degrees)	$66.8^{+0.3}_{-0.5}$
Inclination (i, degrees)	134.3 ± 0.3
Position angle of the ascending node (Ω, degrees)	$228.0^{+0.4}_{-0.5}$
S0-38 Parameters:	
Time of closest approach (T_0, years)	$2003.191^{+0.038}_{-0.017}$
Eccentricity (e)	0.811 ± 0.003
Period (P, years)	$19.22^{+0.1}_{-0.2}$
Angle to periapse (ω, degrees)	13^{+15}_{-21}
Inclination (i, degrees)	169 ± 2
Position angle of the ascending node (Ω, degrees)	94^{+18}_{-14}

[a] The peak and corresponding 1σ errors are from the marginalized one-dimensional distributions for the respective parameters. The first error term corresponds to the error determined by the orbital fit itself, while the second error term on the black hole parameters refers to uncertainty in the reference frame and was determined by Boehle et al. (2016).

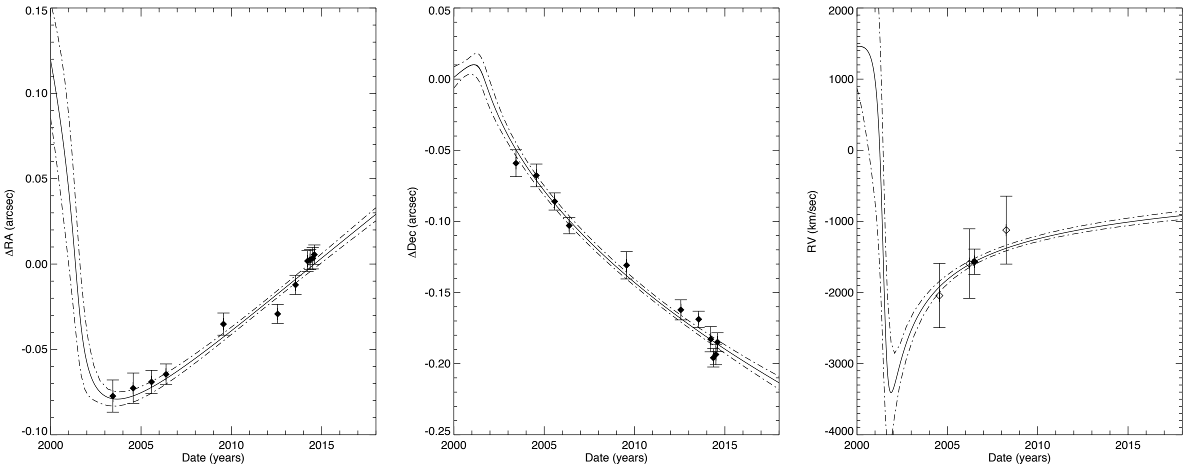

Figure 2.7 G1's kinematic measurements and best fit orbital motion models. Our 11 astrometric and 1 radial velocity measurements are shown as filled points. The three RV measurements from Pfuhl et al. (2015) are plotted as unfilled points. The 1σ uncertainty envelopes are shown as broken lines for the first three orbital plots.

2.4 Results

Our analysis of both photometric and spectroscopic information and our Keplerian orbital fit have led to three key results: G1 follows a highly eccentric Keplerian orbit that differs from G2's orbit; shortly after periapse, G1's L' emission is extended along the direction of orbital motion; and G1's L' emission is much larger than the tidal radius of even a $100\mathrm{M}_\odot$ source shortly after periapse, indicating that this emission comes from material that is not gravitationally bound to G1.

2.4.1 Keplerian Orbital Fit Results

The orbit of G1 is consistent with Keplerian motion (see Figures 7 and 8). Based on our precise astrometry and radial velocity points, G1 lies on a highly eccentric orbit ($e = 0.99^{+0.001}_{-0.01}$) and has recently passed through periapse ($T_0 = 2001.3 \pm 0.4$). The three orbital angles (position angle of the ascending node [$\Omega; 87.1^{+5.0}_{-4.9}$], argument of periapse [$\omega, 117.3^{+2.8}_{-2.9}$], and inclination [$i; 109.0^{+0.9}_{-0.8}$]) are well-constrained, but the orbital period is very poorly con-

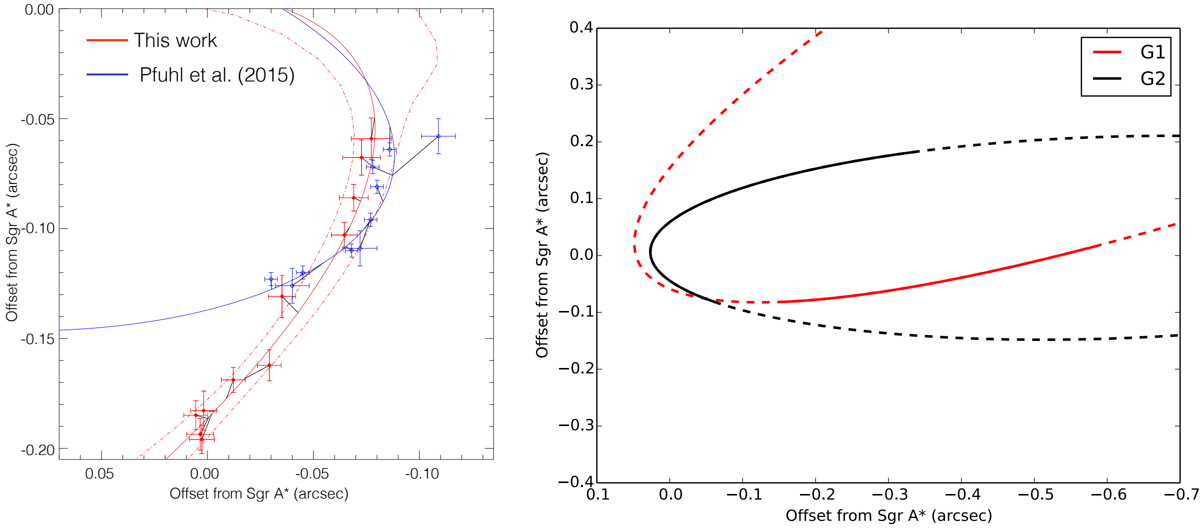

Figure 2.8 *Left:* Comparison of G1's orbital solution between this work and Pfuhl et al. (2015). Our Keplerian orbital fit is shown in red, while the orbital fit and data from Pfuhl et al. (2015) are shown in blue. The black lines connect the observed point to the same point in time on the model orbit. There is an astrometric bias in 2009 and 2010 from confusion or a background dust emission feature that may skew the astrometry in those epochs. We do not use the astrometry from Pfuhl et al. (2015) due to differing reference frames. *Right:* Orbits of G1 and G2 (as described by Table 5) projected into their common average orbital plane ($\Omega_{G1} = +2.5$ deg; $\Omega_{G2} =$ -2.5 deg; $i_{G1} =$ -2 deg; $i_{G2} = 2$ deg; $\omega_{G1} = 117$ deg; $\omega_{G2} =$ 96 deg). It is evident that despite having similar orbital planes, the orbital trajectories are different. The solid (dotted) lines show times when we have (have not) observed G1 and G2.

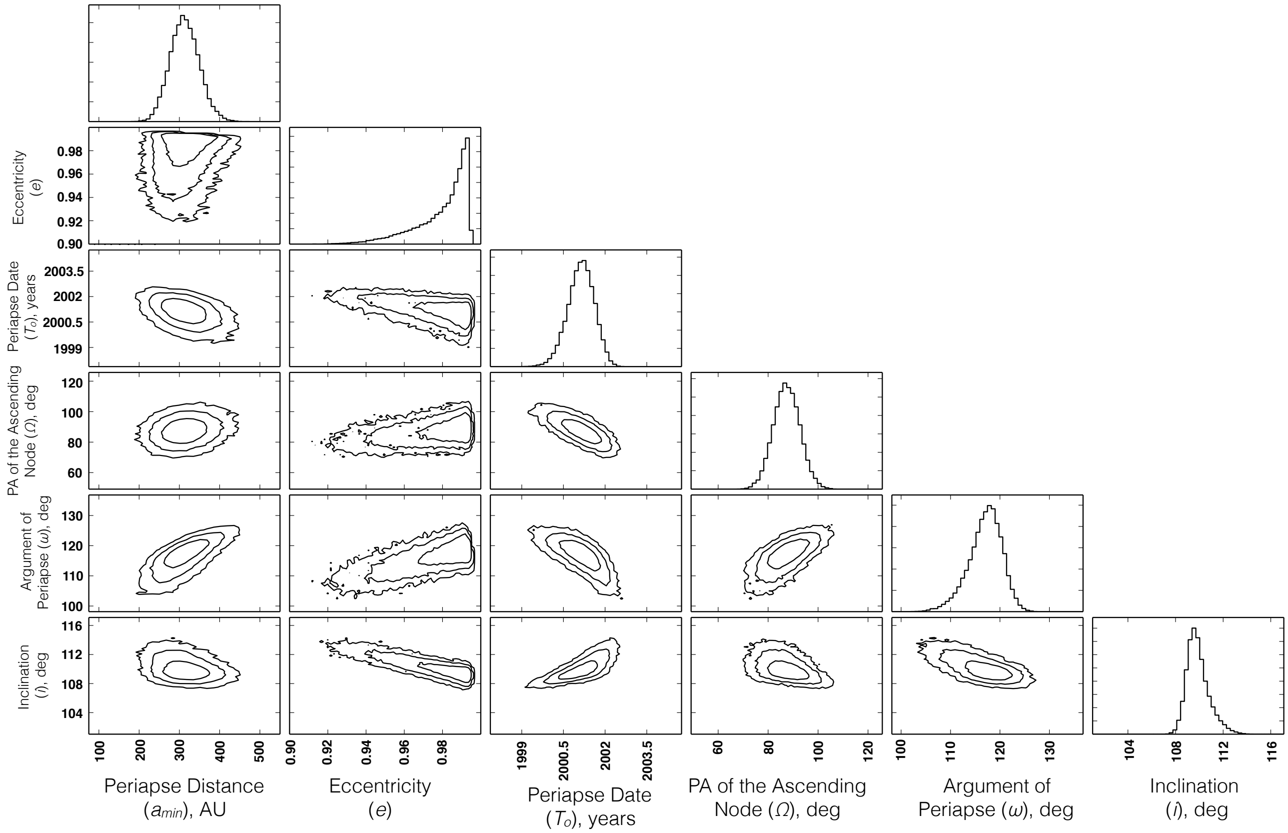

Figure 2.9 One-dimensional marginalized probability distribution functions for the six Keplerian orbital parameters for G1 (black 1, 2, and 3σ contours), along with the joint probability distribution functions for all parameters.

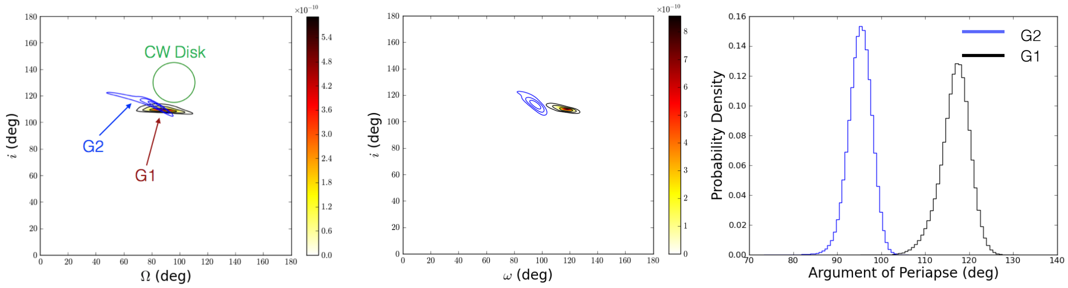

Figure 2.10 Joint probability distribution functions showing G1 (black) and G2 (blue) 3σ contours. While G1 and G2 may have a similar orbital orientations, as shown in the Ω vs. i plot (*left*), their arguments of periapse (ω) differ by greater than 3σ, implying that they have different orbits (*center, right*). The clockwise disk's orientation and width are overplotted on the Ω vs. i plot to show the orientation of the orbital plane's proximity to the clockwise-moving disk of young stars.

strained due to lack of orbital phase coverage. The best-fit orbit is shown in Figure 8 and the peak of the 1-dimensional marginalized probability distribution functions along with the maximum likelihood best fit are presented in Table 5. We only fit bound, closed orbits; G1 could be on a hyperbolic orbit since the eccentricity distribution is artificially truncated. The period restriction of P <6000 years also constrains our orbital fits.

Figure 7 shows our orbital plots, our extracted G1 astrometry, and radial velocity measurements. Figure 8 presents our projection of the orbit onto the sky and compares it to the orbital solution from Pfuhl et al. (2015) while assuming the black hole parameters from Gillessen et al. (2009). Our orbit covers almost twice the time baseline presented in Pfuhl et al. (2015). It is evident that our orbital solution is significantly different compared to the orbit of G2 (e.g., Gillessen et al. 2012, 2013b; Phifer et al. 2013; Meyer et al. 2013).

2.4.2 Size Variation

In the epochs closest to periapse, G1 is extended along the direction of orbital motion (the semi-major axis). Figure 4 shows the intrinsic extension of G1 corrected for the size of the PSF along both the semi-major and semi-minor axes. The source is approximately

Table 2.5. Orbital Parameters for G1 and G2

Parameter	Best Fit, G1	Peak, G1[b]	Best Fit, G2[c]	Peak, G2[c]	G1 Fit Pfuhl et al. (2015)
Time of closest approach (T_0, years)	2001.0	$2001.3^{+0.4}_{-0.2}$	2014.1	$2014.2^{+0.03}_{-0.05}$	2001.6±0.1
Eccentricity (e)	0.981	$0.992^{+0.002}_{-0.01}$	0.962	$0.964^{+0.036}_{-0.073}$	0.860±0.050
Periapse Distance (A_{min}, AU)	277	298^{+32}_{-24}	193	201 ± 13	417 ± 239
Argument of periapse (ω, degrees)	118	117±3	95	96±2	109±8
Inclination (i, degrees)	109	109±1	112	113±2	108±2
Position angle of the ascending node (Ω, degrees)	89	88^{+5}_{-4}	83	82±2	69±5

[a] The parameters of Sgr A*are extracted as described above.

[b] The errors reported here are the 1σ errors taken from the marginalized one-dimensional distributions for the respective parameters.

[c] G2 parameters are from performing an orbital fit on our available astrometric and spectroscopic points (those outlined in Meyer et al. 2013) in the same fashion described in Section 3.3.

[d] The clockwise disk parameters are i=130±15 deg and Ω=96±15 deg, where 15 deg reflects the half-width at half-maximum from the peak density of the clockwise disk as reported in Yelda et al. 2014.

elliptic and the semi-major axis of an elliptical 2D Gaussian fit is rotated in the direction of linear motion (Figure 5). However, in the more recent epochs, G1 becomes more compact. Additionally, there is significant brightness variation of G1 at L' post-periapse passage, which corresponds directly to its size evolution: when G1 is at its largest size, it is also brightest; when G1 is compact, it is ∼2 magnitudes dimmer. The arrows in Figure 4 show the intrinsic (PSF-size corrected) upper limits on the source size along the semi-major and semi-minor axes, which is on average ∼170 AU along the semi-major axis assuming $R_0 = 8$ kpc.

Figure 6 shows images of G1 with all neighboring point sources identified by *StarFinder* subtracted. The contours illustrate the size development of G1. The full-width at half-maximum of the semi-major axis of G1 is as high as 463 ± 16 AU in 2004.567 after correcting for the PSF contribution (see Figure 3), but decreases to the size of a point source after 2006. Figure 11 also shows azimuthally-averaged radial profiles of G1 from 2009 through 2014, showing that the size of G1 is indeed consistent with a point source.

Our 2006 Br-γ detection is quite shallow and we are unable to determine whether G1 is resolved at Br-γ. Due to the shallowness of the Br-γ detection, we are unable to conclude if G1 is spatially resolved or has a velocity gradient.

2.4.3 Photometry and Temperature of G1

There is a large photometric difference (∼2 magnitudes) between the epochs when G1 is extended (2004, 2005, and 2006) and when it is point-like. The brightness develops with size, as epochs when G1 is extended are brightest, and epochs when G1 is point-like are dimmer and remain at a constant magnitude from 2012 through 2016.

G1 is identified at L' and Ms ($L' = 13.65$ in 2005; $Ms = 12.71$ in 2005), but not at K' ($K' > 18.8$ in 2013). Assuming zero-point fluxes for L' from Tokunaga (2000) and the extinction law outlined in Schödel et al. (2010), we infer a dereddened L' flux of 2.7 ± 0.5 mJy in 2005.

In order to infer a temperature for G1 at a moment in time (2005) when G1 is extended enough to be resolved, we expect it to be optically thin, and therefore use a modified blackbody:

$$I_\nu \propto Q_0 \left(\frac{\nu}{\nu_0}\right)^\beta B_\nu(T_{dust}) \tag{2.1}$$

where ν_0 is the frequency at which the temperature is calculated, where Q_0/ν_0^β is a constant, and where B_ν is the Planck function. We take the power-law index β equal to 2, as in Lau et al. (2013) and consistent with extinction curves from Draine (2003). We separately do the same calculation assuming $\beta = 0$ (blackbody). The temperature is therefore calculated following the equation:

$$L' - Ms = -2.5 \log \left[\left(\frac{\nu_{L'}}{\nu_{Ms}}\right)^\beta \frac{B_{L'}(T_{dust})}{B_{Ms}(T_{dust})} \right] \tag{2.2}$$

From our L' and Ms measurements, we are able to obtain a dereddened color (L' - Ms) of 0.706. Fitting a modified blackbody following equation 2 with $\beta = 2$, the color temperature we obtain from our 2005 data is equal to 568 ± 44 K; assuming a blackbody ($\beta = 0$), we obtain a 2005 temperature of 426 ± 44 K where our error bars are computed via a Monte Carlo simulation.

Using our L' and Ms photometric data in 2016 when G1 is observed to be point-like and assuming that G1 behaves as a blackbody in this epoch (β=0), we infer a blackbody temperature of 684 ± 75 K (where our error bars are again computed via a Monte Carlo simulation). Therefore, our inferred blackbody temperature has increased from 2005 to 2016.

2.5 Discussion

G1 is a cold, extended source that has tidally interacted with Sgr A* and survived at least 13 years past periapse passage. It has observable parameters that seem to be consistent with other examples of infrared excess sources at the Galactic Center, the most prominent of which is G2. Many of its orbital and observable properties are comparable with those of G2: its cold temperature (426 K if $\beta = 0$, or 568 K if $\beta = 2$ in 2005; 684 ± 75 K if $\beta = 0$ in 2016), its highly eccentric orbit ($e = 0.99^{+0.001}_{-0.01}$), and the orientation of the orbital plane (see Table 5). There is a measurable size change post-periapse passage, and the L' flux density also changes dramatically after periapse. In the following, we discuss the similarities and differences between G1 and G2.

2.5.1 Is G1 part of a gas streamer common with G2?

Pfuhl et al. (2015) have recently proposed that G1 and G2 are not only lying in the same orbital plane, but follow the same trajectory. They speculate that the Keplerian orbits of G1 and G2 are closely related and they postulate the small deviations between the orbits of the two objects are due to the drag force from the ambient Galactic Center medium. This additional drag force leads to an evolution of G2's orbit into G1's orbit over time. Similarly, McCourt & Madigan (2015) and Madigan et al. (2016) use G1 and G2 as probes to constrain the properties of the accretion flow surrounding Sgr A*. They model the orbital differences (as found by Pfuhl et al. 2015) between G1 and G2 in terms of an interaction with the background flow (McCourt & Madigan, 2015) and in the accretion flow onto Sgr A* (Madigan et al., 2016). Based on their orbital analysis, they conclude that both sources could have originated from the clockwise young stellar disk (Paumard et al., 2006b; Lu et al., 2009; Yelda et al., 2014).

However, the study we present here, which includes data taken several years beyond the last data point used in Pfuhl et al. (2015) (2014.6 vs. 2010.5; true anomalies of 10.5 and 8.7 degrees, respectively), shows that despite the common orbital plane, G1 and G2 have distinct Keplerian orbits with a significant ($>3\sigma$) difference of their arguments of periapse, $\sim$3 times larger than the difference reported in Pfuhl et al. (2015). This is demonstrated in Figure 8, showing both the data and the best-fit orbits projected into the plane of the sky as well as both best-fit orbits projected into the average orbital plane.

In order to test whether the reference frame derived from our three-star-fit would affect the orbital parameters of G1 and G2, we forced the black hole to be at rest, at the origin of our coordinate system, and fixed the mass and distance to be the peak values reported in Table 4. As shown in Figure 2.11, the ω vs. i plots do not change for G1, but do for G2. In fact, the 3σ contours for G2 move further away from G1's contours. Therefore, the two orbits are still inconsistent with each other at greater than 3σ significance even with fixed

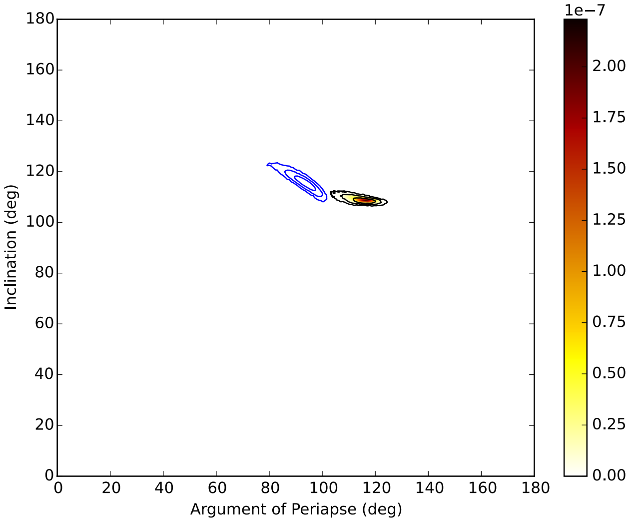

Figure 2.11 Same plot as the center panel of Figure 10 but with the black hole parameters fixed so that there is no movement and so that the mass and distance are fixed to the peak values reported in Table 4. The 3σ contours for G1 do not really move in inclination vs. ω space, but the contours of G2 do move slightly away from G1.

black hole parameters.

While the model proposed by McCourt & Madigan (2015) and Madigan et al. (2016) might be able to accommodate such a large shift of the Keplerian orbit in the case of a compact gas cloud, the drag force scenario and a resulting common trajectory of G1 and G2 become increasingly unlikely for increasing mass of these two bodies. We believe that the compactness of both sources is indicative of a higher mass. The masses derived in the following sections and in Witzel et al. 2014 are 10^5 - 10^6 times larger than the original proposed 3 Earth masses. The interpretation in Pfuhl et al. (2015) that G1 and G2 are two dense regions within the same extended extended gas streamer that fills one trajectory around the black hole and have an identical origin, but are offset by ∼13 years, therefore seems unlikely.

We do not exclude the possibility that G1 and G2 originate from the same plane, in particular the clockwise disk of young stars (Yelda et al., 2014; Madigan et al., 2014) as the orbital plane angles of G1 and G2 (Ω and i) are fairly close to the position of the clockwise disk (see Figure 10, Pfuhl et al. 2015). We note, however, that there are other G2-like sources that do not lie on their common orbital plane (Sitarski et al. in preparation).

2.5.2 Gas Cloud or Star?

Independently of whether G1 and G2 are related by a gas streamer, the physical natures of G1 and G2 are still not yet known. Recent results (e.g., Witzel et al. 2014, Valencia-S. et al. 2015, in contrast to Pfuhl et al. 2015) support the hypothesis that that G2 has a stellar component due to its periapse passage survival. This raises the question of whether there is similar evidence that G1 is stellar in nature.

In contrast to the unresolved source G2 at L', for G1 we are able to measure its size in 2005 and we can therefore put constraints on the optical depth, τ of the dust envelope at this point in time. Based on several parameters calculated in Section 4.3 ($T_{\beta=2} = 568$ K; $T_{\beta=0} = 426$ K; $r_{G1,2005} = 137$ AU), we find that the optical depth of G1 is small in the epochs when it is resolved and we can therefore conclude that the origin of continuum emission is an optically thin medium in 2005. As calculated in Section 3.2, the ambient radiation field in the Galactic Center is strong enough to externally heat this optically thin envelope via Lyman-α heating. The profile of G1 in the epochs when it is extended is well constrained by a PSF convolved with a 2D Gaussian (see Section 3.1.2) and shows no evidence of two components (as could be modeled by a PSF + a 2D Gaussian). This indicates that we do not see a central, optically-thick point source in 2005.

From 2009 onwards, G1 is unresolved at L' and shows a significantly lower, roughly constant flux density of $\sim$0.6 mJy. Blackbody modeling of G1's L' - Ms color yields a temperature of 684 K, implying a blackbody radius of $\sim$1 AU and a luminosity of $\sim$4.5 solar luminosities. This high luminosity and the fact that the object became more compact with time point to a substantially larger mass than 3 Earth masses. As indicated by the evolutionary tracks of main sequence stars, this mass can be of the order of a solar mass (Figure 2.12). However, the large derived blackbody size for the unresolved G1 shows that it is neither a main sequence star nor is G1 luminous enough to be a Red Giant.

The material at the enormous distance of $r \sim 230$ AU of the outer halo seen in the extended epochs certainly remains unbound from G1 to even much higher masses of G1 than 1 $\mathrm{M}_\odot$; in fact, this holds true for a central mass that is two orders of magnitude higher due to the weak $M^{1/3}$ dependence of the tidal radius. Figure 15 shows the tidal radius (black lines) of a $2\mathrm{M}_\odot$ source (solid line) and a $100\mathrm{M}_\odot$ source (dashed line; see Witzel et al. 2014) plotted with the measured HWHMs of G1. Therefore this material is stripped and its emission falls below the detection limit as its density decreases or dust grains are destroyed by X-rays and high-energy particles generated in the accretion flow (e.g., Lau et al. 2015 and references therein; Tielens et al. 1994)[2]. It is interesting to note that the minimal radius of material that remained bound throughout periapse for a G1 mass of 1 $\mathrm{M}_\odot$ and the periapse passage distance of ~300 AU is 1 AU (see Figure 14, which plots the tidal radius as a function of time since periapse passage for G1 and G2). This corresponds nicely to the derived blackbody radius in 2016.

The question remains how G1 has reached the enormous extension of $r = 230$ AU in 2004. This most certainly requires that G1 was large at periapse passage. From an energy argument, we determine the lower limit of the size of G1 at periapse passage from the maximum shearing velocity of the object in the potential of the black hole according to the following equation:

$$\left(\frac{r_{obs} - r_{per}}{}\right)^2 = \left[\sqrt{v_*^2 - 2GM_{BH}\left[\frac{1}{d_*} - \frac{1}{d_* - r_{per}}\right]} - v_*\right]^2 - \frac{2Gm}{r_{in}} \tag{2.3}$$

where r_{obs} is the observed size in 2004, r_{per} is the half-width along the Sgr A*-G1 line, v_* is velocity of G1 at periapse passage, m is the mass of G1, M_{BH} is the mass of the supermassive black hole from Table 5, is the difference between our observation date (2004.6) and periapse passage time, the first epoch where we see a resolved G1, and d_* is the distance of the center

---

[2] *Fermi*, HESS, and VERITAS all report a bright unresolved point source of high energy coincident with Sgr A*, and both G1 and G2 are within their central resolution element (e.g., Ajello et al. 2016; Aharonian et al. 2004; Archer et al. 2014)

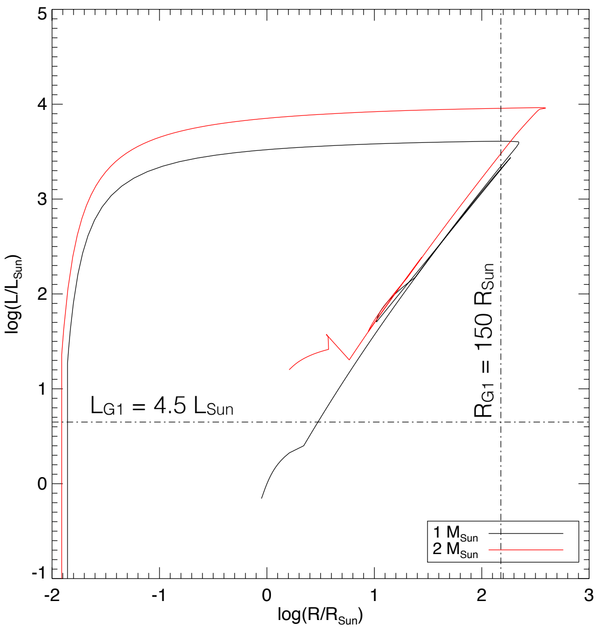

Figure 2.12 Luminosity plotted against radius of two main sequence stars at M $= 1$ M$_\odot$ and M $= 2$ M$_\odot$ using the SSE code (Hurley et al., 2000). The vertical and horizontal lines show our inferred blackbody values for G1 from our 2016 data set. It is clear that the luminosity we infer for G1 is too small for a source we see of that radius.

of G1 to the Sgr A*. Simultaneously solving for m and r_{per}, we find that r_{per} is larger than 21 AU at the time of closest approach and that the solution is not strongly mass dependent.

Therefore, for G1 to be so large in 2004, it must be $\geq$21 AU at periapse passage and it was likely a large object even before it started interacting with the SMBH. If G1 was intrinsically an object with a radius of 4, 3, or 2 AU before it started to be tidally sheared, it would have began interacting with the SMBH 1.3, 0.9, and 0.4 years before periapse passage, respectively, giving it plenty of time to grow to be the large source we infer for periapse passage.

It is possible that G1 appears extended at L' because of confusion with background sources. However, this seems unlikely for several reasons. We have traced the orbits of all known stars close to G1 and Sgr A*, and G1 is certainly not confused with a bright (mag$_{L'}$ < 16) source. But it is not fully excluded that, during the early epochs, there could be several dim stars whose images are overlapping that of nearby G1 for multiple epochs before separating and moving below the detection limit again. However, the symmetry in the extended residual after subtracting a point source makes this seem rather unlikely.

In summary, our model for G1's dust shell is as follows: G1 started tidally interacting with the SMBH with a rather large size several years prior to periapse passage. The tidal radius penetrated deep into the dust shell ($r \sim 1$ AU) and the outer part of the optically thick shell became unbound from the source. This unbound shell became optically thin and externally heated by the surrounding radiation field in the Galactic Center, which is what we observe starting in 2004. Over time, the tidally stripped dust fell below the detection limit, and by 2009, we see the optically thick shell a massive, internally-heated central object as a point source that is 2 magnitudes fainter than what is observed in 2004. Throughout all epochs, the source is also surrounded by an externally-heated gas envelope that we observe as Br-γ emission. One possible physical explanation for G1's large size is that it could be an example of a black-hole-driven binary merger product (Phifer et al., 2013; Witzel et al., 2014; Prodan et al., 2015).

Several predictions have been made for the post-periapse development of G2 in the case of a pure gas cloud. G1 and G2 have similar periapse passage distances and blackbody sizes (as inferred in Section 5.3 for G1), and we expect them to tidally interact with the black hole in a comparable manner. Thus, in the following, we compare G1's post-periapse observables to some of these predictions for G2.

Various models for G2 predict that if it were a pure gas cloud, it should undergo tidal shearing within 1 to 7 years after periapse. The Br-γ flux of G2 was predicted to rapidly decrease over time (Anninos et al., 2012; Morsony et al., 2015), both due to the break-up of G2 and the heating of its gas. Observationally, the latest Br-γ line detection of G1 occurred in 2008, 7 years after periapse passage (Pfuhl et al., 2015)[3], not showing any indication of a strong decay or complete depletion. In fact, the post-periapse luminosity of G1 is consistent with the pre-periapse luminosity of G2 (see section 3.2). We also note that G1's FWHM in 2006, 5 years after periapse passage, was 185 km sec^{-1}, comparable to the line width

---

[3] In epochs later than 2008, it is extremely difficult to extract due to lack of sufficient data quality.

of G2 five years before its periapse passage in 2014. (Phifer et al., 2013) This provides strong constraints on future hydrodynamic modeling of the post-periapse development of these objects.

Unlike G2's flux density staying constant before and during periapse (Witzel et al., 2014), G1's L' flux significantly decreased post-periapse (Figure 2). The size of G1 at L' shows a similar development over time from a clearly resolved, optically thin source two years after periapse to an unresolved, compact source five years post-periapse passage. Our calculation in the previous section indicates that G1 went through periapse passage with a radius > 21 AU. These findings are indicative of G1's dust envelope interacting more strongly with Sgr A* than that of G2 due to its smaller mass and larger size. While they have similar tidal radii close to periapse passage, G1 interacts with the SMBH for a longer period of time than G2.

Several studies (e.g., Schartmann et al. 2012; Anninos et al. 2012; Gillessen et al. 2012, 2013a; Morsony et al. 2015) find that if G1 or G2 were a gas cloud, there should be a significant increase in the steady-state X-ray flux several months before and after periapse passage due to shocks. The *Chandra X-ray Observatory* was launched in 1999, and the earliest observations of Sgr A* were conducted in late 1999 and 2000. Baganoff et al. (2001) and Ponti et al. (2015) show no indication of an increase in the the steady-state X-ray flux in the time around G1's periapse passage (2001.3 ± 0.4; figure 3 in Ponti et al. 2015).

The size evolution of G1 in L', along with the distinct Keplerian orbits described in section 5.1, the intact Br-γ emission after 7 years, the survival of G1 at L', and the lack of an increased X-ray flux, all provide evidence that G1 has a massive ($\sim$1 $M_\odot$) central (stellar) component surrounded by an envelope of gas and dust, similar to our hypothesis for G2 (Witzel et al., 2014). Even if the mass of G1 is smaller than 1 $M_\odot$, it is still $\sim 10^5$ times larger than the masses suggested for a gas cloud (Gillessen et al., 2012; Pfuhl et al., 2015).

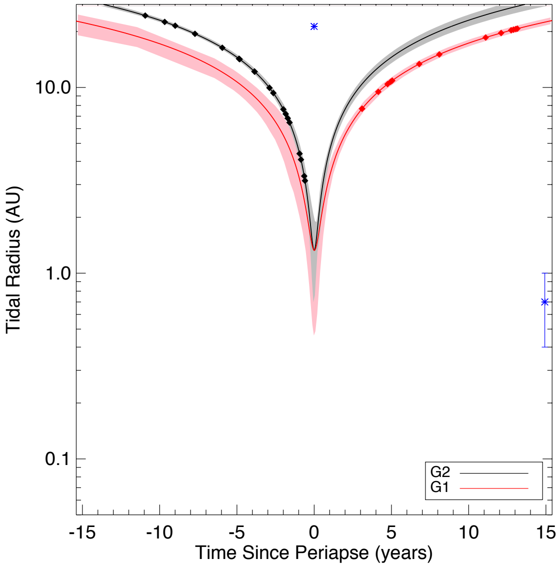

Figure 2.13 Plot of the tidal radii of G1 (red) and G2 (black). The tidal radius for G1 is computed assuming a mass of 1.0 $M_{\odot}$, consistent with our luminosity calculation described in section 5.2. The first blue asterisk denotes the inferred size of G1 at periapse passage calculated with our dynamical model; the second blue asterisk shows the inferred size assuming that G1 is a blackbody in 2016. The latter is consistent with 1.0 AU, the deepest point of direct tidal interaction of G1 with Sgr A^*. G1 has a longer interaction with Sgr A^* than G2 does.

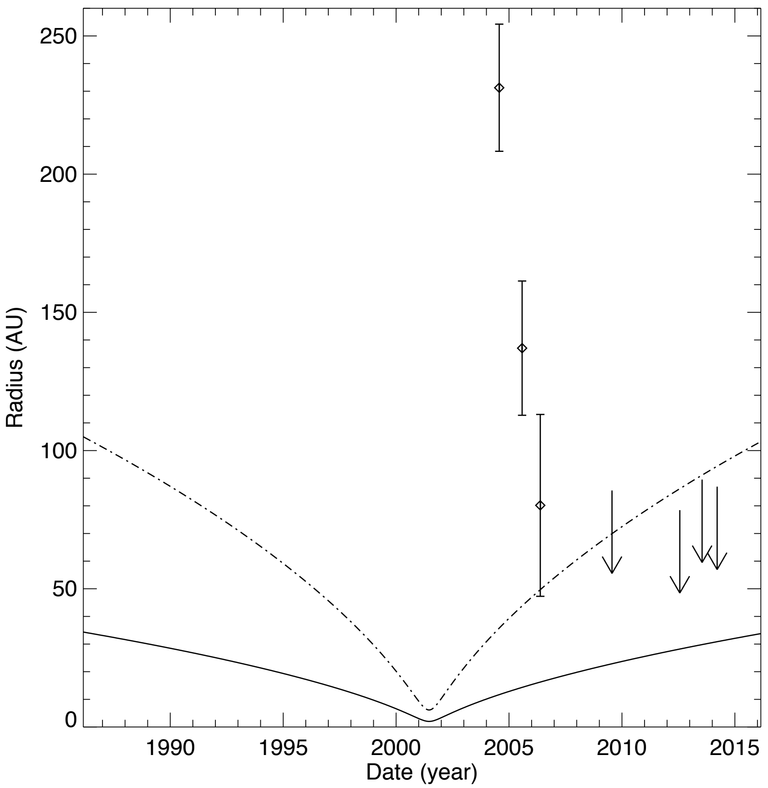

Figure 2.14 Tidal radius as a function of time since periapse passage for G1. The solid line shows the tidal radius of a $2M_\odot$ main-sequence star (as found for G2 in Witzel et al. 2014); the dashed line shows the tidal radius of a $100M_\odot$ star. The intrinsic size of the semi-major axes of G1 from Figure 3 are over-plotted as well. It is evident that in the epochs where G1 is large, it lies well outside the tidal radius and therefore can interact gravitationally with Sgr A*. Therefore, some of the dust evolution could have become unbound, but the remainder survives as a compact object in later epochs (and when the tidal radius is outside the size of the source).

2.5.3 Comparison to Observed Merged Binary Systems

G1 shares some observed characteristics with known merged binaries. Our inferred dust temperature of 426-568 K is within the ranges reported for other observed binary mergers, including V1309 Sco (Nicholls et al., 2013) and BLG-360 (Tylenda et al., 2013). Also, the large size and luminosity inferred for G1 are similar to BLG-360. We suggest that G1 and G2, if they are indeed binary mergers, crossed their individual Roche limits sometime between 1 $\times$ 10^4 - 1 $\times$ 10^6 years after the last star formation episode (Stephan et al., 2016). The high eccentricity of G1 and G2 in their respective orbits around Sgr A* is what we would expect from binary systems that have been affected by the Kozai mechanism (Kozai, 1962; Lidov, 1962). That is, we do not assume that these mergers stem from random stellar collisions, but rather that the binaries merge as a result of secular interactions similar to what is described by Prodan et al. (2015). The end result of the eccentric Kozai mechanism yielding a merger product has been discussed in detail in the literature (see the review by Naoz 2016); binary systems are most likely to merge on highly eccentric orbits (Naoz & Fabrycky, 2014; Stephan et al., 2016).

Merged binary systems undergo many physical changes as the merger occurs. For example, there is usually an optical outburst immediately following the physical merging of the stars, along with an evolution of spectral type (e.g., Tylenda et al. 2011, Nicholls et al. 2013). The very few examples that have been published thus far have been inferred to be merged binaries because of optical periodic variability from the binary system before the outburst, and the absence of any periodicity from the system following the outburst (e.g., Tylenda et al. 2011).

The high infrared flux density (2.7 mJy at L') shortly after periapse passage (2005) is consistent with the high fluxes from other binary merger products after the merger has taken place. As the majority of stars in the field and in dense stellar clusters like the nuclear star cluster exist as multiple-component systems (e.g., Prodan et al. 2015; Sana & Evans 2011; Duchêne & Kraus 2013), it is not unreasonable that many of these could merge in the Galactic Center and form extended envelopes of gas and dust.

While the binary merger hypothesis provides many similarities to the observed characteristics of G1, several things remain unclear. The timescale over which such mergers occur is not yet known (but is under study by Stephan et al. 2016); the length of the dusty phase depends on the mass of the progenitors and the relaxation timescale. For instance, V1309 Sco was originally discovered in September 2008 as a "red nova" (Nakano et al., 2008; Rudy et al., 2008a,b; Tylenda et al., 2011) that had an evolving spectral type from F to M. Nicholls et al. (2013) showed that V1309 Sco was undetected in the near-infrared regime prior to its outburst; $\sim$23 months afterward, there was a clear near- and mid-infrared excess. They further model the infrared excess as a dust envelope surrounding V1309 Sco that formed after the merging. Two years after merging, a near-infrared excess was still present (Nicholls et al., 2013). This implies that the duration of the dusty phase was at least 15 years so that our observation window is shorter than the duration of the dust phase. However, if G1 and G2 are more massive sources, winds and radiation stemming from the star could affect the dust envelope lifetime. Several other hypotheses exist that could describe the observables of G1, such as disrupted, edge-on, protoplanetary disks around young, low-mass stars (Murray-Clay & Loeb, 2012), disrupted disks around older stars (Miralda-Escudé, 2012), or some other tidal disruption phenomenon involving a stellar object.

2.6 Conclusions

G1 has several observable properties similar to those of the mysterious G2 object–it is a cold source in the Galactic Center that has hydrogen recombination emission (at Br-γ) and has recently passed very close to Sgr A*. Our orbital fits indicate that G1 and G2 lie on similar orbital planes, but have different arguments of periapse, indicating that these objects are not part of the same gas streamer. In contrast to G2, G1 was originally well-resolved at L' (3.8 μm). This additional information strongly supports the idea that there is a central, stellar object embedded in a gas- and dust-filled envelope.

We hypothesize that G1 may be a binary merger product due to the similarities to observed merger systems (see Section 5.2): notably, it has a large inferred size, and high infrared luminosity. This would be a natural explanation for many unsolved questions regarding other populations in the Galactic Center, including the young stars in the S-star cluster, which may have resulted from the mergers of binaries interacting with Sgr A*, followed by relaxation back to the main sequence. G1 and G2 are also not the only objects with these observed properties in the Galactic Center, as at least 4 others exist close in proximity to Sgr A* (Sitarski et al., 2014). Further studies of these additional sources will indicate whether all these sources have common characteristics such as Br-γ emission, and whether they share a common origin or a common production mechanism.

2.7 Acknowledgements

Support for this work was provided by NSF grants AST-0909218 and AST-1412615, the Levine-Leichtman Family Foundation, the Preston Family Graduate Fellowship (held by B. N. S. and A. B.), and the UCLA Graduate Division Dissertation Year Fellowship (held by B. N. S.). The W. M. Keck Observatory is operated as a scientific partnership among the California Institute of Technology, the University of California, and the National Aeronautics and Space Administration. The authors wish to recognize that the summit of Mauna Kea has always held a very significant cultural role for the indigenous Hawaiian community. We are most fortunate to have the opportunity to observe from this mountain. The Observatory was made possible by the generous financial support of the W. M. Keck Foundation. B. N. S. also thanks James Larkin for his engaging discussions about the nature of G1 and G2, Alexander Stephan for his comments, and Ann-Marie Madigan for her thoughts on G1. We thank the anonymous referee for providing invaluable comments.

2.8 K'-derived distortion solution on L' data

As stated in section 2, we resample all data (K', L', and Ms) data with the geometric optical distortion solution from Yelda et al. (2010). This distortion solution was derived with K' data only, so we tested whether this distortion solution was appropriate to apply to the L' and Ms

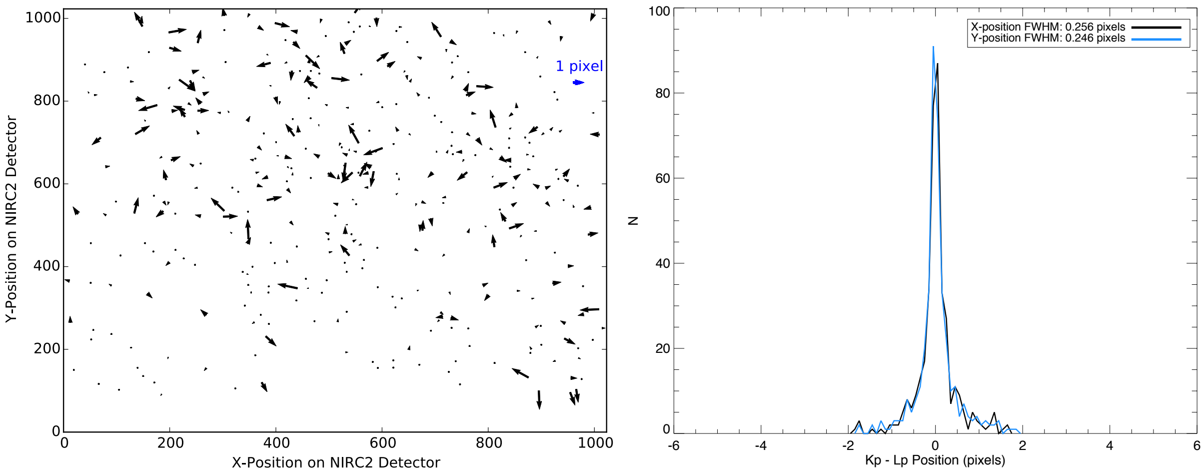

Figure 2.15 *Left*: Difference between the K' and L'-transformed positions across the field of view of NIRC2. The arrows originate at the K' position and end at the position of the L'-transformed-to-K' coordinate system points. There is no systematic position or rotation of the arrows, so using the K' data derived distortion solution is completely adequate. *Right*: Histogram of the difference between the K' and L'-transformed positions. The FWHMs of the distributions are less than the astrometric errors of the data.

data sets. We therefore took one of our epochs of data (we chose 2005.580) and transformed the L' positions as detected by *StarFinder* (see Section 3.1.1) into the K' coordinate system. We allowed for first-order translation, rotation, and pixel-scale adjustments between the two frames that were independent in x and y. The results from this alignment are shown in the left panel of Figure 2.15, where each arrow represents the difference in position for stars identified both at K' and L'. As there is no noticeable rotation or structure indicated by arrows, we conclude that applying the distortion correction for L' data is therefore adequate. The right panel of Figure 2.15 shows a histogram of the difference between the K' and L'-transformed coordinates in both x and y. The FWHM of these histograms are less than the positional errors as found in Table 2.2.

Table 2.6. Jackknife Parameters

Orbital Parameter	Jackknife Parameters
X-Position of Sgr A* (x_0, mas)	2.2±0.3
Y-Position of Sgr A* (y_0, mas)	-4.3±0.3
ΔRA Velocity of Sgr A* (V_x, mas/yr)	0.11±0.02
ΔDec Velocity of Sgr A* (V_y, mas/yr)	0.67±0.03
Radial Velocity of Sgr A*(V_z, km/sec)	-19.3±3.7
Distance to Sgr A* (R_0, kpc)	7.85±0.06
Mass of Sgr A* (M, millions of $M_\odot$)	3.92±0.06
G1 Parameters:	
Periapse Passage Distance($a_{\min}$, AU)	292±44
Time of closest approach (T_0, years)	2001.3 ±0.2
Eccentricity (e)	0.993±0.002
Argument of periapse (ω, degrees)	117±4
Inclination (i, degrees)	109±1
Position angle of the ascending node (Ω, degrees)	86±6

2.9 Jackknife-derived estimates of the variance of G1's orbital parameters and the black hole parameters

To determine whether our errors for the orbit of G1 and the black hole parameters capture at least part of the systematic errors due to potential outliers, we used a jackknife resampling technique to determine the variance of each of G1's orbital parameters while simultaneously fitting S0-2, S0-38, and G1. In each of our orbital fits, we dropped one epoch of observations and determined the jackknife variance over all orbital fits. Our recovered jackknife parameters are listed in Table 2.6. The values and associated error bars calculated from this jackknife analysis are consistent with what is reported in Table 2.4.

CHAPTER 3

Infrared Excess Sources in the Galactic Center

3.1 Introduction and Motivation

The physical natures of G1 and G2 have sparked much debate in the astronomical community (see section 1.2 for a short review). In particular, the question of whether these sources could be gas clouds or stars has motivated many physical models, but no one model has clearly been determined. The detection of similar objects can help determine the nature of G1 and G2 and whether they belong to a previously unreported class of objects at the Galactic Center, or if these two objects are unique. If other objects exist that have similar physical characteristics to G1 and G2, constraints could be placed on the physical model of these sources.

Within the central 2 arcseconds of the Galactic Center, there are several other objects that exhibit infrared excesses; that is, they are brighter at L' (3.8 μm) than at K' (2.2 μm). Eckart et al. (2013) describes a population of infrared excess point-like sources within the central 2 arcseconds of Sgr A*. Their interpretation is that the infrared excess of most of these point-like sources can be described by a mixture of photospheric light from a central star surrounded by a shell of dust of temperature less than 1000 K.

In this chapter, we further wish to constrain the nature of these infrared excess sources to see whether they have other observational characteristics similar to G1 and G2. G1 and G2 both exhibit Br-γ emission that has been thought to arise from an externally ionized gaseous envelope surrounding the central dust shell and stellar source (Witzel et al., 2014; Valencia-S. et al., 2015; Sitarski et al., 2016). A detection of Br-γ emission might constrain whether or not all the infrared excess sources are similar in nature, or whether the observational characteristics of G1 and G2 could be accounted for by several different types of physical manifestations. G1 and G2 both appear to be compact at L' (for G1, a few years after periapse passage), implying that their dust shells are within 10s of AU of their central host star; their blackbody radii are large though, far larger than any main-sequence star. Witzel et al. (2014) explored a physical description for this and posited that G2 might be a binary merger system; Sitarski et al. (2016) present evidence that G1 might also be a binary merger (see arguments within those two papers). G1 and G2 also both lie on similar orbital planes but have different trajectories within that orbital plane.

Here we gather observational characteristics of infrared excess sources to determine whether they exhibit similar features as G1 and G2: that is, we determine whether they: (1) have Br-γ emission features; (2) are resolved sources in Br-γ or L' well beyond or before their possible periapse passage times; (3) move in similar orbital planes or in similar directions; (4) have a similar temperature distribution as G1 and G2; and (5) have L' luminosities that evolve as functions of time. We also determine the radial distribution of the sources (whether they are preferentially clumped to one area near Sgr A*), and whether there is a positional dependence on dust temperature based on the source's proximity to Sgr A* or IRS 13.

This chapter is organized as follows: section 2 describes the data sets used in this study; section 3 details our astrometric and photometric calibration as well as our sample selection criteria and our orbital fitting procedure; section 4 presents our results; section 5 discusses our findings in the context of G1 and G2 and speculates on whether these sources are all part of the same class of objects; and section 6 summarizes our conclusions.

3.2 Data Sets

This study utilizes near-infrared, high-angular resolution images and integral field spectroscopy of the Galactic Center region containing G1 that have been obtained as part of the long-term program at W. M. Keck Observatory. In this study, we use all previously published WMKO LGSAO images that have been acquired through the L' ($\lambda_0 = 3.76\ \mu$m) broadband filter over a time baseline between 2004 and 2015. Eleven data sets were obtained over this eleven-year period with the facility near-infrared camera on Keck II, NIRC2 (PI: K. Matthews). Most of these previous data sets have been reported (Hornstein et al., 2007; Phifer et al., 2013; Meyer et al., 2013; Witzel et al., 2014; Sitarski et al., 2016), but we do include a new data set taken in 2015. Observing techniques are described in those papers, and the 2015 data were taken with the techniques described in Witzel et al. (2014) and Sitarski et al. (2016). Table 3.1 details all our L' observations.

All data were run through our standard pipeline to remove camera and background artifacts (sky-subtracted, flat-fielded, bad pixel corrected, and resampled with the geometric optical distortions from Yelda et al. (2010) and Serivce et al. (2016)). To sky-subtract each science exposure after our 2004 observations, we took a series of sky exposures that matched the field rotator mirror position to within ∼2 degrees to subtract off thermal emission from dust on the mirror optics (Stolte et al., 2010; Sitarski et al., 2013, 2016). In 2004, we took sky exposures in a similar way to our K' maps: we matched dither positions in a blank part of the sky near the Galactic Center at the end of our observations. As this does not subtract off all the thermal emission from the dust on the mirror, there is a large overall background in the 2004 L' data.

In addition to L' imaging, we also draw upon three other imaging data sets. The first is a new K' data set obtained in 2015, published here for the first time but taken in an identical way to all previous K' astrometric maps (e.g., Yelda et al. 2014). It consists of 203 frames with an average FWHM of 57.8 mas and an average strehl of 0.38. These data, along with all previous astrometric epochs of K' data, were used to align all astrometric data with L' data (see Section 2.2). We also use a new LGSAO Ms data set along with previously-published NGSAO Ms data (Hornstein et al., 2007). The LGSAO Ms data were taken in the same fashion as our L' data, including obtaining sky exposures matching the science rotator angles every ∼2 degrees to subtract the thermal emission from the optics.

In addition to the Keck NIRC2 data, we also use one epoch of Br-γ narrow-band imaging data from the European Southern Observatory Very Large Telescope (ESO VLT) taken through the facility near-infrared camera and AO system NAOS/CONICA (NACO). These data were originally published in Kunneriath et al. (2012) and were sky-subtracted, bad pixel corrected, flat-fielded, and cross-talk corrected. They were combined using a shift-and-add algorithm, and an uncertainty map for the shift-and-add combined image was extracted by taking the standard deviation between the subsets of the shift-and-add images. Table 3.1 summarizes all imaging data sets used in this study.

We also use multiple OSIRIS data sets, most of which were originally published in Phifer et al. (2013) and Sitarski et al. (2016). These data are mosaicked together from multiple nights of data taken in a given year in order to maximize the depth of the observations. Most of these observations were taken in the Kn3 narrow-band filter ($\lambda_0 = 2.166$ μm) in order to obtain radial velocity information from any Br-γ ($\lambda = 2.1661$ μm) emission line that was present for some of the sources. We also use two epochs of Kn5 data ($\lambda_0 = 2.35$ μm), which captures CO bandheads ($\lambda = 2.29$ μm and 2.32 μm). One epoch of data (2013) was taken in the *Kbb* filter ($\lambda_0 = 2.173$ μm), which simultaneously encompasses both the Br-γ emission line and CO bandheads. Most data utilized in this study uses the 35 mas/pixel plate scale available on OSIRIS. Table 3.2 describes the depth of all of our OSIRIS data.

3.3 Analysis

3.3.1 Imaging Analysis

Our imaging analysis is divided into two parts: (i) astrometric analysis using the PSF fitting tool *StarFinder* and (ii) photometric calculations using the procedure first described in Sitarski et al. (2016) that simultaneously fits for extent and flux of a source. Both measurements are described in detail below.

3.3.1.1 Astrometry

All astrometric extractions were performed with the PSF fitting program *StarFinder* (Diolaiti et al., 2000) in a similar manner to what has been described in detail in other works (e.g., Yelda et al. 2014 and references therein). We run *StarFinder* using a correlation threshold of 0.8 and 0.6 in the main image and three sub-images for each epoch, respectively, to identify

Table 3.1. Summary of Imaging Data

UT Date	Decimal Date	Band (Orig. Pub.)^{b}	Instrument	$t_{int} \times$ coadds	Frames Taken	Frames Used	Array Size	Dithered FOV	PSF FWHM (mas)	Strehl	L'_{lim}^{a} (mag)	δ_x (mas)
2003 Jun 10	2003.440	L' (1)	Keck/NIRC2	0.50 × 40	12	6	10” × 10”	$12\farcs8 \times 10\farcs2$	85	0.41	13.3	1.4
2004 Jul 26	2004.567	L' (1)	Keck/NIRC2	0.25 × 120	11	11	10” × 10”	$10\farcs7 \times 9\farcs8$	80	0.42	14.4	0.4
2005 Jul 16	2005.539	Ms (2)	Keck/NIRC2	0.20 × 600	39	39	6” × 6”	$6\farcs4 \times 6\farcs4$	100	0.71	12.7	0.4
2005 Jul 30	2005.580	L' (1)	Keck/NIRC2	0.50 × 60	62	56	10” × 10”	$10\farcs3 \times 9\farcs5$	81	0.36	14.4	0.3
2005 Jul 30	2005.580	K' (2)	Keck/NIRC2	2.8 × 10	31	31	10” × 10”	$10\farcs4 \times 10\farcs4$	58	0.31	18.9	0.3
2006 May 21	2006.385	L' (2)	Keck/NIRC2	0.50 × 60	19	19	10” × 10”	$11\farcs4 \times 11\farcs3$	82	0.38	14.4	0.4
2009 Jul 22	2009.556	L' (4)	Keck/NIRC2	0.50 × 60	4	4	10” × 10”	$13\farcs1 \times 12\farcs3$	85	0.38	13.2	0.1
2009 Aug 06	2009.597	Br-γ (3)	VLT/NACO	15.0 × 3	X	X	14” × 14”	$35\farcs1 \times 35\farcs1$	X	X	X	X
2012 Jul 20-23	2012.551	L' (4)	Keck/NIRC2	0.50 × 30	1316	1231	$2\farcs64 \times 2\farcs64$^{c}	$2\farcs6 \times 2\farcs8$	92	0.51	15.3	0.2
2013 Aug 13	2013.616	L' (5)	Keck/NIRC2	0.50 × 60	249	245	$2\farcs64 \times 2\farcs64$^{c}	$2\farcs7 \times 2\farcs6$	90	0.54	15.2	0.1
2014 Mar 20	2014.216	L' (6)	Keck/NIRC2	0.50 × 60	21	21	10” × 10”	$10\farcs3 \times 9\farcs3$	91	0.51	14.4	0.4
2014 May 11	2014.359	L' (6)	Keck/NIRC2	0.50 × 60	9	9	10” × 10”	$10\farcs1 \times 9\farcs3$	90	0.53	13.2	0.4
2014 Jul 2	2014.503	L' (6)	Keck/NIRC2	0.50 × 60	20	20	10” × 10”	$10\farcs2 \times 9\farcs3$	91	0.34	14.1	0.4
2014 Aug 4	2014.590	L' (6)	Keck/NIRC2	0.50 × 60	28	28	10” × 10”	$10\farcs2 \times 9\farcs4$	92	0.50	13.7	0.4
2015 Mar 30	2014.246	L' (7)	Keck/NIRC2	0.50 × 60	58	57	10” × 10”	$10\farcs2 \times 9\farcs3$	94	0.31	14.7	0.4
2015 Mar 31	2015.251	Ms (7)	Keck/NIRC2	0.20 × 600	32	32	10” × 10”	$10\farcs6 \times 9\farcs4$	101	0.80	12.9	0.4

[a] This is defined as the 95% quantile of the distribution of magnitudes of detected stars with *StarFinder*.

[b] References: (1) Ghez et al. 2005a; (2) Hornstein et al. 2007; (3) Kunneriath et al. 2012; (4) Phifer et al. 2013; (5) Sitarski et al. 2016; (6) Witzel et al. 2014; (7) This work.

[c] For all L' and Ms data, a PSF support size of 1” × 1” is used instead of our standard 2” × 2” support size in order to avoid edge effects and high noise levels due to background noise. Comparisons on the larger field of view showed that his had no significant effect on the astrometry or photometry of any of the infrared excess sources.

Table 3.2. OSIRIS IFU Observations

UT Date	Decimal Date	Filter	Plate scale (mas/pix)	N$_{frames}$ Observed	N$_{frames}$ Used	FWHM (mas)	Orig Pub.
2006 Jun 18, 30; Jul 1	2006.495	Kn3	35	28	27	74	Ghez et al. (2008)
2008 May 16; Jul 25	2008.487	Kn3	35	22	21	78	Do et al. (2009b), Phifer et al. (2013)
2009 May 5, 6	2009.344	Kn3	35	24	19	79	Phifer et al. (2013)
2010 May 5, 8	2010.349	Kn3	35	17	16	82	Phifer et al. (2013)
2012 Jun 7-11; Jul 21, 22; Aug 13	2012.556	Kn3	35	47	40	80	This Work
2013 May 11-13	2013.366	*Kbb*	35	36	36	70	Boehle et al. (2016)
2013 May 15	2013.371	Kn5	35	9	8	87	This Work[a]
2013 May 15	2013.371	Kn5	35	14	11	88	This Work[b]
2014 May 17-19; May 22-23	2014.382	Kn3	35	58	55	81	This Work
2015 Jul 23	2015.557	Kn5	50	11	10	83	This Work

[a] This field is slightly North of our central pointing (see Figure 3.1).

[b] This field is slightly South of our central pointing.

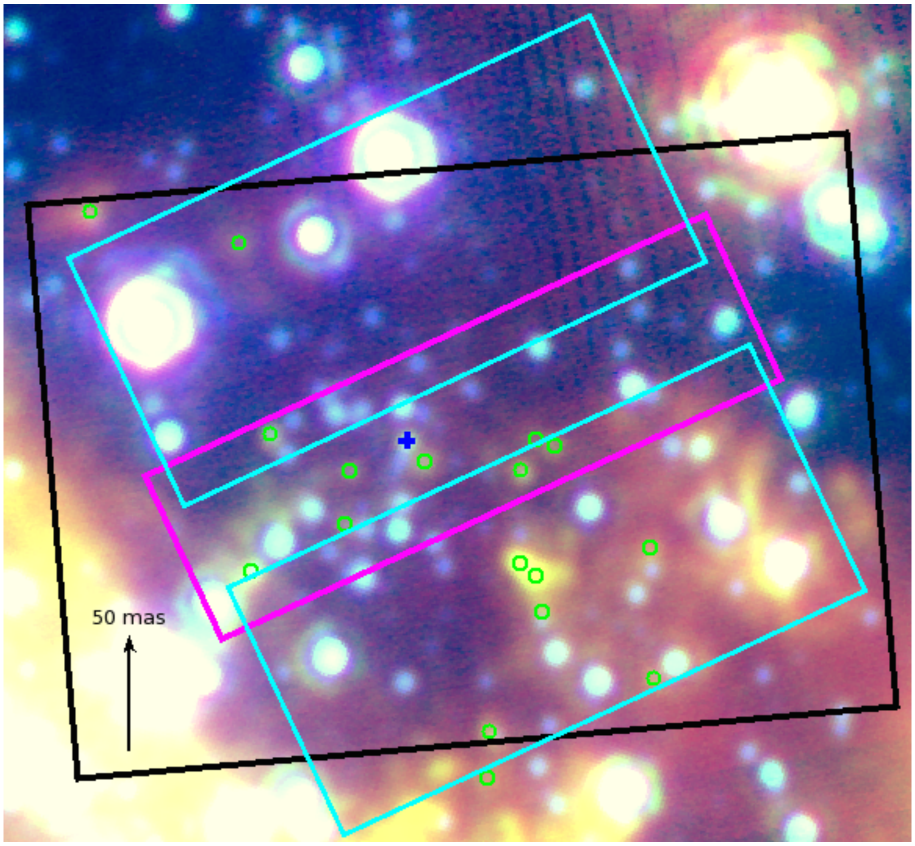

Figure 3.1 Three-color image of the central ~2 arcseconds of the Galactic Center. All data are taken in July 2005. The red color corresponds to Ms data ($\lambda_0 = 4.7\mu$m; $\Delta\lambda = 0.24$ μm); green corresponds to the L' data ($\lambda_0 = 3.8$ μm, $\Delta\lambda = 0.7$ μm); and blue corresponds to K' data ($\lambda_0 = 2.12$ μm; $\Delta\lambda = 0.35$ μm). The blue cross indicates the position of Sgr A*, while the cyan boxes are where our Kn5 data exist. The magenta box outlines the extent of our Kbb data, while the black box shows the extent of our mosaicked Kn3 data. All green circles show the positions of our sample objects. North is up and East is to the left in this image.

candidate sources in each image for each epoch. In all L' and Ms data, we used a smaller PSF support size than what is traditionally used (e.g., Yelda et al. 2014), following Sitarski et al. (2016). Because of the high background levels at L' and Ms, we used a $1\farcs0 \times 1\farcs0$ support size. A comparison with a larger ($2\farcs0 \times 2\farcs0$) PSF on the entire field of view yielded no change in astrometry or astrometric precision.

We initially selected our sample from the 2005 L' and K' data. If the source was not detected in other L' epochs, we used a different approach to obtain the L' astrometry. We searched for a point source within a three-pixel box centered at the point of the highest flux count from a visual identification of the source in the field of view. If the source was not visually identified, we extrapolated what its position might be using its proper motion over detected epochs (as each source was detected in at least three epochs), and then used a modified version of *StarFinder* that searches for additional sources at a lower correlation (Boehle et al., 2016).

Each point source identified in a given epoch was matched across all epochs and transformed to a common coordinate system where Sgr A* is at rest (see Sitarski et al. 2016; Phifer et al. 2013; Yelda et al. 2010, 2014). Specifically, each L' star list was aligned to the nearest K' astrometric epoch that solves for translation, rotation, and a pixel scale that is independent in both x and y. If a point source was identified at L' but not at K', that star's position was added to the K' star list nearest in time. All astrometric K' star lists are then aligned as described in other works (e.g., Ghez et al. 2008; Yelda et al. 2014). These utilize measurements of the infrared astrometric secondary standards taken through 2012 that were used in Boehle et al. (2016) and Sitarski et al. (2016). For our K' data, we ran *StarFinder* as described in Yelda et al. (2014).

3.3.1.2 Photometry

The magnitudes of all point sources identified by *StarFinder* through the K' filter were calculated using our standard *StarFinder* procedure. We used a new set of calibrators identified by Gautam et al. (2016): S1-23, S2-22, S1-25, S0-14, S1-1, S1-13, S1-17, S2-17, S2-21, S2-22, S3-2, S3-6, S3-22, S3-134. These calibrators minimize the photometric zero point compared to our old set of calibrators (IRS 16C, IRS 16NW, IRS 16CC), which are often close to saturation.

Since some of the members of our sample look extended, we adopt the procedure described in Sitarski et al. (2016) to find our photometry: we use an intrinsically extended elliptical Gaussian source convolved with the empirical PSF model as extracted from *StarFinder* from a list of previously-identified PSF stars; this typically recovers the photometry and extent to within 20% down to $L' = 16$ mag (Sitarski et al., 2016). We subtracted the *StarFinder*-generated backgrounds along with neighboring point sources from the original image. This was applied to each of our identified infrared excess sources in all epochs. As in Sitarski et al. (2016), we allowed for the FWHM to range between 0.3 and 10.0 pixels; if the intrinsic size fell below 0.3 pixels in an epoch, then a PSF without a Gaussian was used in lieu of the convolved version.

Following Sitarski et al. (2016), we used S0-2, S0-12, S1-20, and S1-1 to photometrically calibrate our L' and Ms data. The magnitudes of these sources were obtained from Schödel et al. (2010), and have an overall zero-point error of 0.15 magnitudes (R. Schödel, private communication). These four sources are in all fields of view for our L' and Ms epochs including our subarrayed epochs, and are of comparable brightness to G1 and G2. Our usual calibrators (IRS 16C, IRS 16CC, and IRS 16NW) are typically saturated in our L' and Ms data, and are therefore inadequate to use. As in Schödel et al. (2011), we use the same calibrators and same L' magnitudes to photometrically calibrate our Ms data since the L' - Ms magnitudes of the calibrators are close to 0. The L' and Ms magnitudes were dereddened using the extinction prescriptions and A_K map presented in Schödel et al. (2010) and Schödel et al. (2011).

If no K' counterpart was detected for any of the infrared excess sources, star-planting simulations were performed as outlined in Sitarski et al. (2016): the L' position of the source in the 2005 image was translated to the 2005 K' coordinate system as described above, and point sources were planted at that position. Using a modified version of *StarFinder* (Phifer et al., 2013; Boehle et al., 2016; Sitarski et al., 2016), we identified the limiting magnitude at that position. There are some confused sources (i.e., G3 and S0-60), but the fluxes of the confusing sources were subtracted out and the association of the K' and L' counterparts were assessed by comparing their proper motions.

Our Br-γ narrow-band image was flux-calibrated using *Ks* fluxes for IRS 16C, IRS 16NW, and IRS 33N from Schödel et al. (2010) (9.93, 10.14, and 11.20, respectively). As we do not have Br-γ zero points, we used reddened Kurucz atmosphere models to get offsets between *Ks* and Br-γ magnitudes for the NACO filters. For all spectral types (O5V - M0III), the difference was at most 0.05 magnitudes, which is far less than our photometric error. Therefore, we believe that this flux calibration should be accurate to within ~5%. This photometric calibration was performed by R. Schödel for this project and other projects.

3.3.2 Sample Selection

Our sample of infrared excess sources was defined in a manner similar to Stolte et al. (2010), but with more of a focus on L' photometry than K' photometry. Following Figure 7 in Stolte et al. (2010), we generated a dereddened L' vs. K' - L' color-magnitude diagram (following the dereddening prescriptions described in our Photometry section), where the main sequence runs along a constant color (here, K' - $L' \sim 0$). We added 0.7 magnitudes to this as in Stolte et al. (2010) and defined anything red-ward of K' - $L' = 0.7$ to be a member of our sample. Next, we cross-matched our 2005 L' catalog to our 2004 and 2006 L' catalogs (as they are near in time and of good quality) to make sure there were at least two epochs of measurement for each source to rule out spurious detections by *StarFinder* and so that we could make at least a proper motion measurement for all members of our sample. This left us with 17 remaining sources.

To confirm these infrared excess sources, we also plotted a color-color diagram using our L' - *Ms* and K' - L' colors. The main sequence in this plot is centered around (0, 0), while our infrared excess sources are to the top right. Both this plot and our color-magnitude diagram are shown in Figure 3.2.

Our naming scheme for the remainder of this thesis is as follows: all sources start with

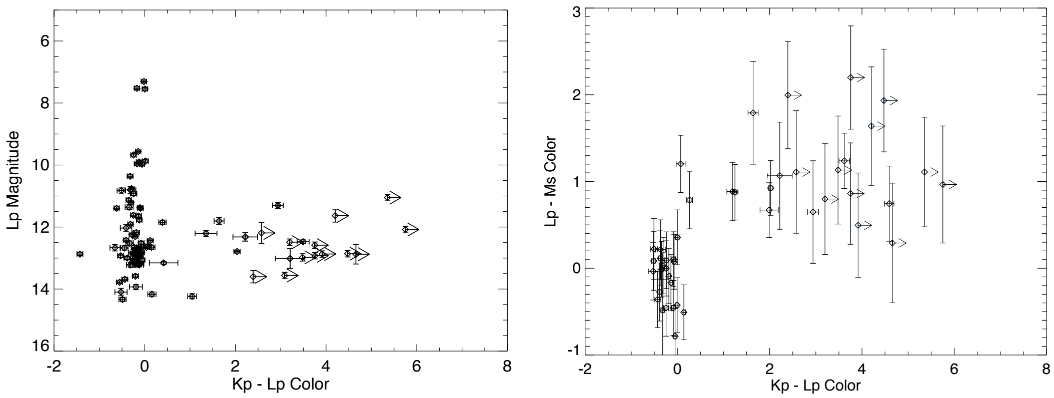

Figure 3.2 *Left*: Color-magnitude diagram plotting our K' and L' magnitudes and colors. The K' limits (here plotted as arrows) were determined using a star-planting technique. Our infrared excess sample consists of stars with a K' - L' color greater than 0.7 magnitudes. *Right*: Color-color diagram plotting our $K' - L'$ and L' - Ms colors. The main sequence is concentrated at (0, 0), while the infrared excess sources we include in our sample are on the top right.

"G" (as we speculate later whether all these sources are similar to G1 and G2), and they are ordered based on their projected distance from Sgr A* in 2005.580. The one exception is G3, whose name was adopted prior to this in-depth look of many infrared excess sources.

3.3.3 Spectroscopic Analysis

Since a majority of our selected sources lie within the field of view of our mosaicked OSIRIS Kn3 data cubes, we sought to: (1) measure the radial velocities of the sources if they had spectral features that allowed for this endeavor, and (2) determine the luminosity of the lines that were present. Since G1 and G2 both have Br-γ emission lines and we believe that G2-like objects would show emission in this line as a result of ionization of a gaseous envelope around the source by the ambient radiation field; we looked for Br-γ features from each of the sources. This was initially done on our 2006 OSIRIS mosaicked cube because it is not only closest in time to our 2005 sample selection observations, but it constitutes some of our deepest Kn3 data. If a source was not identified in that epoch, we looked at the 2009 Br-γ narrow-band map to see whether or not it should be detected. If the source was

Table 3.3. Infrared Excess Sources

Name	ΔRA (2005, arcsec)	ΔDec (2005, arcsec)	Projected Distance (2005, arcsec)	K' (mag)	L' (mag)	Ms (mag)
G1	-0.07±0.008	-0.07±0.006	0.11±0.003	>18.8	13.6±0.1	12.7±0.3
G2	0.25±0.002	-0.12±0.002	0.28±0.002	>20.0	14.0±0.3	13.6±0.4
G3	-0.48±0.001	-0.13±0.002	0.50±0.002	>18.2	13.7±0.1	12.7±0.4
G6	0.58±0.005	0.03±0.006	0.58±0.008	17.0±0.2	13.5±0.1	12.2±0.4
G7	-0.62±0.003	-0.12±0.001	0.62±0.003	>19.0	14.2±0.1	12.9±0.4
G4	0.26±0.001	-0.35±0.002	0.44±0.002	>18.5	14.8±0.2	12.6±0.4
G5	-0.54±0.003	0.00±0.002	0.54±0.004	>19.3	14.0±0.1	13.3±0.3
G11	-1.02±0.002	-0.46±0.001	1.12±0.002	>19.1	14.7±0.1	13.4±0.4
Comet	-0.48±0.003	-0.52±0.002	0.70±0.004	16.8±0.1	12.5±0.1	11.7±0.3
G9	-0.57±0.007	-0.73±0.003	0.92±0.003	>19.3	14.2±0.1	11.8±0.4
G13	-1.04±0.003	-1.01±0.007	1.45±0.008	>20.0	14.1±0.1	12.0±0.4
G12	-0.35±0.003	-1.24±0.008	1.28±0.008	>20.5	13.3±0.1	12.2±0.3
G14	-0.33±0.002	-1.43±0.001	1.47±0.004	18.7±0.1	14.2±0.3	12.6±0.4
G8	0.67±0.004	-0.55±0.009	0.86±0.010	16.0±0.1	13.0±0.1	11.0±0.3
G15	1.34±0.003	0.97±0.003	1.65±0.004	>18.5	12.9±0.2	11.1±0.5
G10	0.71±0.004	0.84±0.009	1.10±0.010	>17.3	13.4±0.3	12.1±0.4

positively identified in the 2009 Br-γ map but not in the 2006 OSIRIS data cube, we looked at the 2012 and 2013 data cubes, our two deepest observations, to try to identify it there.

As of the writing of this thesis, there are some problems with the OSIRIS data reduction pipeline (DRP). Flux mis-assignment along spectral channels (as much as 20% of the flux is leaking into spectral channels ±32 channels away) as well as a spatial ringing pattern leave reduction artifacts (see UCO white paper by T. Do and J. Larkin). A group of OSIRIS users from WMKO, UCLA, UCSD, and UCSC, including the author, are looking into these issues, trying to characterize and fix them. For that reason, some of the deepest data presented here may be compromised and reduction artifacts might be seen in the spectra of the sources in our sample.

The spectra of all our sources were extracted at the location in our OSIRIS data that was found by transforming the nearest L' star list in time to each OSIRIS star list to put our sources in the OSIRIS reference frame with a second-order polynomial transformation. The spectra were extracted using an aperture of 1 pixel (corresponding to 35 mas in all our *Kbb* or Kn3 data), and doing a local sky subtraction (e.g., Do et al. 2013b). The extracted spectrum was calibrated using our standard techniques as outlined in Do et al. (2009a). The peak in the output spectrum was fit with a one-dimensional Gaussian model to derive an observed radial velocity and FWHM. All data were corrected to obtain an LSR velocity using the PyRAF/IRAF package *rvcorrect*.

If the Br-γ line was detected for a given source, then the luminosity was calculated as was done in Phifer et al. (2013) and Sitarski et al. (2016): by comparing the flux density of S0-2 to the flux density of the infrared excess sources. S0-2's dereddened flux density is estimated to be 14.1 ± 0.2 mJy at the Br-γ wavelength (and across the entire K' bandpass) (Ghez et al., 2008), with the extinction law prescribed by Schödel et al. (2010) applied.

3.3.4 Proper Motion Determination

Proper motion fits have been extremely useful in the Galactic Center for determining the dynamics of the young stars near the central potential (e.g., Yelda et al. 2014). Eckart et al.

(2013) reported proper motions of multiple "dusty" sources near the central potential that were computed over a 10-year time baseline with data taken from high-pass filtered and Lucy and linear Weiner-filtered images; astrometric measurements were calculated using Gaussian fits to the source profiles. Proper motions are particularly useful because none of our astrometric data sets favor an acceleration fit (Table 3.4), implying that most of our kinematic information stems from a first-order fit with just an initial position and velocity. For our proper motion analysis, we use the astrometric data points extracted from *StarFinder* through the L' filter.

Source confusion is one of the largest sources of systematic error that is not accounted for in our formal astrometric uncertainties computed from three submaps; our errors are therefore underestimated. To account for source confusion, we fit a second-order polynomial to our astrometric data points and add a single additive value in quadrature to the formal x and y errors until the final reduced chi-squared of the second-order fit (including position, velocity, and acceleration) is equal to 1.0. The resulting additive errors are shown in the table below; they are either roughly comparable or less than the formal uncertainties that we calculate using our three submaps. Additional errors were not added in quadrature if there were less than four astrometric points (as a second-order polynomial could not be fit), or if there was significant extended structure (as in the case of G15 and G10). The additive errors are reported in Table 3.4.

We computed the proper motions for all sources with first-degree polynomials in x and y following the prescription outlined in Yelda et al. (2014):

$$x(t) = x_0 + v_{x,0}(t - t_0) \tag{3.1}$$

$$y(t) = y_0 + v_{y,0}(t - t_0) \tag{3.2}$$

Here, t_0 corresponds to a reference time derived from the mean time of all epochs weighted by the astrometric errors, and v_0 corresponds to the proper motions at the reference time in the x and y directions. Proper motions and references times for all sources are reported in Table 3.4. Uncertainties for all terms were computed from the covariance matrices generated for each linear fit. Our proper motion fits for all our sources are shown in Figure 3.3.

Table 3.4. Proper Motions of IR Excess Sources

Name	$x(t_0)$ (arcsec)	$y(t_0)$ (arcsec)	$v_x(t_0)$ (mas/yr)	$v_y(t_0)$ (mas/yr)	Reference Time (t_0, year)	Identification from Eckart et al. (2013)	Additive Error (arcsec)	Vel vs. Accel Fits[a]	Significant a_z?
G15	1.3422±0.0005	0.9225±0.0004	-0.76±0.22	-3.07±0.21	2011.15	D7	Extended	Vel	No
G10	0.7343±0.0020	0.8380±0.0011	16.78±0.83	5.71±0.49	2007.41	Not IDed	Extended	Vel	No
G5	-0.5433±0.0024	0.0037±0.0017	-9.12±1.26	9.65±1.72	2006.01	Not IDed	0.0011	Vel	No
G7	-0.5678±0.0006	0.0422±0.0015	10.19±0.14	13.39±1.76	2011.25	D3	0.0045	Vel	Yes
G3	-0.4247±0.0015	-0.0082±0.0015	9.84±0.39	20.04±0.42	2011.50	D2	0.0045	Vel	Yes
G6	0.6630±0.0028	0.1060±0.0028	11.94±0.70	11.51±0.79	2012.09	D5	0.0080	Vel	No
G4	0.2652±0.0015	-0.3490±0.0011	29.06±2.20	1.13±1.95	2005.63	Not IDed	<3 Points	Vel	No
G8	0.6595±0.0010	-0.5276±0.0009	-0.88±0.26	3.40±0.23	2011.32	D6	0.0025	Vel	No
G14	-0.4462±0.0027	-1.4032±0.0027	-22.04±0.65	5.10±0.64	2011.09	Not IDed	0.0055	Vel	No
G12	-0.3932±0.0010	-1.2093±0.0010	-8.33±0.24	4.91±0.24	2011.24	F1	0.0029	Vel	No
G13	-1.0429±0.0008	-1.0249±0.0010	-0.17±0.18	-2.87±0.19	2010.63	D8	0.0016	Vel	No
G11	-1.0269±0.0012	-0.4566±0.0006	-4.04±1.56	2.71±0.57	2006.25	Not IDed	<3 Points	Vel	No
G9	-0.5656±0.0007	-0.7356±0.0006	-0.40±1.31	1.53±1.23	2005.90	Not IDed	<3 Points		
Comet						D4	Extended		

[a] An F-Test was performed to determine whether an acceleration or velocity fit is favored based on the chi-square and degrees of freedom for each fit. The null hypothesis that an acceleration fit would work better than a linear fit was rejected if the F-statistic was greater than 0.05.

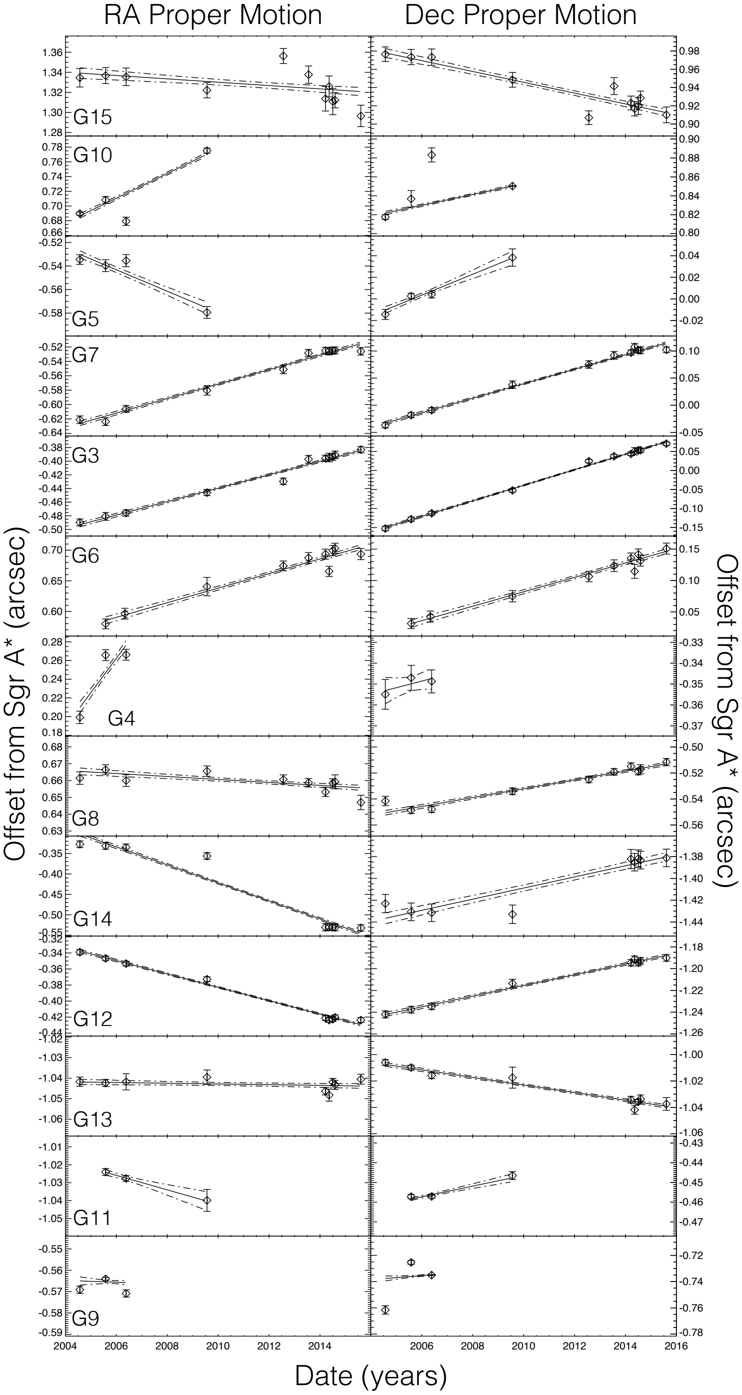

Figure 3.3 Astrometric data of each source with their linear fit described in equations 3.1 and 3.2 overplotted in both RA and Dec. The error bars reported on each of the astrometric points take into account the additive error as described in Section 3.3.4. The dotted lines show the error envelopes for the linear fits.

3.3.5 Orbit Determination

In order to compute orbital fits on any of our infrared excess source sample, they have to have enough kinematic information. An orbital fit consists of six Keplerian orbital parameters (period, epoch of periapse passage, eccentricity, position angle of the ascending node, argument of periapse, and inclination) for each source included in the fit, along with the seven black hole parameters (the two-dimensional position, the three-dimensional velocity, and the mass and distance to Sgr A*). As some of these sources are significantly far away from Sgr A* that they may not have moved very much in the plane of the sky (and therefore may not have significant orbital phase coverage), we select which stars to perform complete Keplerian orbital fits based on: (1) whether they have Br-γ emission so that we can calculate their radial velocities, and (2) if they have significant acceleration along the z direction (a_z) based on a linear fit to their radial velocity measurements using *mpfitexy* (Williams et al., 2010). This is one cutoff that we apply as there is limited kinematic information from the x and y astrometry (see Table 3.4). The values computed for a_z are reported in Table 3.9. To pass the significance test for the second criteria, we set that $a_z/\sigma_{a_z} > 2.0$ to ensure that there would be enough kinematic information for a full orbital fit. We therefore only perform complete Keplerian orbital fits for G3 and G7 in addition to those reported by Sitarski et al. (2016) for G1 and G2 (see Chapter 2 of this thesis).

As in Boehle et al. (2016) and Sitarski et al. (2016), we use a three-star fit for each orbital fit that includes S0-2, S0-38, and an individual infrared excess source that passes the above criteria. We fit for the six Keplerian orbital parameters for each constituent of an orbital fit; S0-2 and S0-38's orbital information drive the fit of the black hole parameters since they have complete orbital phase coverage. We use the same radial velocities and astrometric points for S0-2 and S0-38 as Boehle et al. (2016) and Sitarski et al. (2016) but with additional data to reflect our longer time baseline which are reported in the last section in this chapter. We use uniform, flat priors on all free parameters and we fit only bound Keplerian orbits. Since each orbital fit also re-derives the black hole parameters, we report and analyze them in the last section of this chapter.

Our astrometry for our infrared excess sources at most consist of 11 data points (from 2004 - 2015) and at most 7 radial velocity points from our seven Kn3 or *Kbb* data.

3.4 Results

3.4.1 Proper Motion Comparisons

Proper motions for each of the sources in our sample are shown in Table 3.4. As Eckart et al. (2013) computed proper motions for these sources as well, it is worthwhile to compare the magnitude of the proper motions. Assuming a distance of 8 ± 0.6 kpc (Ghez et al., 2008), it is easy to convert the proper motions listed in Table 3.4 in mas/year to km/sec. Not all of the proper motions of our sources align with the L' or combined proper motions reported in Table A.1 of Eckart et al. (2013). G3 (D2) has the clearest difference in proper motions. This might be due to the fact that in our data, the L'-detected source follows a different trajectory than the K' detected sources that are confused with G3 at a given time (S0-60 from 2005 to 2009; S0-43 after 2014). Our longer time baseline past 2012 elucidates that G3 is not tied to S0-60 or S0-43. The proper motions cited in Table A.1 of Eckart et al. (2013) also vary based on wavelength for G3 (D2), which may point to separate objects identified in their L' and Ks filters.

The only other source with significantly different proper motions compared to Eckart et al. (2013) is G15 (D7). In our data, G15 is clearly extended at both L' and Ms and in fact has a distinct bow-shock like morphology. Figure 1 in Eckart et al. (2013) also shows that G15 (D7) is extended compared to its neighboring sources as well. Because of its extended structure, precise astrometry is quite difficult to do, especially with *StarFinder* (see Sitarski et al. 2016).

The proper motions of the other sources also identified by Eckart et al. (2013) agree within our error bars, but our error bars are at least a factor of two less than Eckart et al. (2013). Two sources have fairly circular movement (G3 and G6) across the plane of the sky; this movement will be further described in section 3.5.3 for G3. Table 3.4 describes the first

Table 3.5. Emission Features Identified

Name	Br-γ $\lambda_0 = 2.1661 \mu$m	[Fe III] $\lambda_0 = 2.1459\ \mu$m	[Fe III] $\lambda_0 = 2.2184\ \mu$m	CO Bandhead 2.29 & 2.32 μm
G4	Yes	No	No	No
G6	No	No	No	No
G12	Yes	Yes	Yes	No
G7	Yes	Yes	Yes	No
G10	No	No	No	No
G13	Yes	Yes	Yes	No
G4	No	No	No	No
G11	Yes	Yes	Yes	No
G5	Yes	No	No	No

proper motion detections of sources not previously identified by other works.

3.4.2 Emission Line Detections, Radial Velocity Measurements, and FWHM Calculations

As a principal goal to this project is to determine if there is a population of G2-like objects at the Galactic Center or if G1 and G2 are indeed unique objects, other G2-like objects should have similar observational qualities to G1 and G2. Both G1 and G2 harbor Br-γ emission (Gillessen et al., 2012; Phifer et al., 2013; Pfuhl et al., 2015; Sitarski et al., 2016). Spectra of our infrared-excess sources were extracted as described in Section 3.3.3, and if they were within the field of view of our Kn3 data, their spectra are plotted below. The identification of any emission lines in our spectra are shown in Table 3.5 below.

Several of the sources also have other emission lines, which are identified as collisionally-excited [Fe III] emission at $\lambda = 2.1459\ \mu$m and $\lambda = 2.2814\ \mu$m (e.g., Bautista & Pradhan 1998). These emission lines are at the same radial velocity as the Br-γ emission lines also seen in these sources. [Fe III] lines were originally identified in the Galactic Center by Eckart et al. (1992) and is thought to trace hot material in the vicinity of the supermassive black hole. Lutz et al. (1993) find that [Fe III] emission might stem from the high-abundance gas

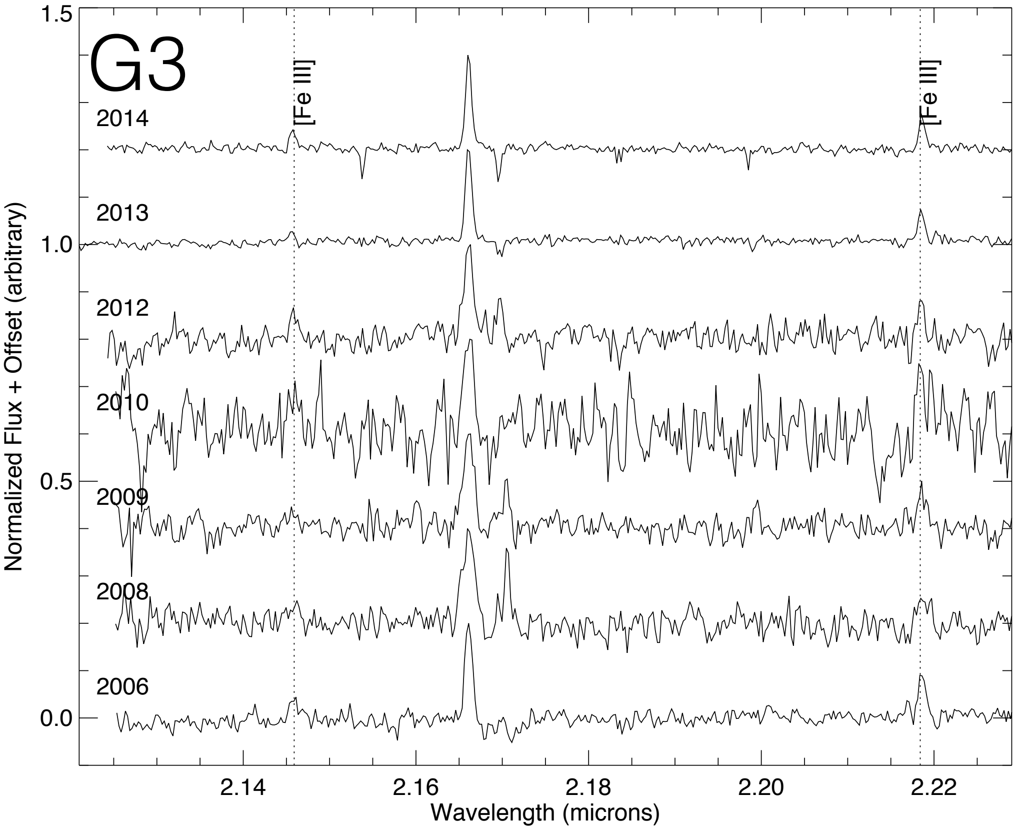

Figure 3.4 Kn3-bandpass range of infrared excess sources within the field of view of our OSIRIS observations that were identified in multiple epochs. The dotted vertical lines indicate the position of OH lines that were often successfully removed. The vertical dashed-dotted lines indicate the rest position of [Fe III] lines.

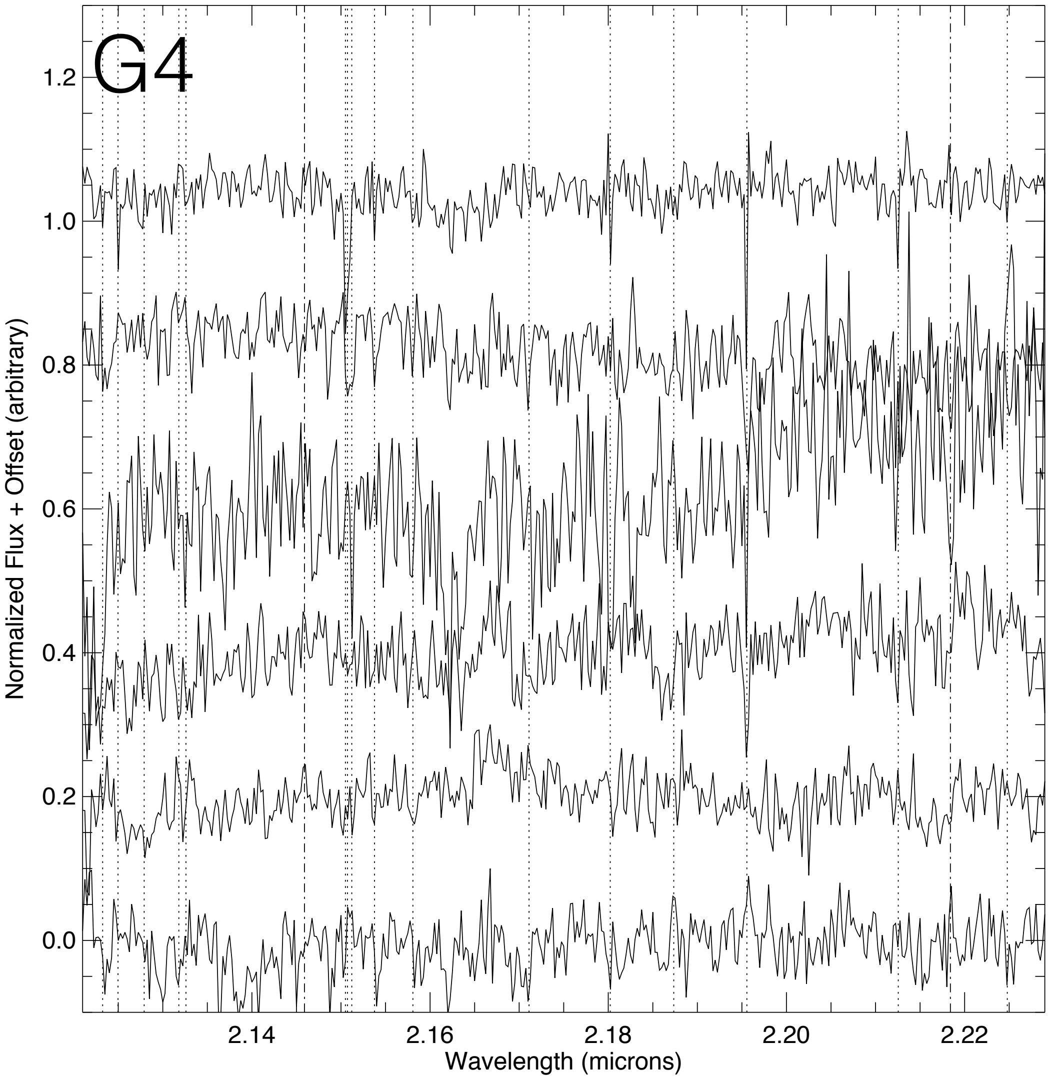

Figure 3.5 Same as figure 3.4, but for G4.

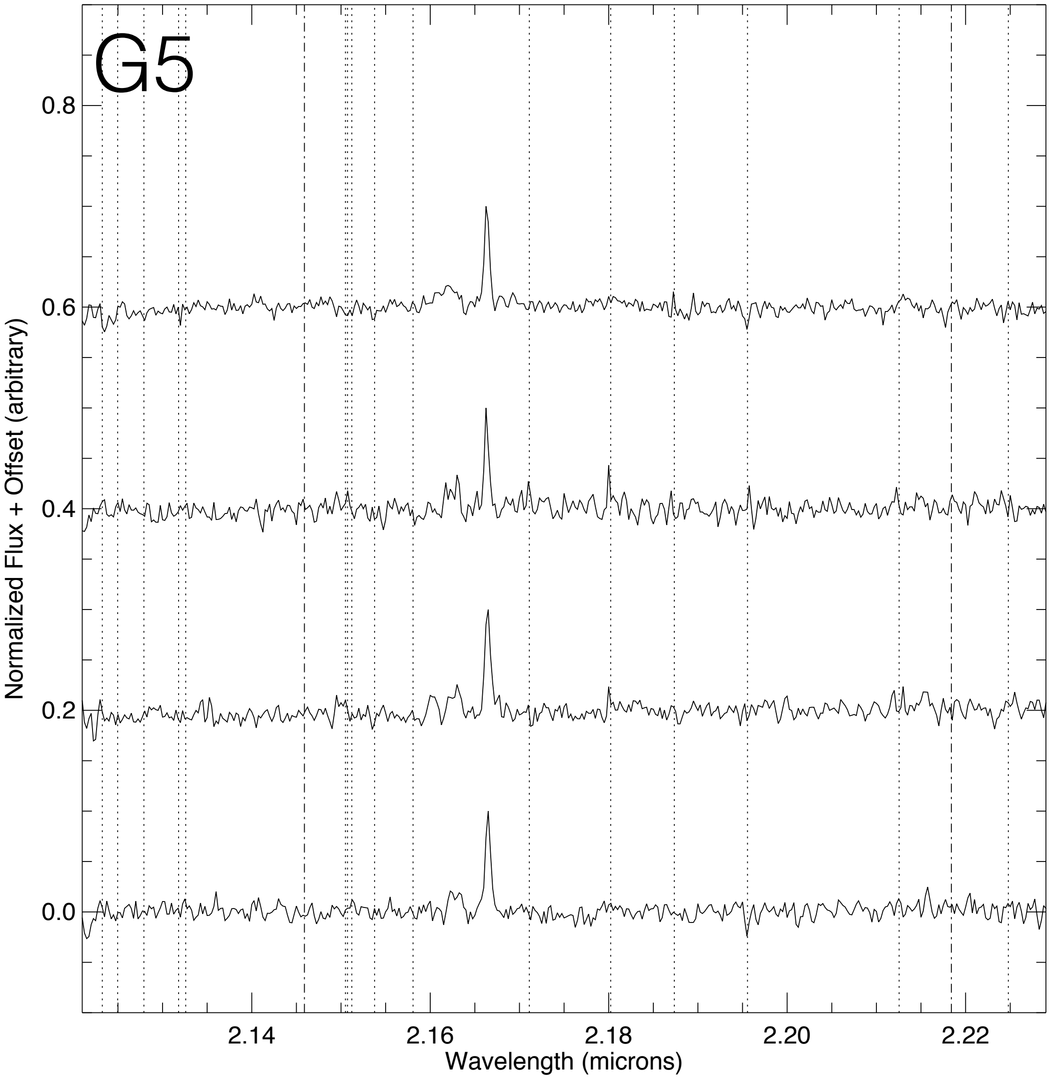

Figure 3.6 Same as figure 3.4, but for G5.

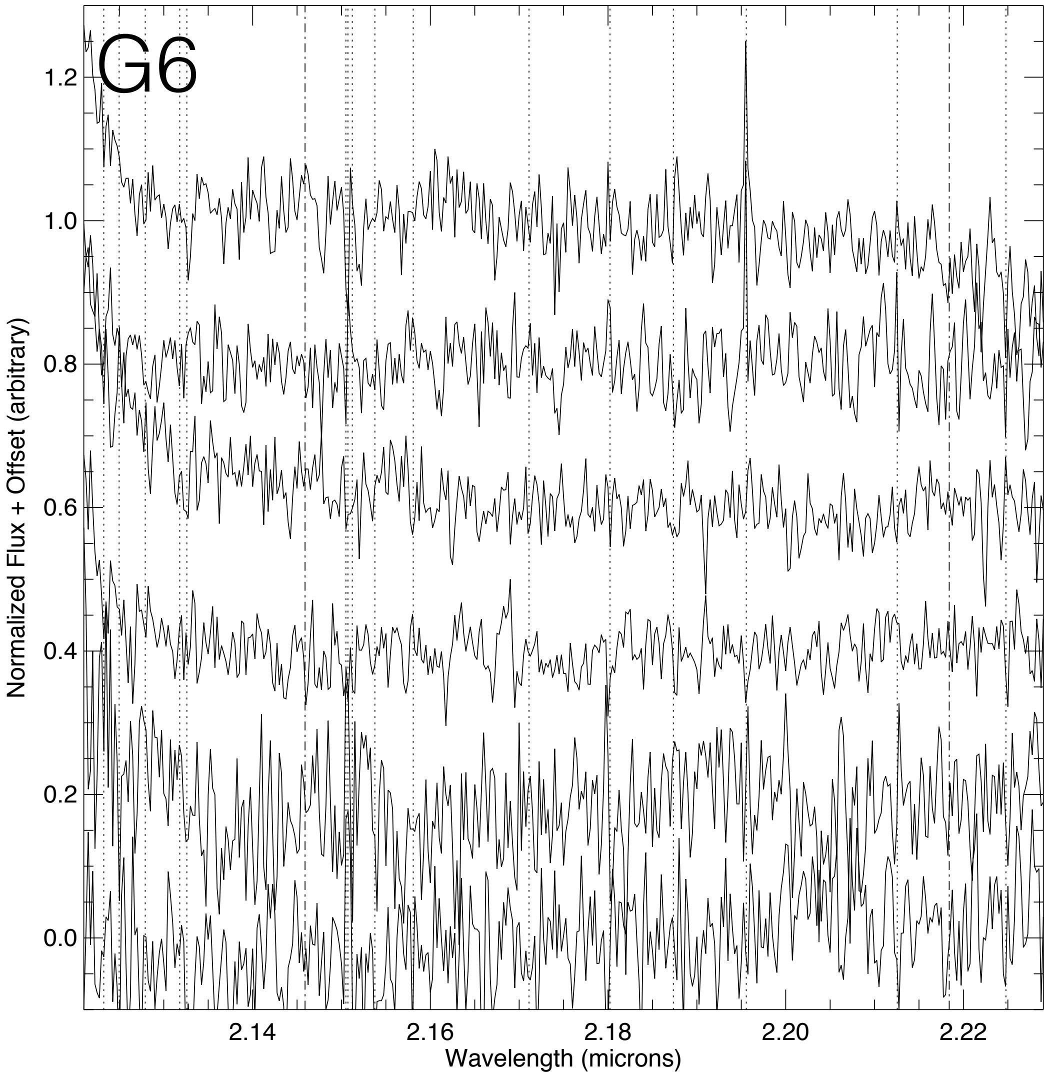

Figure 3.7 Same as figure 3.4, but for G6.

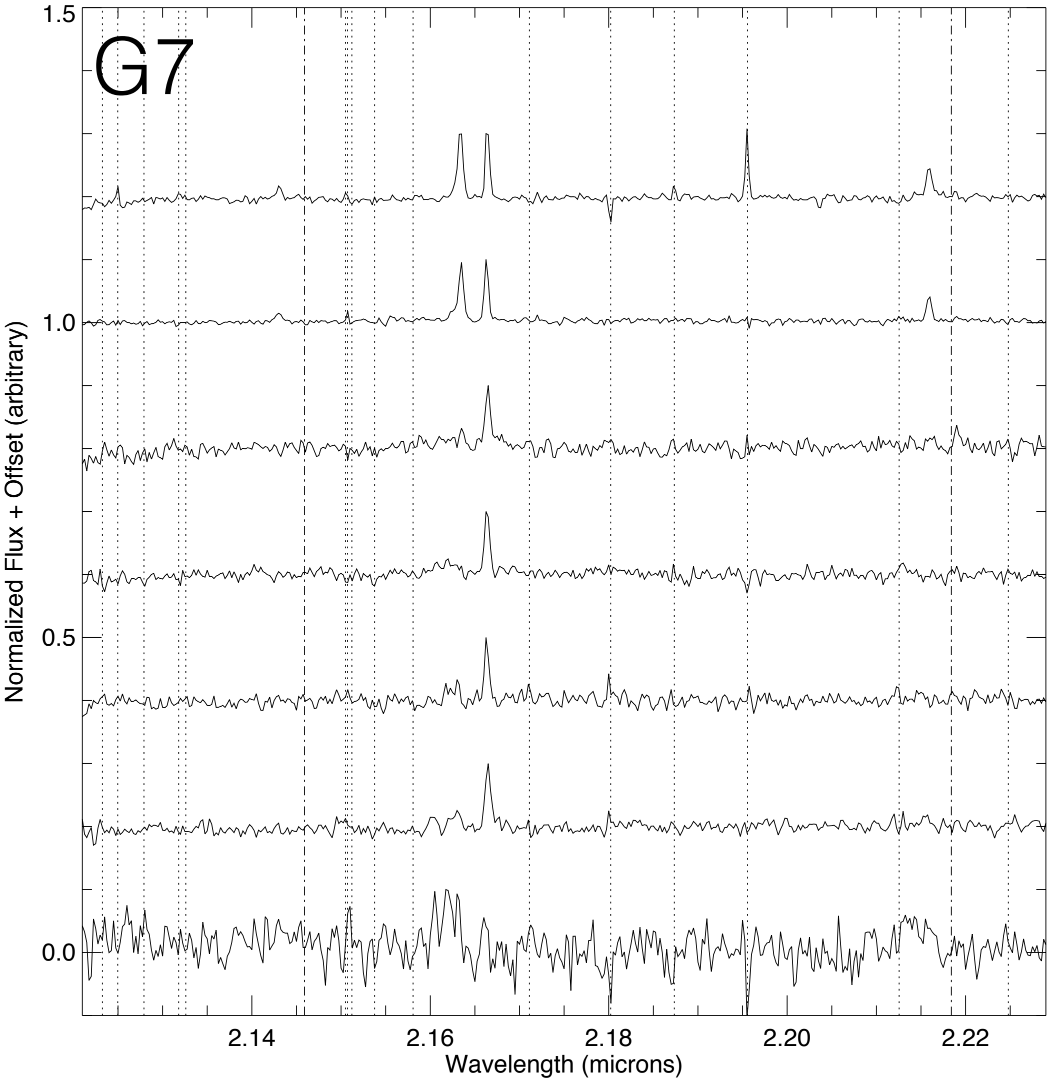

Figure 3.8 Same as figure 3.4, but for G7.

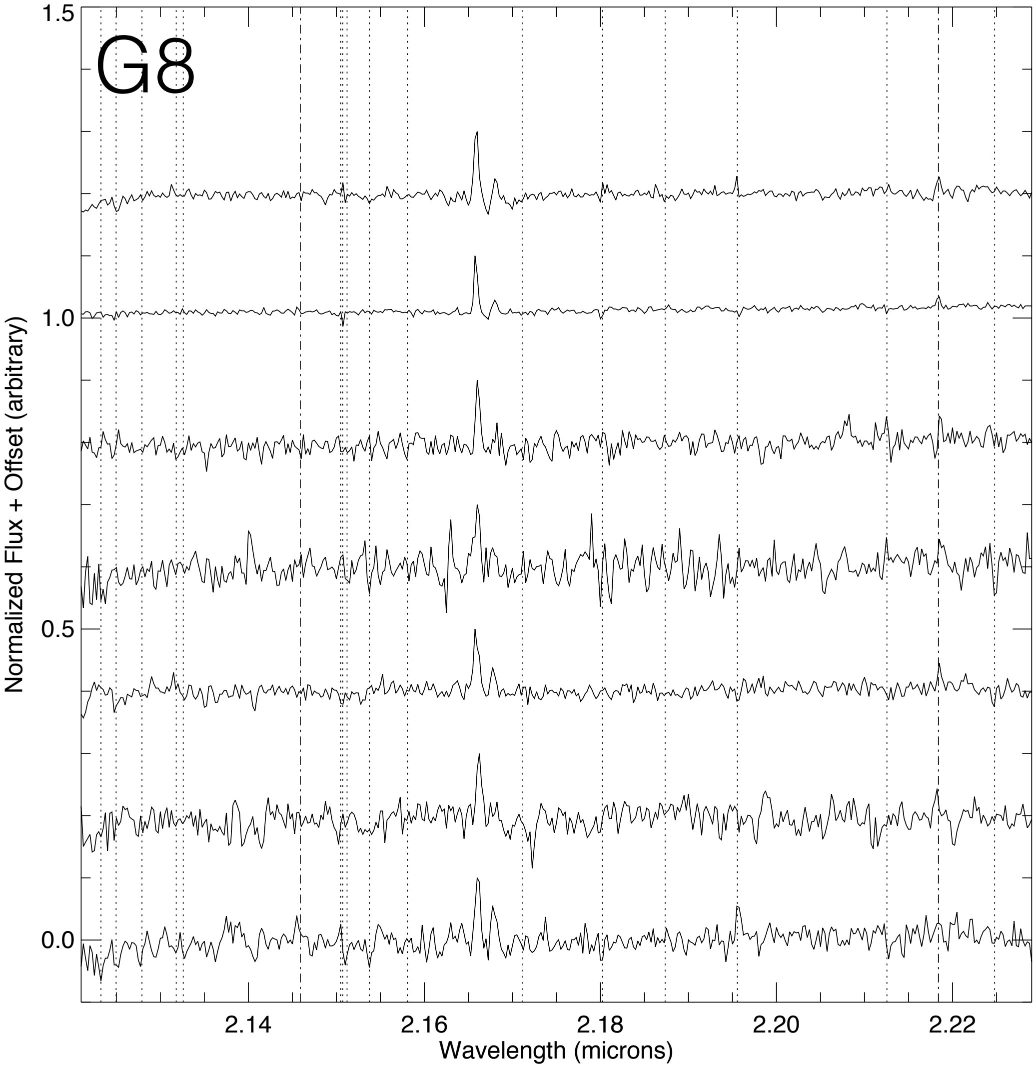

Figure 3.9 Same as figure 3.4, but for G8.

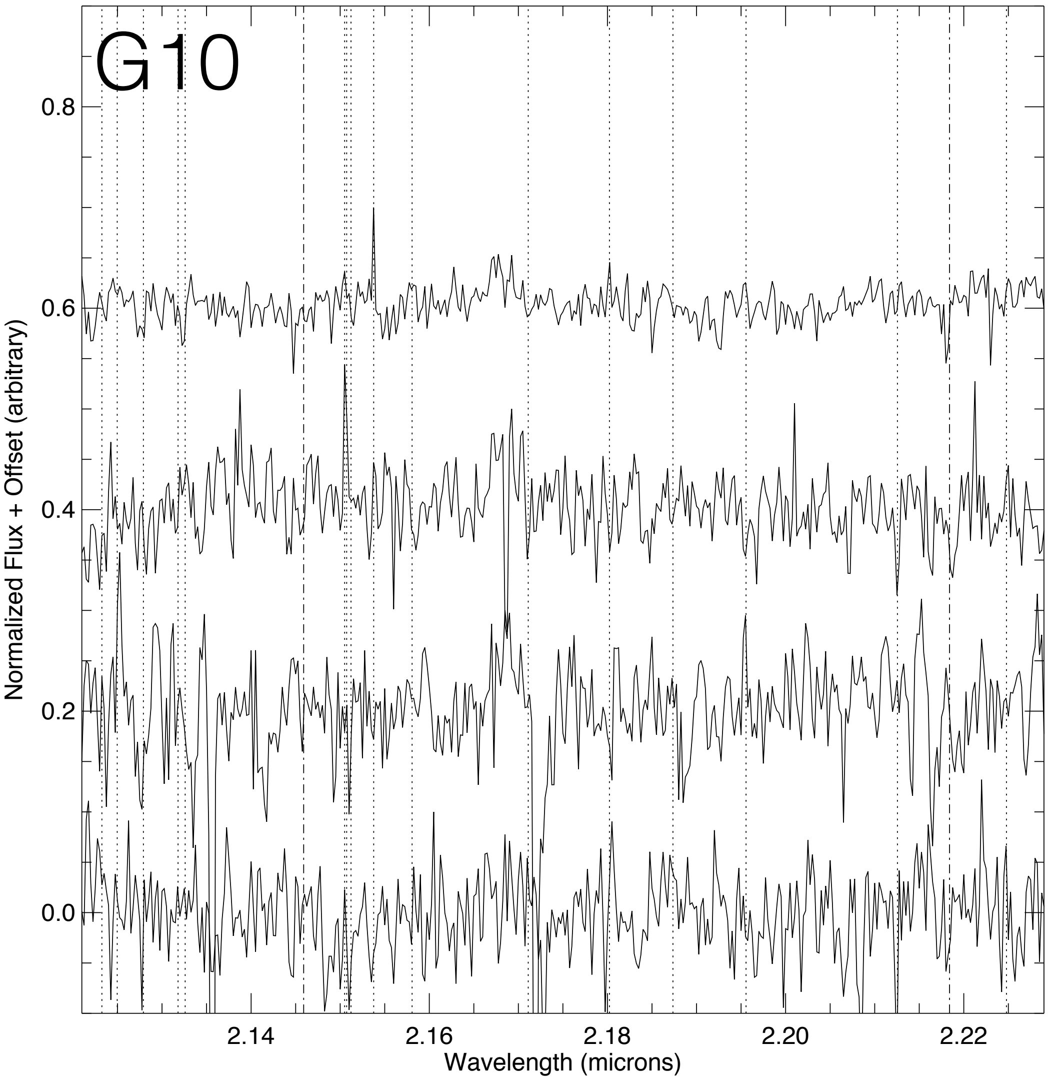

Figure 3.10 Same as figure 3.4, but for G10.

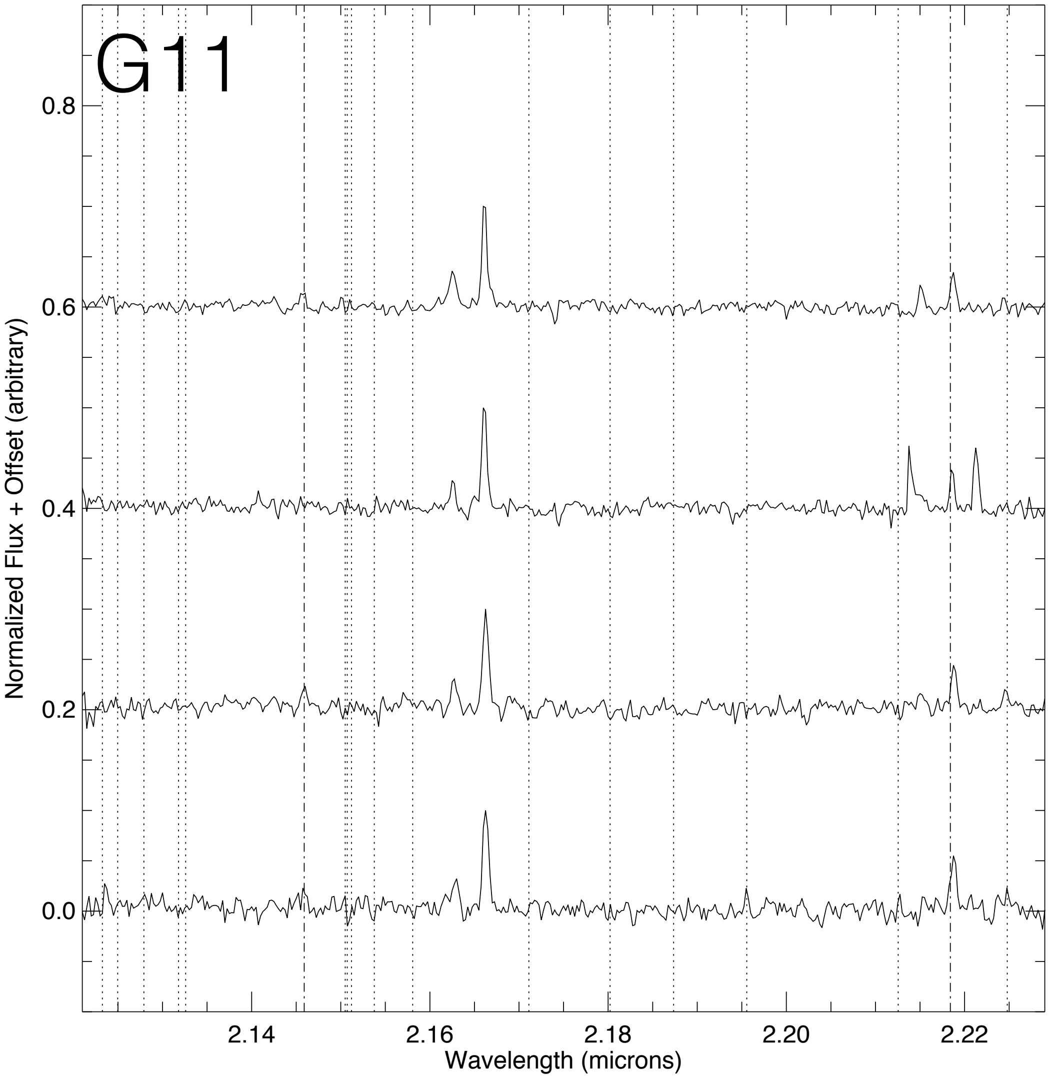

Figure 3.11 Same as figure 3.4, but for G11.

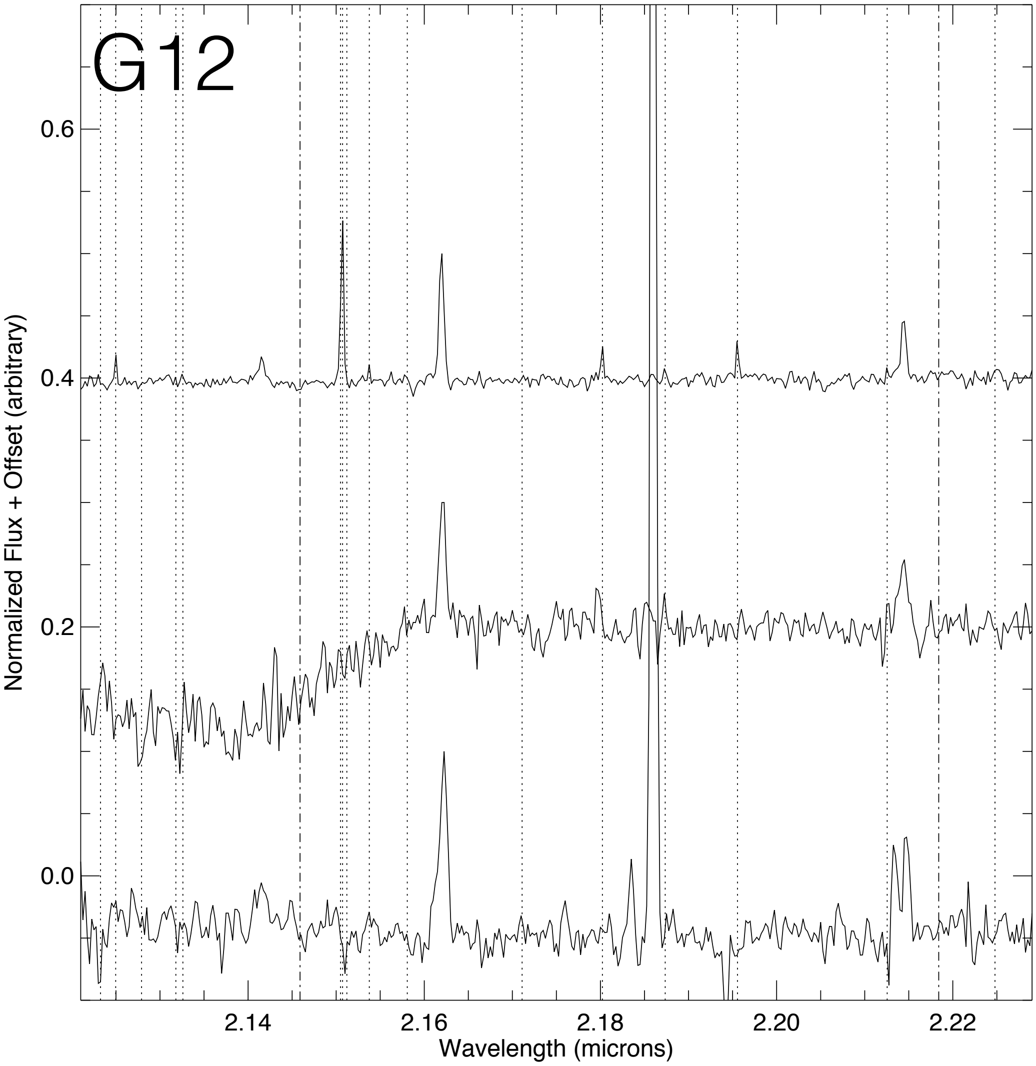

Figure 3.12 Same as figure 3.4, but for G12.

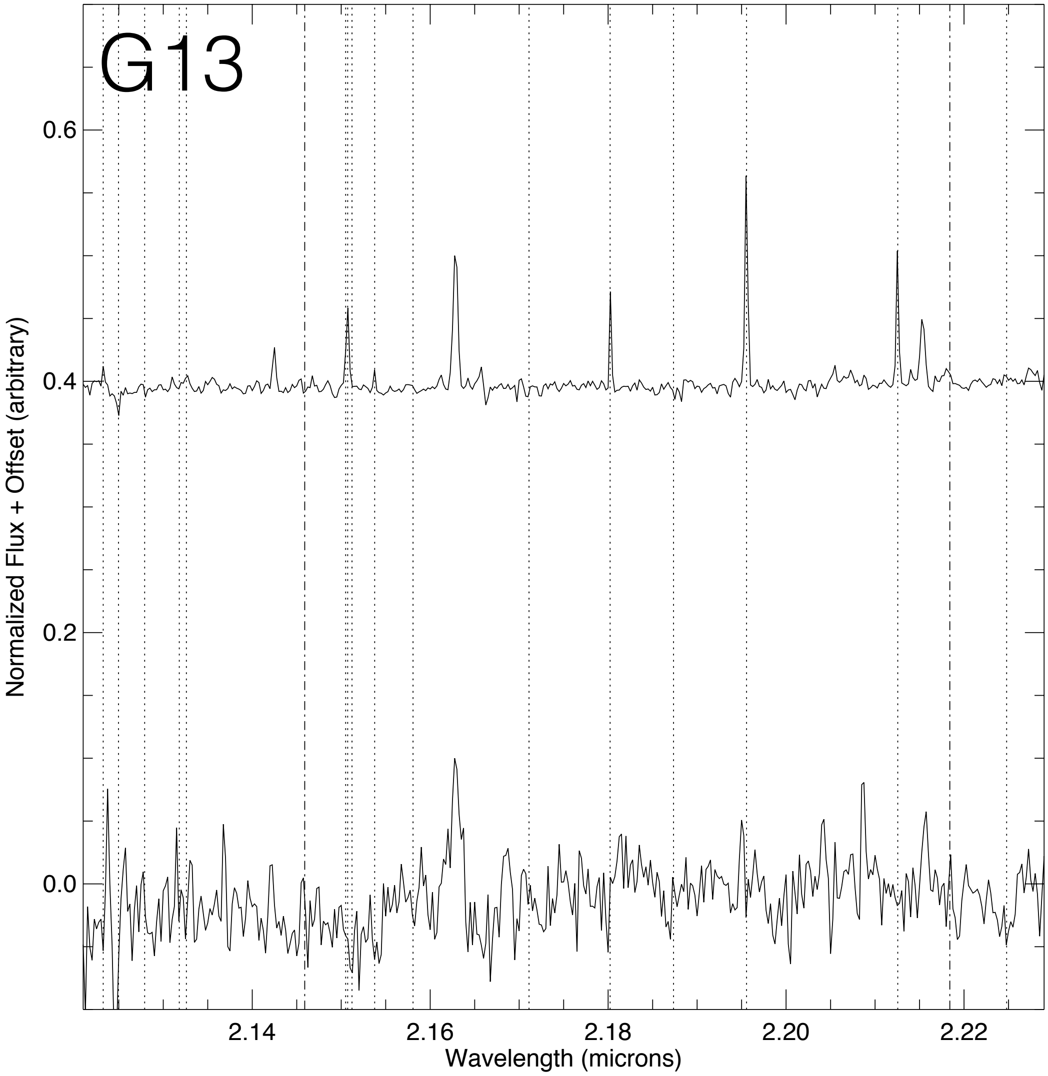

Figure 3.13 Same as figure 3.4, but for G13.

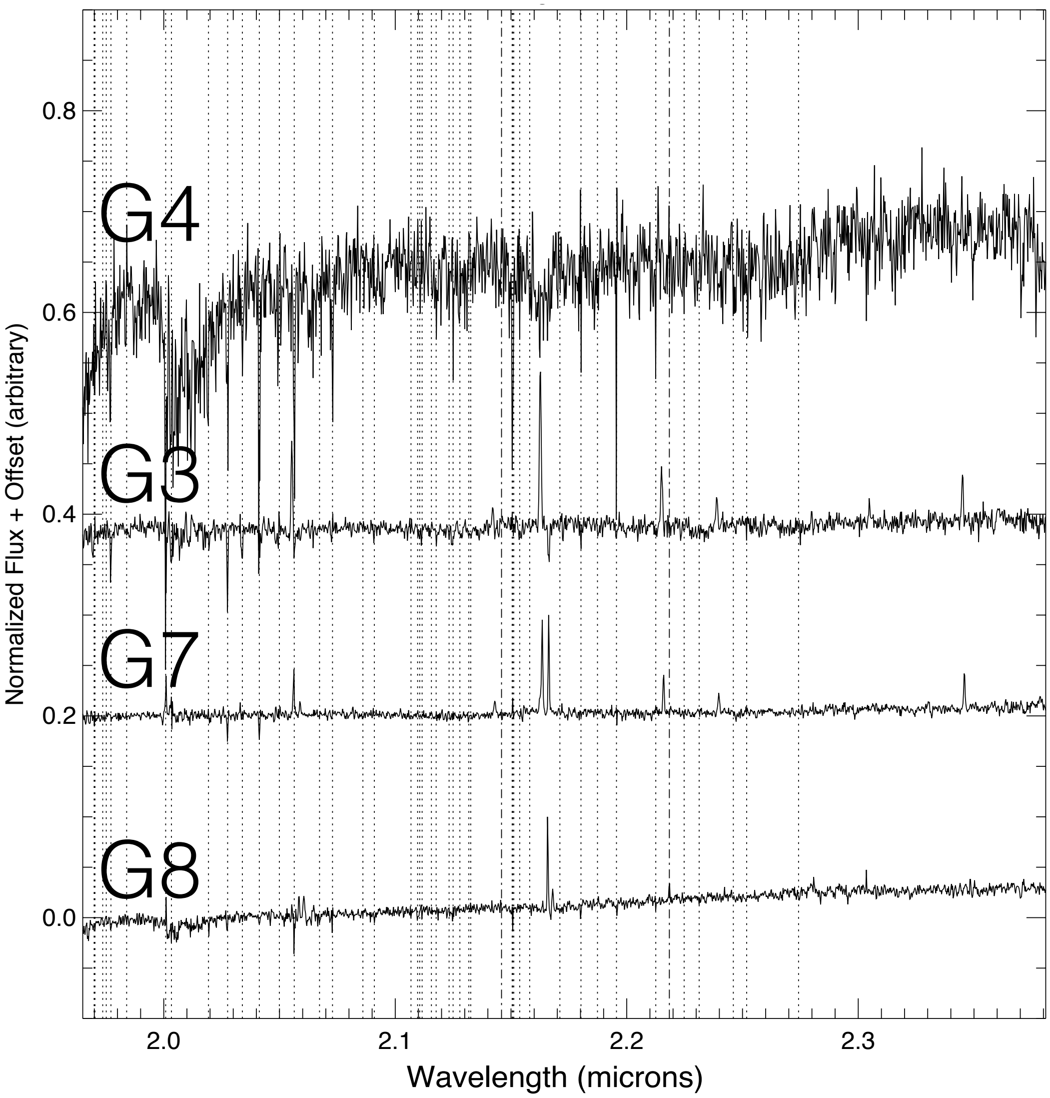

Figure 3.14 *Kbb*-bandpass spectrum of the four sources within our field of view. There is no evidence of CO band head emission in any of our spectra.

that is photoionized by the radiation field in the Galactic Center. In fact, in a study on the "comet-like sources" in the Galactic Center, Mužić et al. (2010) posit that the shape and evolution of the two comet sources could stem from an external wind or outflow with enough momentum to drive high shock velocities. This is possible if one considers the entire disk of mass-losing stars (Paumard et al., 2006a; Yelda et al., 2014) in the central parsec to drive an outflow perpendicular to the clockwise disk with an opening angle of $\sim 30^{o}$. This could also account for the existence of the mini-cavity ~ 3.5 arcseconds southwest of Sgr A*.

The Br-γ sizes are reported in Table 3.6 come from fitting our 2009 Br-γ narrow-band image with Gaussians convolved with point spread functions after aligning our 2009 L' star list to our Br-γ star list as it is closest in time. Most of our Br-γ emitting infrared excess sources seem to have gas radii less than 400 AU, but with large error bars.

We also compute the Br-γ luminosities of all of our sources in a manner similar to what is outlined in Sitarski et al. (2016) and Phifer et al. (2013) by comparing S0-2's flux density directly to G1's flux density. We estimate S0-2's dereddened flux density to be 14.1 ± 0.2 mJy Ghez et al. (2008). The wavelength ranges over which we compute the Br-γ flux density for each source is located in table 3.6, and the extracted luminosities are plotted in Figure 3.15. The wavelength ranges were chosen based on the width of the line for each infrared excess source. Both the spectrum of the star and the spectrum of S0-2 had the same wavelength range of integration so that their fluxes can be directly compared. The sources with high Br-γ luminosities are located in regions of high dust, and most tend to have narrow FWHMs in comparison to other sources in the vicinity.

The luminosities of the [Fe III] emission lines are shown in tables 3.7 and 3.8. These were calculated in the same way as the Br-γ luminosities and over the same $\Delta\lambda$ intervals. We hypothesize that the [Fe III] emission we see is largely linked to an abundance of gas in this region of the Galactic Center that is being shocked. The shock is fueled by either the same phenomenon that formed the mini cavity, or it comes from the strong stellar winds from the IRS 13 region to the southwest. That is, the gas shells are being externally ionized by a radiation field that is likely causing the appearance of [Fe III] emission and Br-γ emission.

Table 3.6. Br-γ Luminosities (milli-$L_\odot$) and Sizes (AU)

Name	2006.495	2008.487	2009.344	2010.349	2012.556	2013.366	2014.382	Wavelength Range of Integration (μm)	Measured Sizes
G7	1.24±0.78	0.40±0.23	0.51±0.41	0.54±0.19	1.06±0.84	1.57±0.31	1.30±0.59	2.1605 - 2.1640	113±16
G3	1.61±0.62	1.48±0.40	3.16±0.87	0.85±0.25	3.12±2.35	1.77±0.31	2.23±0.82	2.1610 - 2.1643	164±40
G8	0.36±0.21	0.27±0.20	0.66±0.56	0.13±0.10		0.29±0.21	0.35±0.20	2.1670 - 2.1690	210±95
G11	1.15±0.56	0.66±0.60	0.90±0.75	0.99±0.44				2.1610 - 2.1635	Point-Like
G12		6.09±2.05	5.89±1.30				6.93±3.41	2.1605 - 2.1635	144±69
G13		3.09±0.97					2.51±1.29	2.1605 - 2.1643	Point-Like
G5	0.50±0.37	0.46±0.32	0.55±0.43	0.57±0.38				2.1615 - 2.1643	330±96

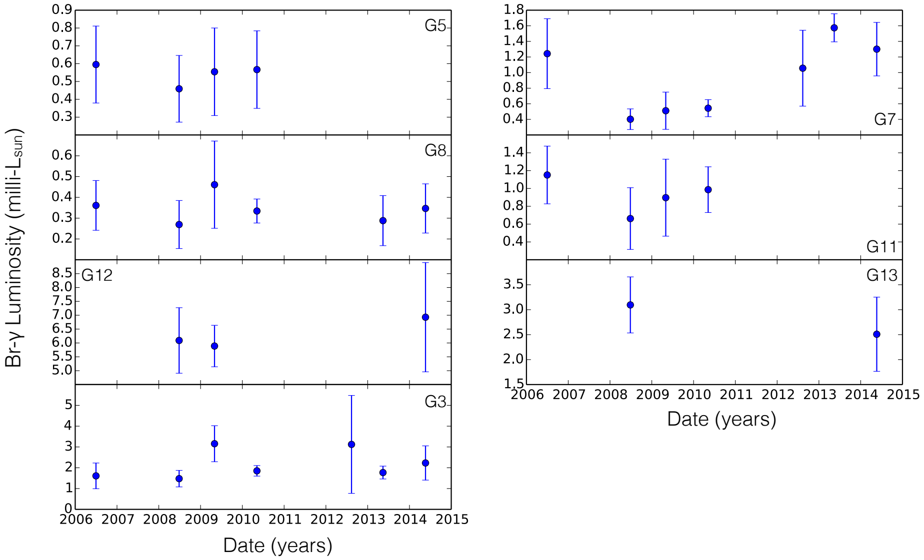

Figure 3.15 Br-γ luminosities of our infrared excess sources as a function of time. Most do not show any significant temporal evolution within their error bars. Interestingly, the sources with high Br-γ luminosities are located in regions of high dust, and most tend to have narrow FWHMs (see Table 3.10).

Table 3.7. [Fe III] ($\lambda_0 = 2.1459\mu$m) Luminosities (milli-L$_\odot$)

Name	2006.495	2008.487	2009.344	2010.349	2012.556	2013.366	2014.382
G7	0.80±0.46	0.39±0.52	0.25±0.53	0.25±0.39	0.14±0.28	0.36±0.15	0.17±0.33
G3	0.50±0.29	0.31±0.22	0.36±0.24	0.26±0.18	0.53±0.32	0.29±0.10	0.39±0.16
G11	0.90±0.60	0.66±0.60	0.55±0.43	0.28±0.10			
G12							1.17±0.78
G13		0.24±0.20					0.44±0.23

Table 3.8. [Fe III] ($\lambda_0 = 2.2184\mu$m) Luminosities (milli-L$_\odot$)

Name	2006.495	2008.487	2009.344	2010.349	2012.556	2013.366	2014.382
G7	1.01±0.27	0.63±0.14	0.48±0.24	0.39±0.23	0.41±0.24	0.70±0.20	0.71±0.30
G3	0.79±0.34	0.46±0.40	1.10±0.52	0.50±0.22	0.95±0.42	0.82±0.15	0.66±0.36
G11	1.10±0.23	1.15±0.31	2.07±1.10	0.82±0.51			
G12			2.74±0.62				4.04±1.60
G13		0.38±0.23					1.70±0.90

It is noteworthy that we do not see any CO bandheads in emission at all. There could be several reasons for this: these sources are extremely faint at K', so if the bandheads are present, they might be too shallow to observing in our current data. That being said, CO bandheads in absorption were seen in our mosaicked 2013 data cube for the $K' = 17.2$ magnitude source S0-38 (Boehle et al., 2016), which is a harder detection to make.

All spectra over the Kn3 wavelength bandpass are plotted in Figures 3.5 - 3.14; Figure 15 plots all of our *Kbb* spectra.

3.4.3 L' Photometric Evolution

As all members of our sample are required to be in at least three epochs for a calculation of the proper motion, we can also monitor the evolution of the L' photometry for each of our sources in the epochs when they are detected. This is shown in Figure 3.16. Most of the sources do not have much variation, but it is arguable that G10 and G9 show clear evolution, while G4 has some small linear evolution over time. We discuss in section 3.5.4 why these objects might have L' temporal variation. We utilize our 2005 photometric points in the following section to compute the blackbody temperatures of each of the sources.

3.4.4 Blackbody Temperature distribution of sources

Determining the temperature distribution of our sources elucidate whether or not all "G2-like" objects have similar temperatures to G1 and G2. G1 and G2 were both shown to have

Table 3.9. Radial Velocities measured from Br-γ emission features (km/sec)

Name	2006.495	2008.487	2009.344	2010.349	2012.556	2013.366	2014.382	a_z (km/sec/yr)
G4	256.21±38.57	216.30±163.53	266.62±30.75	269.36±60.27		293.41±9.04	300.52±10.66	6.3±3.9
G12		-583.47±4.23	-528.98±50.56				-549.92±5.20	-2.0±1.1
G3	-597.24±6.31	-581.12±32.11	-528.20±7.66	-503.40±4.54	-470.76±14.19	-451.53±2.36	-430.33±4.27	20.3±0.8
G7	-585.10591±53.14	-440.63±32.11	-469.46±25.27	-516.35±56.60		-340.00±0.42	-354.74±6.29	25.8±1.6
G13		-449.89±2.42					-427.03±104.43	
G11	-447.61±90.75	-462.78±86.15	-458.70±116.59	-460.34±78.43				-5.1±47.7
G5	-455.27±51.11	-446.08±17.17	-466.43±22.77	-557.44±137.13				-11.6±18.5

Table 3.10. FWHM of Br-γ lines (km/sec)

Name	2006.495	2008.487	2009.344	2010.349	2012.556	2013.366	2014.382
G4	108.79±19.17	249.54±196.67	83.14± 79.97	136.06±84.31		109.80±19.03	85.70±49.10
G12		146.55±47.68	112.12±70.46				86.90±11.94
G3	148.207±29.46	230.31±91.29	163.39±68.28	144.32±58.36	149.15±75.40	121.26±11.90	107.86±17.30
G7	-409.84±176.11	139.62±11.33	231.46±102.51	380.10±70.35	105.85±5.57	91.55±25	97.95±14.22
G13		240.80±94.13					82.02±50.73
G11	135.67±84.86	101.45±29.61	81.66±64.15	127.41±64.90			
G5		202.51±161.87	258.28±83.70	333.41±96.52			

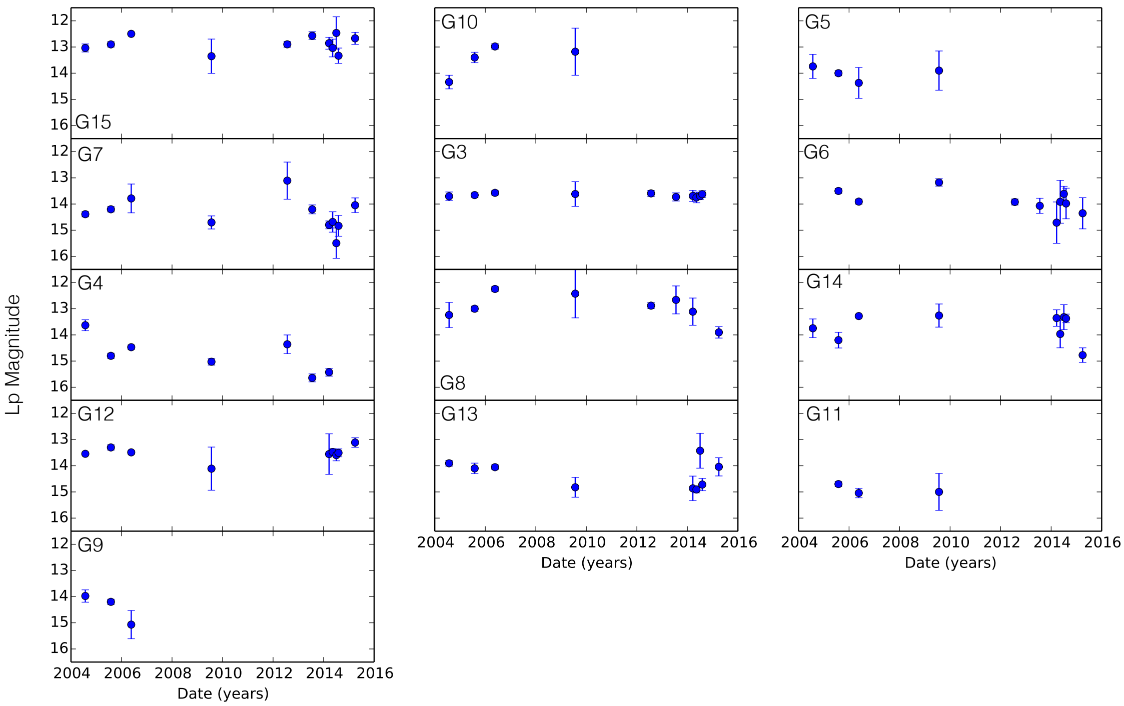

Figure 3.16 L' magnitude evolution of our infrared excess source sample. While most of the sources stay constant with time, a few of the sources evolve. For instance, G10 and G9 show clear evolution, while G4 shows some small linear evolution over time.

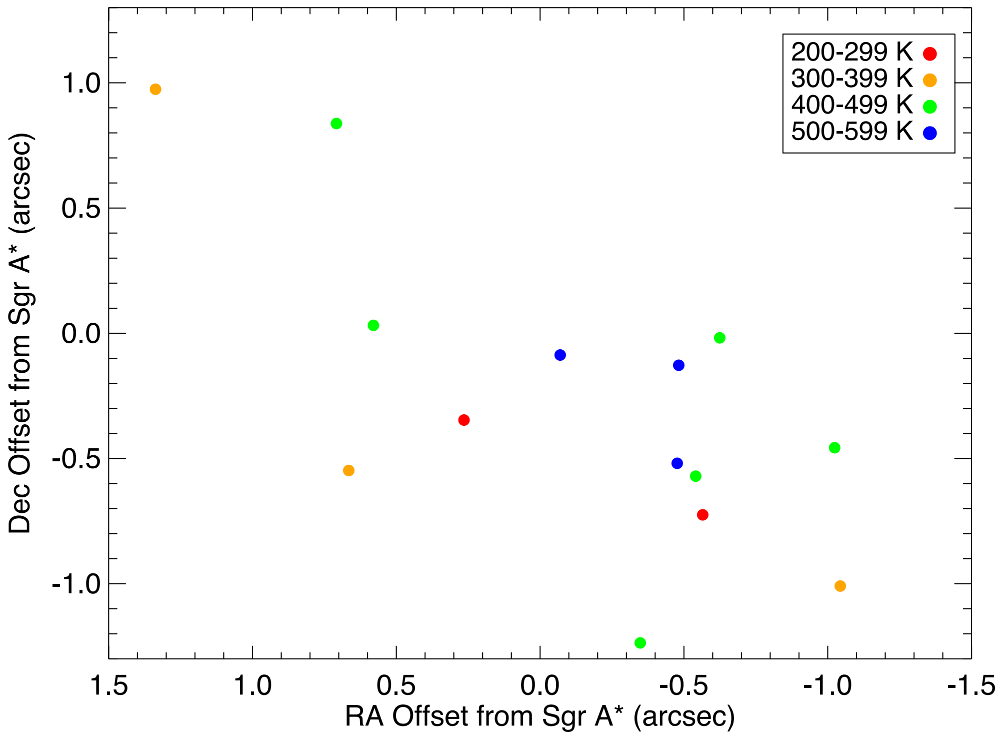

Figure 3.17 Our distributions of blackbody temperatures from all of our sources assuming all of them are optically thick. The color of the point indicates the temperature bin.

cold dust temperatures (e.g., Sitarski et al. 2016; Witzel et al. 2014; Gillessen et al. 2012) based on L' - Ms color temperatures. To infer the temperatures of our sources, we treat them all as blackbodies and use the L' and Ms extinction-corrected magnitudes:

$$L' - Ms = -2.5 \log \left[\frac{B_{L'}(T_{dust})}{B_{Ms}(T_{dust})} \right] \tag{3.3}$$

The distribution across our field of view of our temperatures is shown in Figure 3.17 below where the colors correspond to the L' - Ms derived temperature. Overall, the objects closest to Sgr A* and the S-star cluster in 2D projection tend to be the warmest; the sources furthest away tend to be closer to dusty regions (i.e., near the mini-cavity and the northern arm of the mini spiral). Our inferred blackbody temperatures are presented in Table 3.12.

3.5 Discussion

3.5.1 Did G2 survive periapse passage?

One of our sources that is immediately extracted from our color selection criteria is G2. As shown in Witzel et al. (2014), G2 was compact at L' very shortly after periapse passage (up to six months following it's periapse passage time of 2014.2). However, it was not clear whether G2 would remain intact longer after periapse, or if it would swell up in size like G1 (Sitarski et al., 2016). It was also unclear if G2 would get brighter after periapse, as suggested by the gas-cloud based models (e.g., Gillessen et al. 2012).

As part of its program to monitor the periapse passage and post-periapse passage evolution of G2, the UCLA Galactic Center acquired 2015 L' data as described in Table 3.1. Interleaved data were taken at K' and L' so that the flux of Sgr A* could be subtracted out and that the position of Sgr A^* could be determined (see Witzel et al. 2014 for details). The K' and L' star lists from *StarFinder* were aligned so that they were in a common coordinate system, and nearby sources to G2 were subtracted (S0-2, S0-8, and Sgr A*). The positional accuracies of S0-2, S0-8, and Sgr A* are dominated by the alignment of the two data sets.

The left panel of Figure 3.18 shows our L' map with Sgr A*, G2, S0-2, and S0-8 labeled. Sgr A*, G2, and S0-8 are clearly confused, but since S0-8 and S0-2 have known L' magnitudes and we can infer Sgr A*'s L' flux from its K' flux. After subtracting these sources using the extracted PSF from *StarFinder*, we are left with the center image: There is very clearly a single source in the vicinity of where Sgr A*, S0-8, and S0-2 were subtracted. To determine if G2 remained point like, a 13.6 magnitude point source was subtracted at the position of the centroid of the source; a clean residual is left over. Therefore, we can conclude that G2 is not only point-like more than a year after periapse passage, but it remained at a brightness ($L' \sim 13.6$ magnitudes) consistent with previous L' fluxes of G2 (Witzel et al., 2014).

The fact that G2 remained intact and compact a year after periapse passage further supports the hypothesis that G2 is likely a star. It also further supports evidence presented in Witzel et al. (2014) that the L' source that we see is an optically thick dust shell that

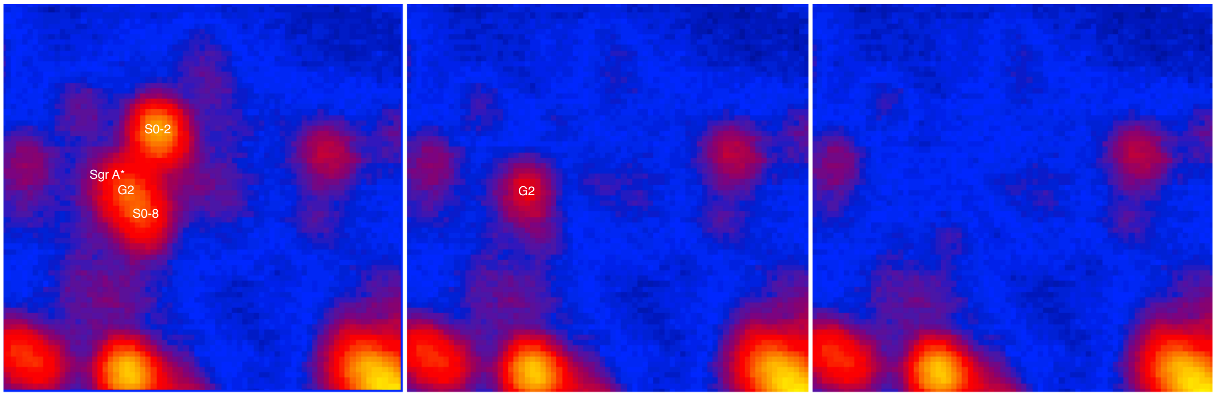

Figure 3.18 *Left*: L' map from 2015 showing the central pointing of the Galactic Center. Sgr A*, S0-8, and G2 are clearly confused. *Center:* The same pointing as shown on the left, but with point sources subtracted at the position of Sgr A*, S0-2, and S0-8 with their appropriate flux contributions (see text for details). A clear point source remains at the position of G2. *Right:* The same as the center, but with an $L' = 13.6$ magnitude point source subtracted at the position of G2. The residual is clean, implying that G2 remained compact even a year after periapse passage.

stays at a constant temperature and size.

3.5.2 Kinematic Structure of Infrared Excess Sources

Since several sources in our sample do not meet the criteria required for full orbital fits, we were able to use their proper motions to determine if they: (1) were with agreement with Eckart et al. (2013)'s reported L' proper motions; and (2) if any of the objects were proper motion measurements and radial velocity measurements had trajectories that were aligned with the clockwise disk of young stars. Figure 3.3 shows the proper motions for all our infrared excess sources except G1, G2 (both of which have a full orbital analysis outlined in Sitarski et al. (2016) and have recently–within the last 15 years–passed through periapse passage around Sgr A*) and the cometary source X7 (as a full analysis was done in Mužić et al. 2010).

As discussed in Section 3.4.1, most of our proper motion measurements are within agreement with Eckart et al. (2013). While Eckart et al. (2013) present proper motions as measured in three bands (L', K', and H), their proper motions are not aways consistent with each other, yet they adopt the average value across bands as their final reported proper motion value (see Table A.1 in that paper). This is true for several of their sources, which could point to incorrect K' and H identification of sources that are identified at L'.

G1 and G2 are on highly eccentric orbits with orbital planes very near alignment with the clockwise disk of stars, leading to the hypothesis that both objects could have been scattered off the disk (Madigan et al., 2016). Our objective is to see whether or not all these stars have orbital planes whose normal vectors align with the normal vectors presented in Yelda et al. (2014) for the clockwise disk ($i = 130 \pm 15$ and $\Omega = 96 \pm 15$). We performed orbital fits with the motion of the black hole set to zero and the mass and distance set to that given in Table 2.4 in Chapter 2 and performed orbital fits for all sources that had astrometric and radial velocity data. The resulting angles describing the orbital plane are plotted in Figure 3.20.

None of the sources have orbital planes that are aligned with the clockwise disk, implying that none of the infrared excess sources we have presented lie on the disk and possibly

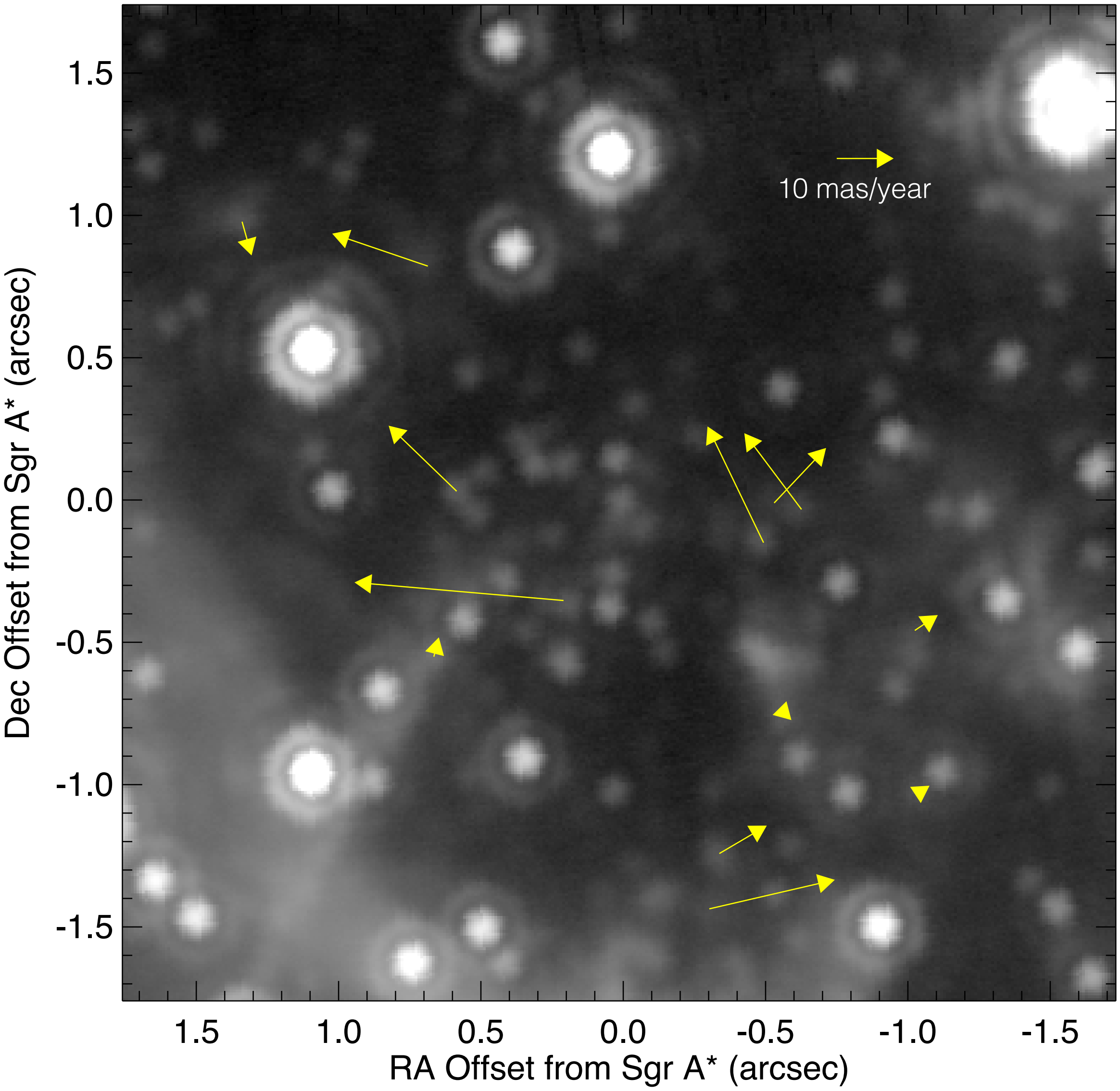

Figure 3.19 Proper motion vectors plotted over a 2005 L' image. In this figure, north is up and east is to the left. Many of the objects are moving perpendicular to the clockwise disk of young stars (Lu et al., 2009; Yelda et al., 2014), while others are moving either along or opposite to the disk rotation.

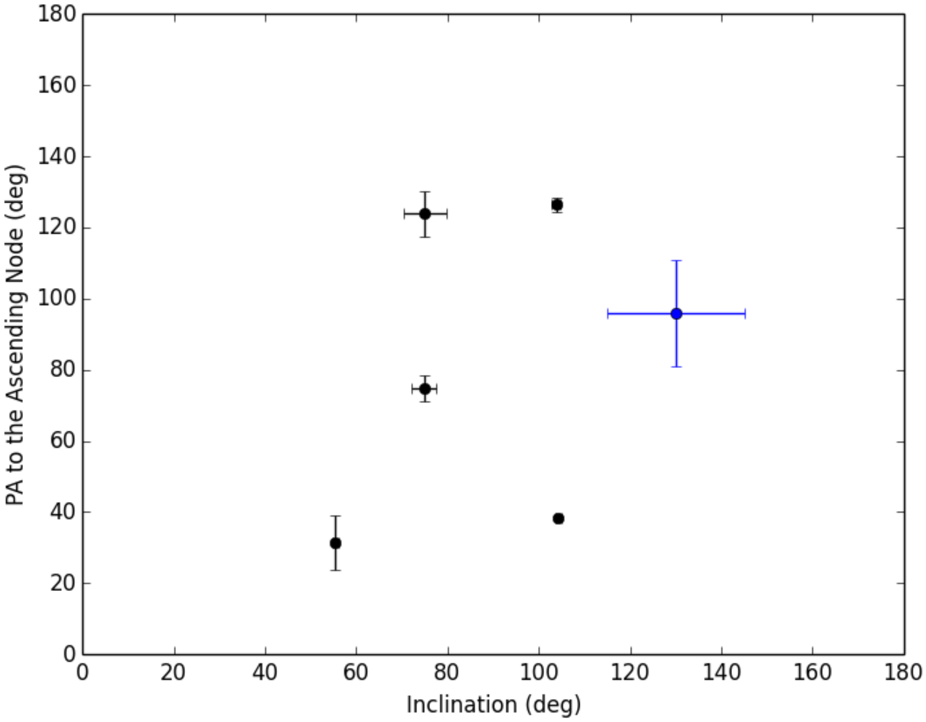

Figure 3.20 Orientation of the infrared excess sources' orbital planes. The blue point indicates the CW disk of young stars with its error bars reflecting the opening angle of the disk. None of our sample members with radial velocity measurements except G1 and G2 (see previous chapter) lie close to the CW disk.

may have never had orbits consistent with the disk. However, these objects could still be associated with the young stars, as ∼80% of all young stars near the central potential are not member of the clockwise disk. Nonetheless these sources did not necessarily originate from a single place given the lack of orbital plane alignment.

3.5.3 G3: a G2-like object on a different orbital plane than G1 and G2

One of the most peculiar sources that falls out of our selection criteria is G3. G3 has similar L' and Ms magnitudes as G1 ($Ms_{G1,2005}$ = 12.7±0.3; $Ms_{G3,2005}$ = 12.7±0.4, $L'_{G1,2005}$ = 13.6±0.1, $L'_{G3,2005}$ = 13.7±0.1), and looks slightly elongated in each epoch. The elongation is likely due to residual flux from K' sources. Like G1 and G2, G3 has a large blackbody radius (∼10 AU) and high inferred luminosity (∼125$L_\odot$); it is also resolved at Br-γ. Unlike G1 and G2, though, G3 does not show evidence for L' or Br-γ size or luminosity evolution (see Figure 3.21). G3 also exhibits [Fe III] emission lines that are consistent with the Br-γ radial velocity, which, as outlined in Section 3.4.2, could arise from the high radiation fields externally ionizing an abundance of gas.

One of the most peculiar aspects of G3 is its orbit. As G3 is one of the few sources with significant acceleration in the z direction, a full Keplerian orbital fit was performed, and a full description of its orbital parameters is presented in table 3.11. Most notably, G3 lies on a completely different orbital plane compared to G1 and G2 and seems to have a low-eccentricity orbit while G1 and G2 both had very high eccentricity orbits. Figure 3.22 shows the marginalized 1D histograms for G1, G2, and G3 over-plotted for the six Keplerian orbital elements.

The lack of size evolution and luminosity evolution that we saw with G1 (Sitarski et al., 2016) is likely due to no strong tidal interaction of G3 with Sgr A*. Our orbital analysis suggests that G3 went through periapse passage in 2005.5, but its periapse distance was ∼5000 AU–too far away from Sgr A* for it to undergo a similar tidal interaction that G1 experienced. The narrow Br-γ lines and lack of luminosity evolution in either Br-γ or L' for G3 supports this hypothesis. G3's Br-γ size is hardly resolved as well. While G1 appears

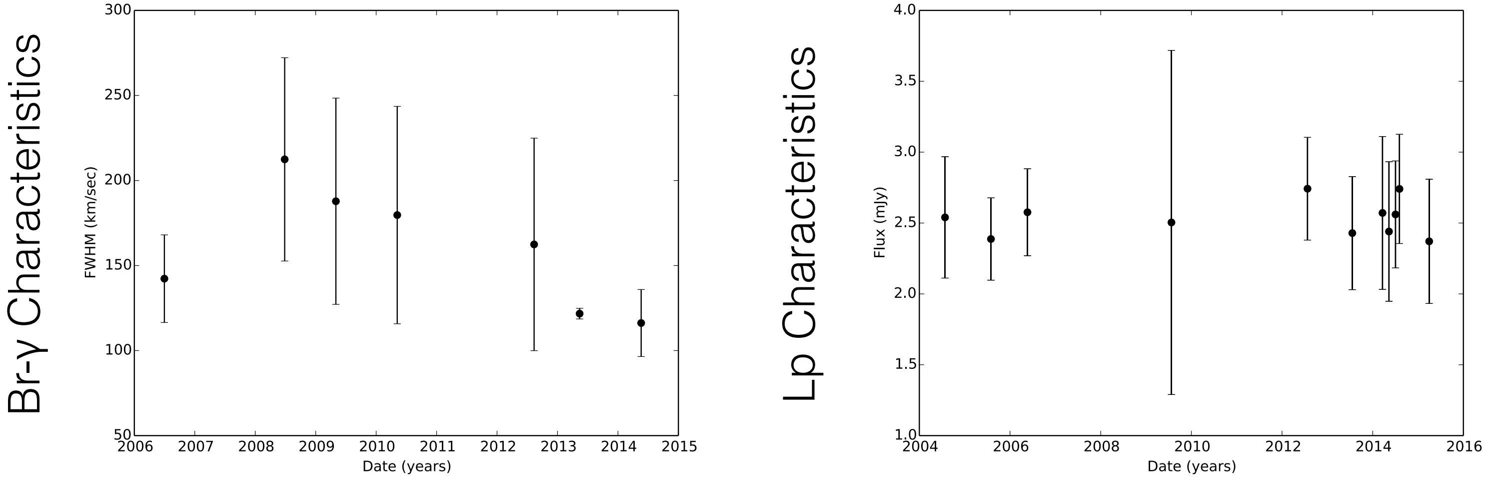

Figure 3.21 *Left:* FWHM of the Br-γ lines as a function of time. There is very little evolution of the FWHM, and all lines are quite narrow compared to G1 and G2's pre-, during, and post-periapse passage widths. *Center:* Br-γ luminosity for G3 as a function of time. G3 is comparably luminous at Br-γ as G1 and G2, particularly in early years. The spectra of later years may be contaminated from data reduction effects. *Right:* G3's L' flux stays roughly constant as a function of time. Flux contributions from nearby sources that are confused with G3 at given epochs (e.g., S0-60 and S0-43) are subtracted out assuming that they have the same colors as our calibrator sources (see Sitarski et al. 2016 for more details on this procedure).

Table 3.11. Keplerian Orbital Parameters for G3

Orbital Parameter	Best Fit	Peak of Probability Distribution
Period (P, years)	391	$385^{+5.8}_{-90.2}$
Epoch of Periapse (T_0, years)	2005.5	$2005.5^{+2.1}_{-1.1}$
Eccentricity (e)	0.40	$0.41^{+0.05}_{-0.06}$
Inclination (i, degrees)	59.9	$59.9^{+1.0}_{-0.5}$
Argument of Periapse (ω, degrees)	-134.8	$-134.0^{+0.7}_{-1.8}$
PA of the Ascending Node (Ω, degrees)	47.7	$48.0^{+0.9}_{-1.0}$

marginally larger than a point spread function, it is likely due to confusion with background sources.

G3 is also a strong Br-γ emitter with very narrow Br-γ emission lines (see Figure 3.21). While the the FWHM of the G1 Br-γ emission lines are much larger, that could have been due to tidal shearing shortly after periapse (as the measurement reported in Sitarski et al. (2016) was taken 5 years after periapse passage). G3 also exhibits [Fe III] emission lines that are consistent with the Br-γ radial velocity. Interestingly, the Br-γ size measured over time shows a smaller Br-γ size than L' size. We therefore propose that the resolved L' source is an optically thin shell, and we see the Br-γ gas envelope slightly internal to the optically thin shell. Internal to that, there is an optically thick shell around a compact stellar object.

The fact that G3 lies on a different orbital plane than G1 and G2 and has similar observational characteristics provides further evidence that G1 and G2 are likely not peaks in a single gas streamer: if G1 and G2 were indeed part of the same gas streamer on the same orbital trajectory, G3 should be moving on the same trajectory, have a high eccentricity, and have a far lower periapse passage distance than our orbital fits imply. Interestingly, G3's orbital plane does not lie close to the clockwise disk of young stars; in fact, it's proper motion is nearly perpendicular to the clockwise disk (see Figure 3.22). It was hypothesized by Madigan et al. (2016) and McCourt & Madigan (2015) that G1 and G2 could have come from the clockwise disk, but this analysis does not conclude that G3 did not come from the young stars, as 80% of young stars lie off the clockwise disk.

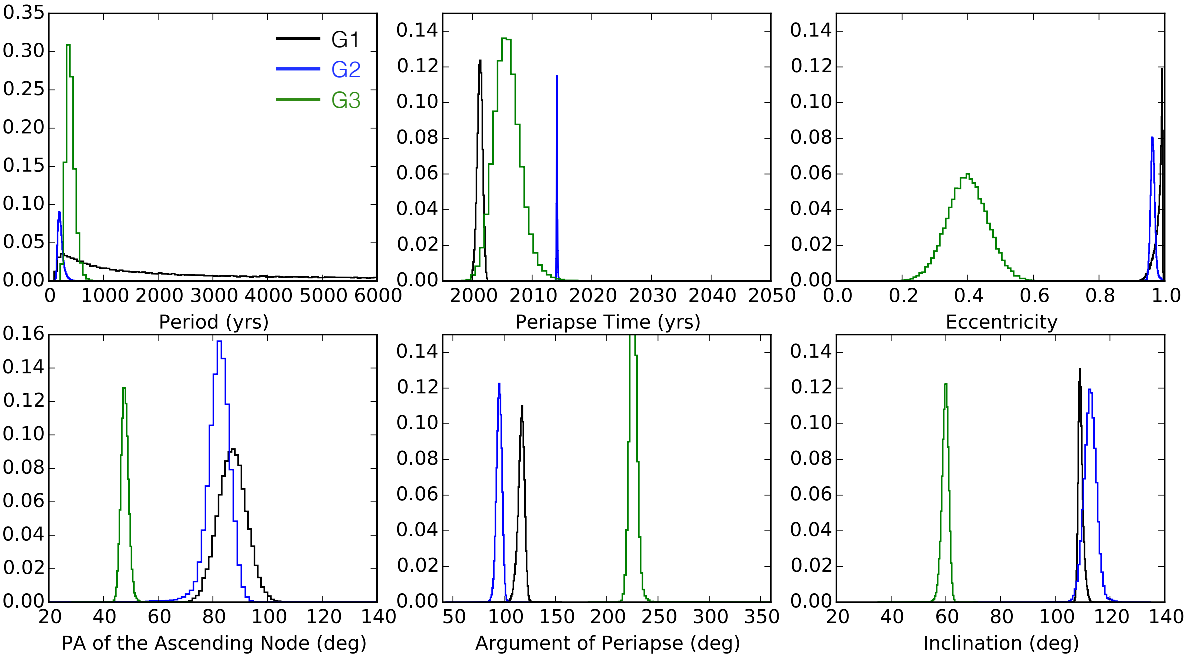

Figure 3.22 1D marginalized probability distribution functions of the Keplerian orbital parameters of G3 (green) compared to G1 (black) and G2 (blue). It is evident that G3 has a much lower eccentricity and lies on a different orbital plane than G1 and G2.

G3 therefore supports the hypothesis that there is a population of objects that share similar observational qualities to G1 and G2–high infrared luminosities, cold dust temperatures, and Br-γ emission line features. G1, G2, and other G2-like sources might therefore exist as a new population of sources in the Galactic Center. We speculate in the next section what the nature of this population could be and whether all the infrared excess sources that are part of our sample are members of the same class.

3.5.4 Gas clouds, dust clumps, or stars?

Following the analysis in Eckart et al. (2013), we determine if the infrared emission that we see in our sample could arise from pure dust sources or a mixture of dust and photospheric emission from stars. Figure 3.23 shows a color-color diagram of K' - L' vs. L' - Ms magnitudes for all point sources detected in our L', K', and Ms combined images. If the objects were pure dust sources, they would fall close to the dotted line plotted on our color-color diagram. While Eckart et al. (2013) detects G2 (DSO) and several other sources at at K', we do not detect most of our sources through the K' filter and we therefore obtain limits on their K' magnitudes.

Eckart et al. (2013) show that sources lying below the blackbody line can be mixtures of both dust and stellar photospheric emission. While many of the sources are clustered at the blackbody line and even sometimes above it (implying that they are possibly pure dust clumps [on line] or stars with hot [$T_{dust \sim 1000}$ K] dust surrounding them [above line]), the photometric error bars from our Ms photometry could push these sources to being a mixture of stellar photospheric emission and dust. Therefore, the model that we adopt is similar to what is outlined in Sitarski et al. (2016) and Witzel et al. (2014): these sources are stars with dust shells surrounding them; those that have Br-γ emission have gas envelopes around them that are being externally ionized by the massive stars in their vicinity.

Following the same analysis in Witzel et al. (2014) and Sitarski et al. (2016), we assume that our entire sample consists of optically thick blackbodies and calculate the blackbody radii of all members of our sample (Table 3.12). The results of this analysis is striking:

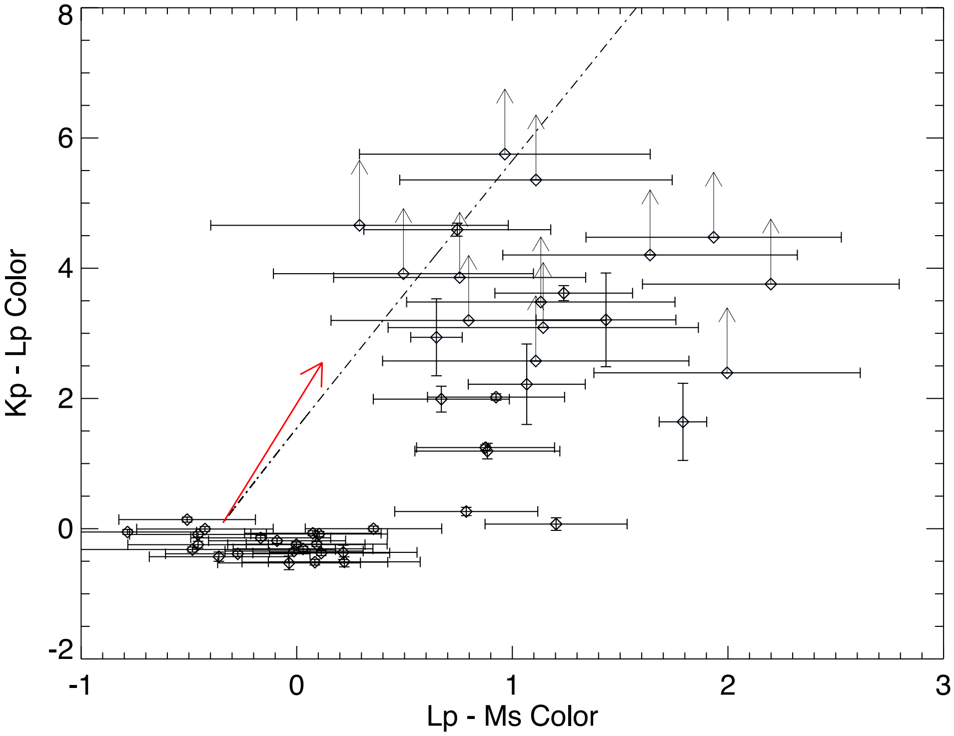

Figure 3.23 Color-color diagram of our IR excess sources compared to a pure blackbody. The dotted line signifies the blackbody line, while the red vector shows our reddening vector. The main sequence is very near (0,0) on this plot, while the infrared excess sources are to the upper right.

Table 3.12. Inferred Blackbody Properties

Name	Temperature (2005; K)	Radius (AU)	Measured intrinsic FWHM (2005; AU)	Luminosity ($L_\odot$)	Mass ($M_\odot$)
G15	283.6	118	713±18	3750	6
G10	350.1	25	1013± 114	406	4
G5	480.9	4	<170	40	2
G7	346.5	19	<170	211	3
G3	406.0	10	Confused?	125	3
G6	356.7	21	<170	318	4
G4	251.5	112	215±62	2100	6
G8	268.9	157	<170	5387	7
G14	306.1	38	341±74	531	6
G12	373.8	19	273±46	292	6
G13	256.5	136	313±33	3347	6
G11	344.8	14.7	<170	127	3
G9	236.2	250.6	284±37	8146	7

all of our sources are very large ($r_{BB} > 4.0$ AU), far larger than any main-sequence star. We interpret this as our sources having very large, extended dust envelopes that are being internally heated by their central host star. We also infer blackbody luminosities from these radii and, using the SSE stellar evolution code from Hurley et al. (2000), associated masses. The masses reported in Table 3.12 can be somewhat lower if the source is a pre- or post-main sequence star that is temporally close to the main sequence (Witzel et al., 2014).

In particular, G15, G4, G8, G13, and G9 all have extremely large blackbody radii (and therefore high luminosities and large masses compared to the rest of our sample). However, their measured L' sizes are quite and they are always resolved (except for G8; see Table 3.12). These sizes were measured as in Sitarski et al. (2016) where we fit a 2D Gaussian convolved with a PSF. As these sources are likely not experiencing the same tidal effects that caused G1's L' elongation due to their distance from Sgr A* (Sitarski et al., 2016), these sources could be resolved for several other reasons: (1) they are interacting with some other nearby massive source; (2) if they are G2-like objects and therefore binary merger candidates, they may not have dynamically settled into a point source (that is, their extended dust cloud may still be intrinsically large); (3) these sources could be resolved dust clumps. These sources do have the largest L' - Ms colors, and Eckart et al. (2013) does list G15 (D7) as a candidate pure dust source. G15 could also likely be a bow-shock or similar object based on its morphology and its high infrared excess, which is to be expected for the dusty head of a bow shock (e.g., the IRS 8 bow shock from Geballe et al. 2004). G9 is extremely close to the comet-shaped source X7; in fact, in later epochs, it becomes spatially confused with X7. G4 lies along multiple streamers of dust coming off the northern arm of the mini-spiral which could significantly influence its Ms photometry; G15 is a bow-shock shaped source that could be interacting heavily stellar winds from IRS 16C. G4 and G11 are both constituents of very dusty regions whose high backgrounds could be influencing the Ms photometry.

We thus speculate most of these sources have large, extended dust shells that are internally heated by their central host star. Some of these are additionally surrounded by an envelope of gas that are externally ionized by the radiation field in the Galactic Center arising from the UV ionization. The other five sources that have large blackbody radii and very cold color temperatures may be something physically different. G8, which also has a K' detection, could be a stellar object moving through dense dust clouds that has picked up dust along its trajectory and is now heavily enshrouded. With its very luminous Br-γ emission, G13 could also follow this model.

G4 and G9 could be compact dust clumps without a stellar counterpart, the original G2 hypothesis (Gillessen et al., 2012). These could just be compact, dusty cores within an extended cloud. Not much mass would be needed for these to form; G2 was originally hypothesized to have a very low mass (∼3 Earth masses). G9 is very near the cometary-shaped source X7, which was hypothesized by Mužić et al. (2010) to have been formed in either an outflow formed from the mass-losing stars in the clockwise disk, or in whatever way the mini-cavity was cleared out. The mini-cavity could have compressed a shell around it, which has lead to Rayleigh-Taylor type instabilities that leave behind these compressed clumps. Both of these objects show L' flux evolution as a function of time, with G4 getting dimmer and G9 getting brighter as it gets closer to X7.

Another hypothesis that is applicable to all the observational characteristics seen in these sources is that they might be binary merger products, a hypothesis originally posited for G1 and G2 (Phifer et al., 2013; Witzel et al., 2014; Prodan et al., 2015; Sitarski et al., 2016). These objects all have dust temperatures that are quite cold and most are consistent with temperatures reported by observed binary merger products in Nicholls et al. (2013) and Tylenda et al. (2013). Their very apparent infrared excesses point to large dust shells surrounding the central source, and the large size and luminosities inferred for these sources are fairly similar to BLG-360. The high infrared flux densities are consistent with the high infrared fluxes from other reported binary merger products after the merger has occurred. Stephan et al. (2016) show that the fraction of possible G2-like objects with infrared excesses could be quite high and could have stemmed from the most recent large episode of star formation nearly 6 Myr ago. While we cannot know when the merger occurred for these sources if they are indeed binary mergers, their observational properties are strikingly similar to the few observed binary merger stars that have been reported.

It is possible that not all of these sources, given their temperature distributions and size distributions, belong to the same class of objects. They may be stars interacting with the ambient gas and dust in the region, particularly the sources that have K' detections, or they could be Rayleigh-Taylor instabilities formed in the dust by the same phenomenon that formed the mini cavity. All these sources interestingly share the same observational characteristics, though, and many of the sources could be the same type of object as G1 and G2, particularly those with similar temperatures and luminosities.

3.6 Conclusion

We presented observational characteristics of several infrared excess sources in the central 1.75 arcseconds of the Galactic Center. These objects all have K' - L' colors at least 0.7 magnitudes greater than the main sequence and are present within our data for at least three years. We are able to confirm the proper motions of Eckart et al. (2013), which show that these sources are not all moving in the same direction and likely do not have the same orbital orientations.

One of the defining features of G2 at its discovery was its Br-γ emission line features that were being tidally sheared as it reached closest approach. Several members of our sample show this emission line feature as well as [Fe III] emission, which likely comes from shocks arising from the same phenomenon that formed the mini-cavity or from the strong stellar winds that form IRS 13. This shock

We also present an orbital analysis of G3, which appears to have nearly identical observational characteristics as G1 and G2, but it lies on a very different orbital plane, has a very low eccentricity, and does not get very close to Sgr A*. Unlike the similar orbital plane of G1 and G2, the orbital plane of G3 is not close in angular orientation the position of the clockwise disk of young stars, but could have still originated from the disk.

While these sources share many observational characteristics, they could be physical manifestations of different types of objects, which we outline in our discussion section. Continued monitoring of these sources to see their evolution and obtain better orbital analyses could be key for determining the physical discrimination of several sources.

3.7 Black hole parameters obtained from G3 orbital fit

As we perform a complete 3-object Keplerian fit with S0-2, S0-38, and G3, we are able to re-derive the black hole parameters. We use the same reference frame as the one outlined in Sitarski et al. (2016) and Boehle et al. (2016), and we add additional epochs of data in order to reflect our longer time baseline. The black hole parameters as well as the orbital solutions for S0-2 and S0-38 from this three-source fit are described in table 3.13. It is clear that some of the orbital parameters of this fit differ from what is reported in Chapter 2; that might stem form the reference frame not being updated as more data epochs are added to our radial velocity measurements and our astrometric measurements. The reference frame was chosen so that it was consistent with that reported in Sitarski et al. (2016), as that outlines the orbits of G1 and G2.

Table 3.13. S0-2 + S0-38 Black Hole Parameter values

Orbital Parameter	Peak Fit[a]
X-Position of Sgr A* (x_0, mas)	1.26±0.33
Y-Position of Sgr A* (y_0, mas)	$-0.98^{+0.40}_{-0.26}$
ΔRA Velocity of Sgr A* (V_x, mas/yr)	$-0.17^{+0.01}_{-0.02}$
ΔDec Velocity of Sgr A* (V_y, mas/yr)	$0.77^{+0.04}_{-0.02}$
Radial Velocity of Sgr A* (V_z, km/sec)	-20.17±5.28
Distance to Sgr A* (R_0, kpc)	7.76±0.05
Mass of Sgr A* (M, Millions of $M_\odot$)	3.65±0.07
S0-2 Parameters:	
Time of Closest Approach (T_0, years)	2002.38±0.01
Eccentricity (e)	0.888±0.0006
Period (P, years)	$15.90^{+0.02}_{-0.01}$
Argument of Periapse (ω, degrees)	66.1±0.3
Inclination (i, degrees)	$133.2^{+0.1}_{-0.2}$
PA To the Ascending Node (Ω, degrees)	226.9±0.5
S0-38 Parameters:	
Time of Closest Approach (T_0, years)	2003.18±0.01
Eccentricity (e)	$0.811^{+0.003}_{-0.002}$
Period (P, years)	19.33±0.04
Argument of Periapse (ω, degrees)	84.6±4.6
Inclination (i, degrees)	$166.5^{+2.0}_{-1.2}$
PA to the Ascending Node (Ω, degrees)	2.57±5.1

[a] This is defined as the peak of the 1D marginalized distribution functions. Error bars reported here are 1σ error bars.

CHAPTER 4

Astrometry with Spatially Variable PSFs: Instrumental Field-Dependent Aberrations

4.1 Motivation

While adaptive optics observations have revolutionized our fundamental understanding of astronomy, there are still some limitations to using adaptive optics to obtain high-resolution images. For example, the use of a single-conjugate laser guide star adaptive optics systems suffers from the cone effect, where the laser does not necessarily probe the exact atmospheric turbulence that influence the science observations as the turbulence above the sodium layer (>90 km) is not sensed, nor are the outer parts of the wave-front (this is also known as focal anisoplanatism). Additionally, angular anisoplanatism in LGSAO systems affects the quality of high-angular resolution images since the wavefront from the laser and the science target can differ.

Anisoplanatism leads to spatial variation of the PSF in a single-conjugate AO system. As shown in equation 1.1, the optical transfer function can be reduced into three components: the on-axis contribution, the instrumental off-axis part, and the component measuring the AO response to the atmosphere. The goal of this project is to establish a new calibration procedure that will measure the variations in the off-axis PSF and allow us to understand the level of PSF variation that can arise from this single component. We establish a full algorithm to go from raw, out-of-focus images to a phase map grid and an interpolated model of Zernike coefficients that smoothly describes the instrumental aberrations in terms of Zernike coefficients.

The procedure will be described in the following way: (1) measurement procedures at Keck Observatory; (2) post-processing and analysis side; (3) integration of Zernike decomposition into a model of the spatial variation across the field of view of the detector.

4.2 Phase Diversity Data Collection

Phase errors can be empirically measured through fiber phase diversity data. The data presented here were taken with the illuminated LED fiber at the Nasmyth focal plane of Keck II. The aim is to use an illuminated fiber in the pupil plane, which corresponds to a position on the detector of NIRC2 in the instrumental focal plane, to measure phase aberrations at specific positions and transform them to arbitrary positions. The aim is to measure the phase of aberrations at a specific positions on the detector and transform them to arbitrary positions through instrumental modeling. Keck Observatory currently uses phase diversity to optimize static aberrations in their image sharpening procedure, which is run prior to every AO night on the NIRC2 instrument (van Dam et al., 2004). In order to extract the phase at a reference position on the detector, an image is taken at Δz = -2 mm, -4 mm, and -6 mm for NIRC2, where Δz is the distance the fiber is moved in and out of a focused position. Data cannot be taken in the opposite (positive) focal direction, as there is not enough room from the focus position for the stage to move in that direction.

Traditionally, image sharpening only corrects low-order modes, and phase diversity data makes use of short exposure times ($t_{int} = 0.181$ sec, $n_{\rm coadds} = 50$, in the CDS readout mode). While this methodology is efficient in terms of total integration time spent at each field position (72 seconds with overheads), it produces a very low signal-to-noise ratio phase map (see Figure 4.1). That is, in large part, due to the insufficient integration times for the more negative values of Δz.

With the aim to measure higher order modes, we developed an improved method of data collection that increases the signal-to-noise of our phase maps. Instead of keeping the integration times constant for each Δz, we increased the integration times and number of reads and decreased the number of coadds (see Table 4.1). While this did increase the overall

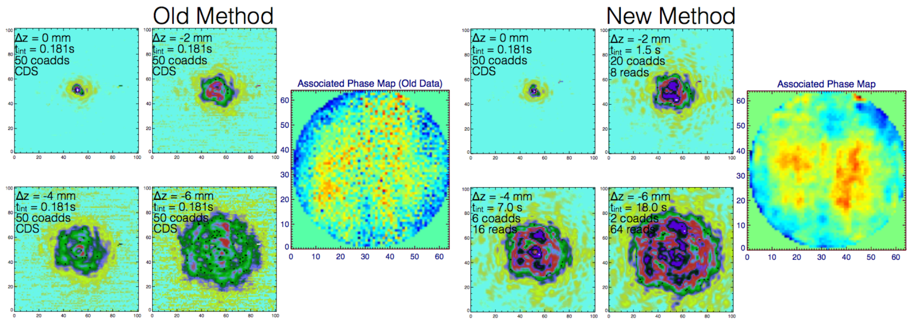

Figure 4.1 A comparison between the old method of collecting phase diversity data and our new method, which results in a much higher signal-to-noise ratio phase map.

Table 4.1 An improved method for phase diversity data collection

Δz (mm)	$t_{\rm int}$ (sec)	$n_{\rm coadds}$	$n_{\rm reads}$
0	0.181	50	CDS
-2	1.5	20	8
-4	7	6	16
-6	18	2	64

integration time significantly (213 seconds), it also yields a phase diversity map with only 12.5 nm RMS random measurement error. Since data acquisition is performed during the day and does not require use of the actual telescope (only the instrument and the AO bench), the benefits of having the higher signal-to-noise ratio phase maps far outweigh the costs of the longer integration time.

To obtain the phase at each specified position, we image sharpen at some reference point on the detector (at pixel [545, 495] for NIRC2) and take phase diversity data across the field of view of the illuminated fiber on its movable stage. The fiber is then moved to other positions on the detector to measure the field dependence of the aberrations. In total, we have taken ∼105 hours of fiber phase diversity data across the field of view of NIRC2 in its various optical setups. This has been done primarily with Randy Campbell and Greg Doppmann at Keck Observatory, along with Jim Lyke, Marc Kassis, and Luca Rizzi. This effort yielded approximately 150 phase diversity phase maps for the pre-alignment grid (see

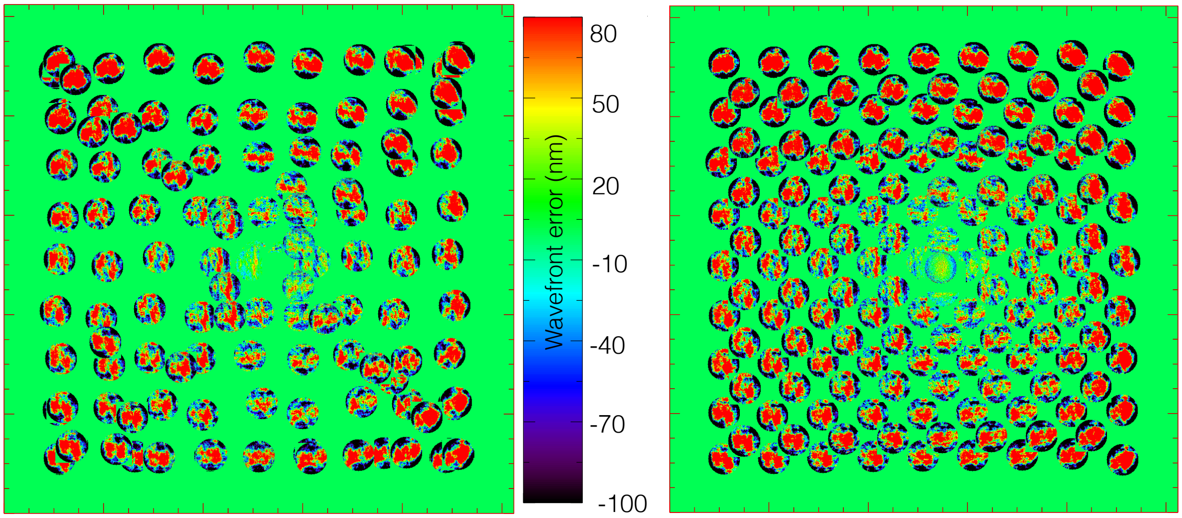

Figure 4.2 Full phase diversity data grid, where the phase diversity data is taken at various point across the field of view. There are over 150 different data sets (some taken at the same position to study time variability effects). All data are taken through the Fe II ($\lambda_0 = 1.6455\mu$m; $\Delta\lambda = 0.0256$ μm) narrow-band filter on NIRC2. The left frame shows the data before NIRC2's optical realignment, while the right frame shows the data after NIRC2's optical realignment.

section 4.2) and approximately 150 maps for the post-alignment grid. The phase maps were constructed using a modified Gerchberg-Saxton phase retrieval algorithm, which is used to construct the image sharpening phase maps (Atcheson et al., 2003). The two grids of phase diversity data are shown in Figure 4.2. At each position, three phase diversity data sets are taken (three sets of images at Δz = -2, -4, and -6 mm) to characterize the random uncertainty on the Zernike terms. Prior to moving the fiber, a reference data set is always taken at [545, 495]; we return to this position at the end to average over the two reference maps. The center position is subtracted out from all other points for that specific data acquisition run to obtain the differential phase maps.

The field extrema are useful for determining measurement error and are defined as the positions furthest from the center of the detector (and therefore defined as the four corners of the detector). The relative wavefront error between the center reference point and the corner points is, at most, 190/220 nm RMS at Fe II ($_0 = 1.6455\mu$m; $\Delta\lambda = 0.0256$ μm) for the pre-/post-alignment grids–this is a large overall error, and any decrease in this value would greatly improve the effects of non-common path errors. The average differential wavefront error between all measured phase maps and the center reference maps is 43 nm RMS at Fe II. The measurement differences between the center phase map taken at the beginning of a data collection run and the center phase map taken at the end of a data collection run is on average ∼23 nm RMS. This is the limit on how accurate we can obtain measurements at the same position over a multiple hour time period. The smallest and largest wavefront differences between adjacent phase maps is 15 and 87 nm RMS at Fe II, respectively, which corresponds directly to the sampling error present in our grid.

The adjacent samples can be used to quantify the error associated with field sampling. Figure 4.3 shows both the pre- and post-alignment NIRC2 grids connecting the points of the nearest adjacent phase map with their wavefront error. While the maps with nearby neighbors have fairly low error compared to the temporal error discussed above, they still exhibit a lot of scatter even between the maps that are close to the center reference point. Figure 4.4 plots the RMS difference wavefront error as a function of distance to the nearest phase map, which clearly shows the scatter. While there is this scatter, the overall sampling error is below the average wavefront error difference relative to the center reference point (∼100 nm RMS). The average difference between the adjacent samples is 43 nm RMS for the old grid and 47 nm RMS for the new grid. Having a finer grid would reduce the sampling error, particularly near the edges of the detector where the adjacent samples have the largest wavefront error differences; the adjacent samples near the center of the detector are very close to the measurement differences between the initial center phase map and final center phase map taken in a given data run (see previous paragraph). A table summarizing some of the errors arising form sampling in the data is in Table 4.2.

Table 4.2 Phase Diversity Grids

Quantity	Value in pre-alignment grid	value in post-alignment grid
Total Collection Time	55 hours	48 hours
Filter of Observations	Fe II & Br-γ	Fe II
Greatest difference from extrema	190 nm RMS	213 nm RMS
Between adjacent samples:		
Average WFE difference	43 nm RMS	50 nm RMS
Smallest WFE difference	15 nm RMS	15 nm RMS
Largest WFE difference	87 nm RMS	78 nm RMS

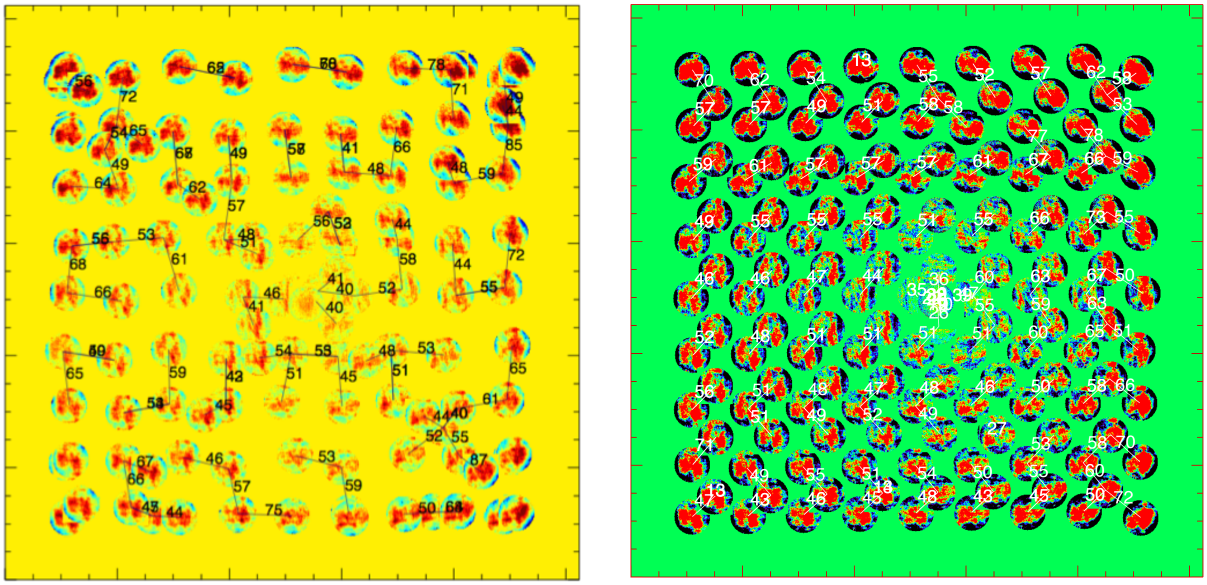

Figure 4.3 Grid of adjacent phase maps with lines connecting the nearest phase map and the associated wavefront error. The left panel shows the grid prior to NIRC2's optical realignment, and the right panel shows the grid after the realignment.

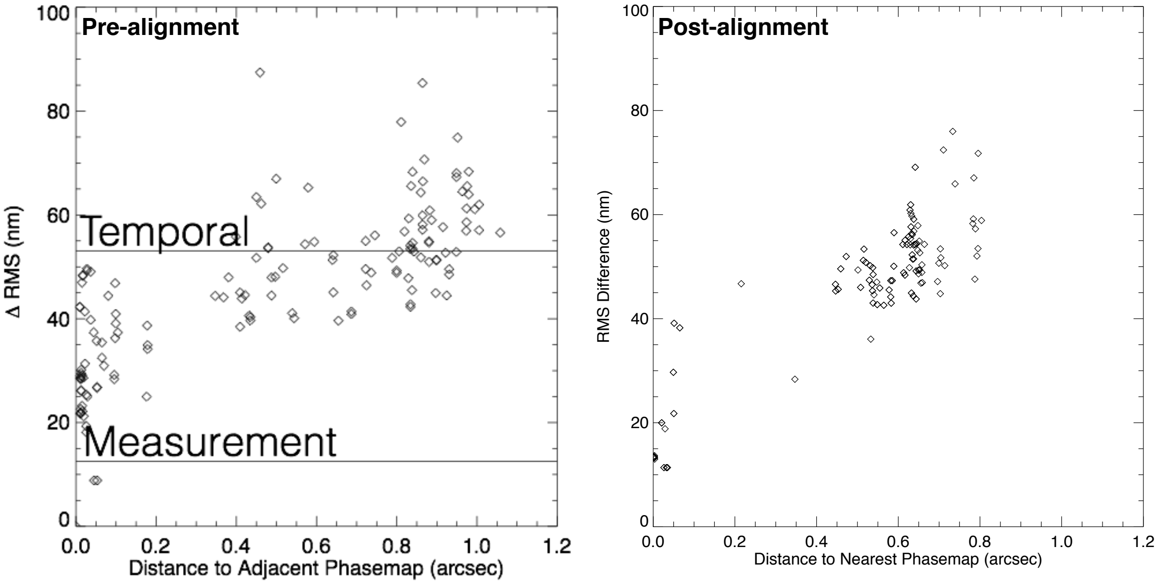

Figure 4.4 Wavefront error as a function of distance from the nearest phase map for both the old grid and the new grid. The phase maps that are close in position to each other tend to have less than the temporal variation of the wavefront error, although there is still a lot of scatter.

4.3 The Effects of Time Variability

Since taking a single set of phase diversity data is time intensive, it is necessary to take this data over a period of time, particularly since it requires the use of the AO bench and NIRC2, which are not always readily available. As such, data from the pre-alignment grid were taken over approximately a two-year period from October 2012 to December 2014, and data for the post-alignment grid were taken over a few-month period (May 2015 - November 2015). Time variability does pose a major concern in using a grid of data; in order to probe and quantify the effects of this, multiple data sets were taken at the field extrema and the center positions.

Data for the center positions were taken twice over a span of five hours to probe the temporal variability on short time periods (see Figure 4.5). Since three sets of data are taken at each position, the average phase map was constructed at $t = 0$ hours and $t = 5$ hours; these were then subtracted to compute the residual. The temporal drift over 5 hours is ∼18 nm RMS for both the old and new grids over the five hour period. The measurement repeatability at the center positions is 12.5 nm RMS. This was found by calculating the RMS after taking multiple center position phase maps consecutively.

A similar analysis was performed at the field extrema for the pre-alignment grid only. Between October 2012 and May 2014, the temporal drift over the field extrema was 53.1 nm RMS, which a measurement repeatability of 15.4 nm RMS. It is noteworthy that the 53.1 nm RMS temporal difference falls significantly below the 190 nm RMS difference between the extrema points and the reference phase map (see Figure 4.7). This is still a fairly large drift, especially compared to the measurement repeatability. There is not a specific set of modes that the large error comes from, as there is a significant amount of fractional error in the high-order modes (see left side of Figure 4.6), but there is a lot of overall power in the low-order modes (see right side of Figure 4.6). We expect that the time variability difference will not be as extreme closer to the the center due to the image sharpening procedure we run. In comparison, the difference between the center maps from October 2012 and June 2014 is 41.6 nm RMS after image sharpening. The RMS of a center phase map is ∼30 nm

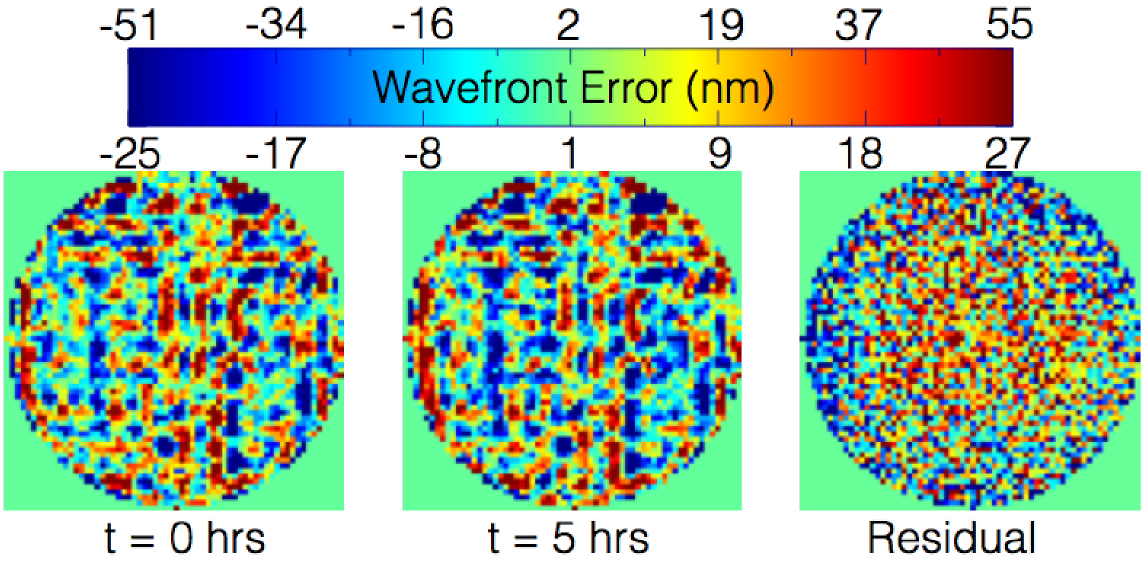

Figure 4.5 Variation of the center phase map of the pre-alignment grid over five hours. The residual primarily consists of high-order noise. The RMS in the residual is 18 nm RMS. The top scale corresponds to the wavefront error in the first two figures; the bottom scale corresponds to what is left in the residual.

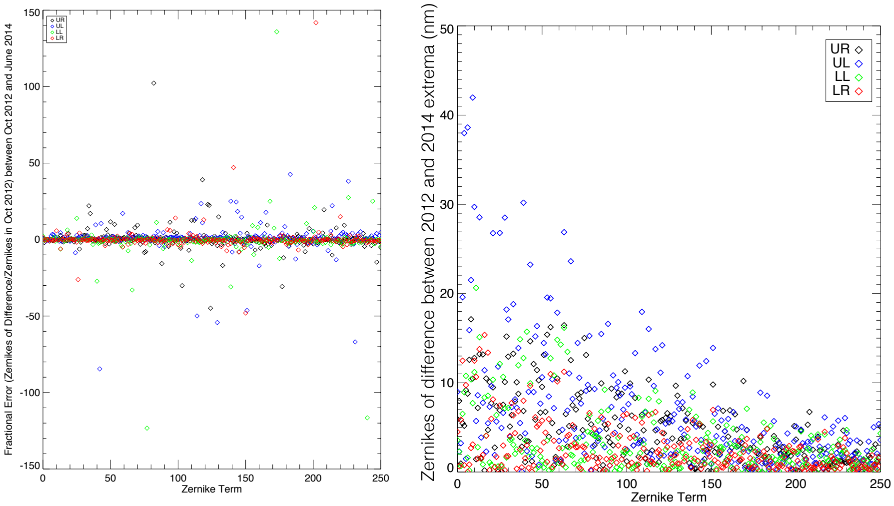

Figure 4.6 *Left*: A plot of the fractional difference in the OTFs of October 2012 and June 2014 normalized by the extracted Zernike coefficients from October 2012. There is no single mode that contributes a lot of fractional error. Instead, *Right*: A plot of the difference in the OTFs of October 2012 and June 2014. There seems that there is no set series of modes that dominate; rather, the low-order modes seem to contribute the most power.

on average, implying that this is primarily measurement error and not dominated by time variability. A plot of the variability of the four extrema points as a function time since October 2012 is shown in Figure 4.8, where it seems that the time variability plateaus and does not increase substantially a year after we started our initial data acquisition.

A fraction of the error arising from time variability is common mode (that is, some shape that shows up in all of the phase maps) that is consistent between all extrema points. The top row of Figure 4.9 shows phase map from three different epochs. At each extrema point, all epochs are averaged over and subtracted to yield the second row. To determine if there were any common-mode errors in a given epoch, the results of the second row were averaged over a given epoch and subtracted from the second row. This results in a field-dependent wavefront

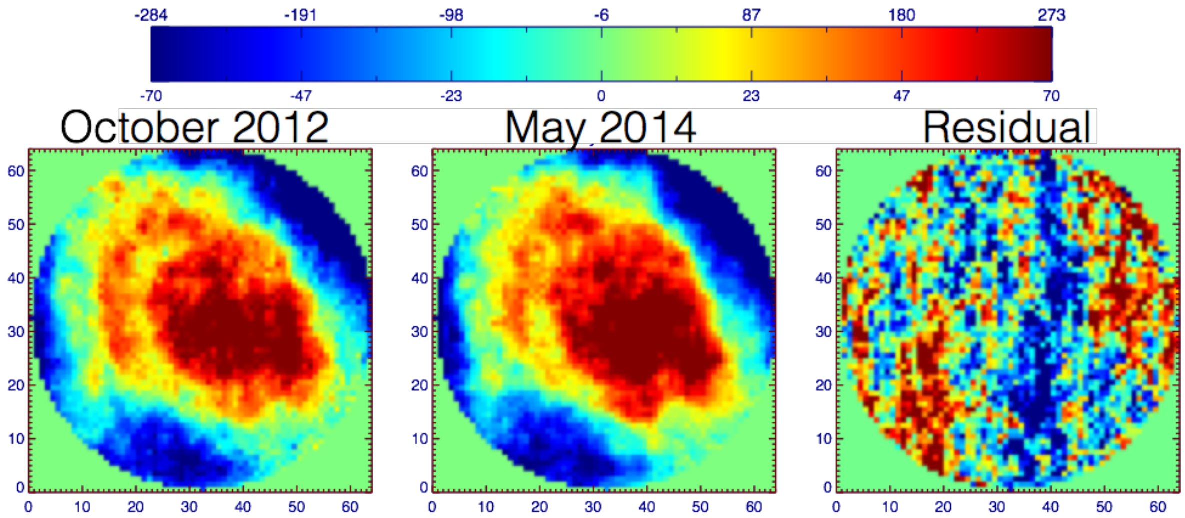

Figure 4.7 Variation of one of the field extrema points (corner positions) as a function of time. The general morphology of the phase map stays the same, but the residual seems to consist of high-order noise. There is some interesting structure (namely the vertical blue line) that exists, but it is unclear where that feature could originate.

error stability after removing common-mode errors of <20 nm RMS. The existence of some sort of common mode between all the extrema points suggests that the image sharpening might be somewhat off. Therefore, the error arising from time variability might be common mode

4.4 Chromaticity of the Grids

All values reported herein are based on the data taken in the Fe II narrow-band filter. However, as the goal of the project is to construct an instrumental aberrations map that is applicable to data taken in all filters, including the K' ($\lambda_0 = 2.124$ μm; $\delta\lambda = 0.351$ μm) and L' ($\lambda_0 = 3.776$ μm, $\delta\lambda = 0.700$ μm) broad-band filters, it is necessary to test to make sure the grid is achromatic at several different wavelengths and that the values reported in table 4.2 hold true at different wavelengths.

In an initial study, we took phase diversity data at several non-thermal narrow- and

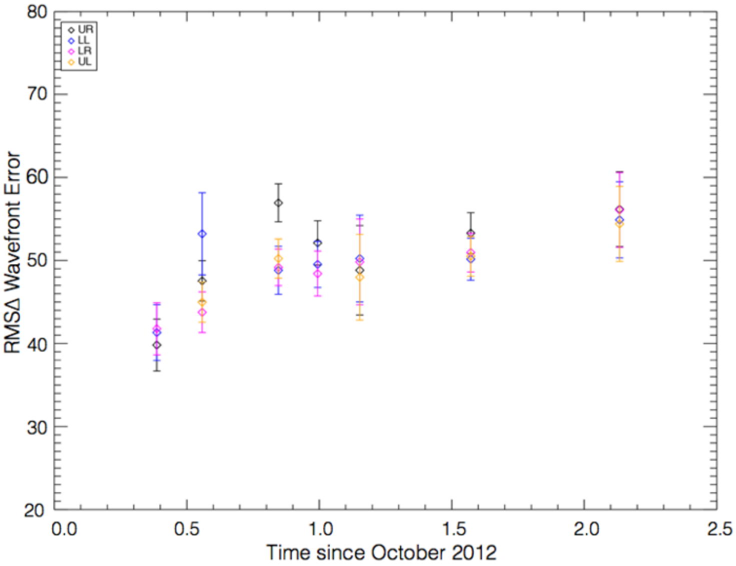

Figure 4.8 Plot of RMS change in the wavefront error as a function of time since our original data acquisition (October 2012). The variability between two given times is consistent with ∼50 nm RMS. This is slightly higher than a factor of $\sqrt{2}$ times our measurement error, implying there might be some time dependent variability. Additional work, such as checking the temperature of the system, needs to be performed..

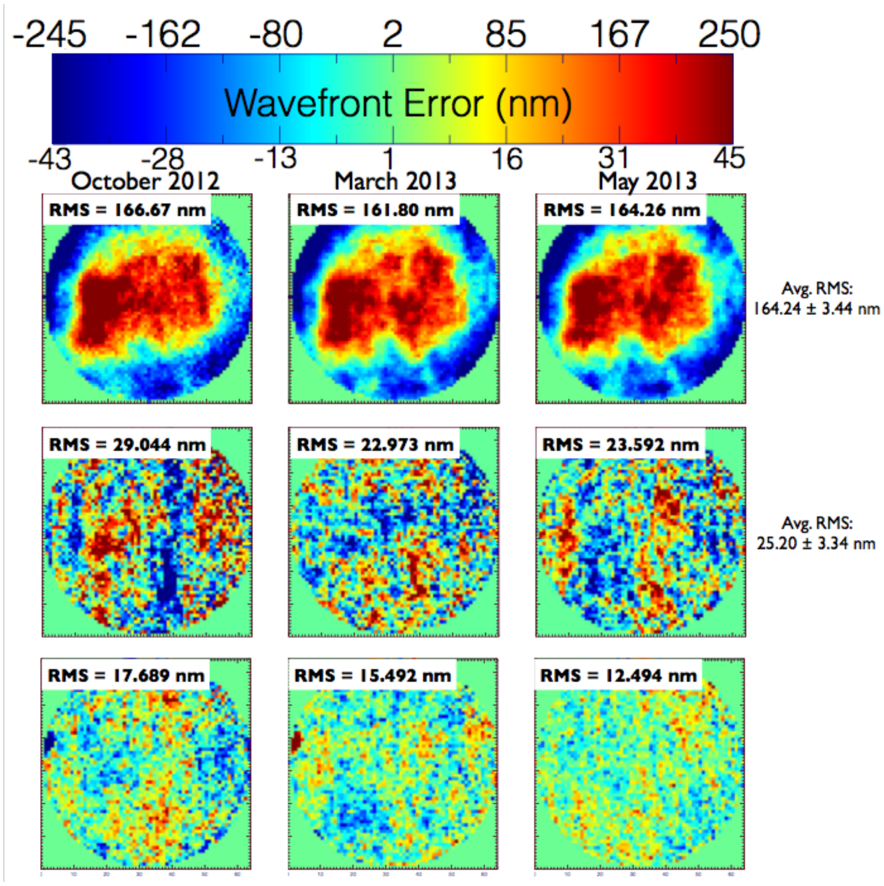

Figure 4.9 There seems to be common-mode error that exists across the different epochs and different field points. The middle row shows the average of the top row subtracted out; the last row shows the average of all extrema data at the respective epoch subtracted out.

Table 4.3. Focus Study Data

Name of Filter	Central Wavelength (μm)	Bandpass (μm)
He 1A	1.0847	0.0182
Pa γ	1.096	0.016
J continuum	1.2132	0.0198
Pa β	1.2903	0.0193
H continuum	1.5804	0.0232
CH_4S	1.5923	0.1247
Fe II	1.6455	0.0256
CH_4L	1.6809	0.1368
He 1B	2.0563	0.0326
Br γ	2.1686	0.0326
K continuum	2.2706	0.0296

medium-band filters available on NIRC2 as described in Table 4.3. We acquired the phase diversity using the method described in Section 4.1. We optimized integration times to obtain <10,000 DN/coadd, as nonlinearity and saturation can affect the quality of the images. The data were taken at the Δz = -2, -4, and -6 mm, as described above.

Assuming that the phase maps extracted from he phase diversity data are linear combinations of the Zernike polynomials, the defocus term for each phase map can be easily extracted. Our preliminary analysis appeared to show some defocus offset (see Figures 4.10 and 4.11). We only take our phase diversity data in negative focus shifts (as opposed to going through focus; e.g. Shields 2012). We currently cannot go in the opposite direction as moving out of focus in the positive direction will hit a limit in stage motion.

We worked with Greg Doppmann at Keck Observatory to take data in various narrow- and medium-band filters where we moved the fiber in and out of focus in both directions positive and negative directions in small intervals. To determine the optimal focus, plot the strehl ratio as a function of focal position of the fiber and fit a Gaussian to the data (see Figure 4.12). The strehl ratios were extracted using Marcos van Dam's strehl ratio code used to calculate strehls at Keck Observatory. Based on this analysis, it doesn't seem like there really is a focal offset as a function of wavelength; instead, the varying defocus term

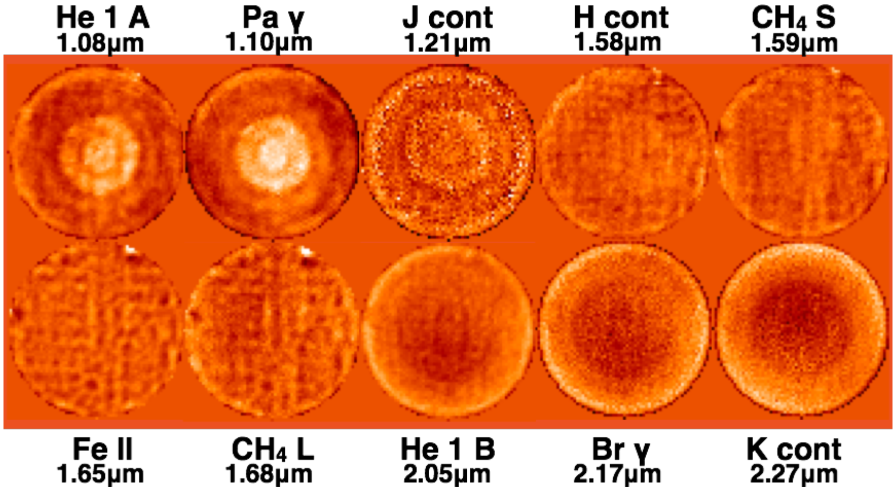

Figure 4.10 Center phase maps extracted from data taken at various narrow- and medium-band filters available on NIRC2. There is a visible apparent focus offset.

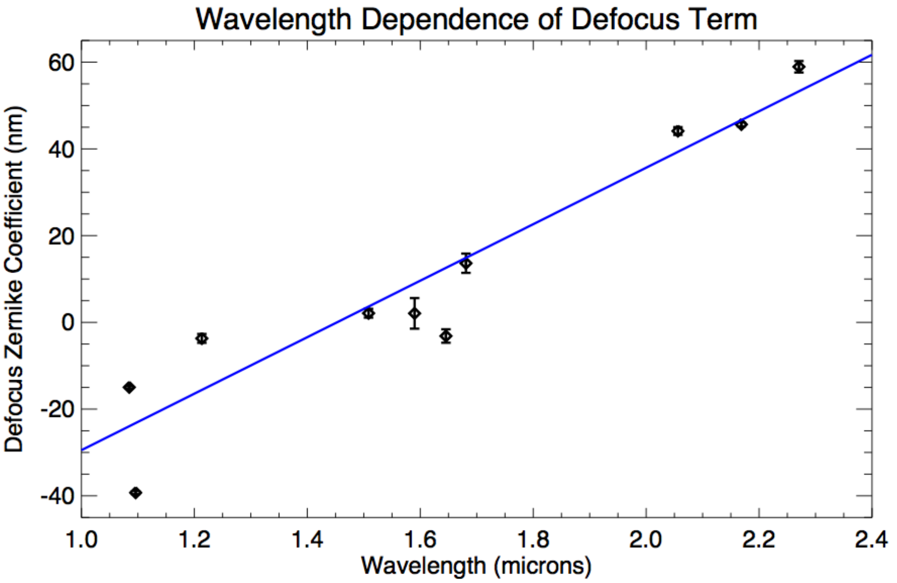

Figure 4.11 A plot of the extracted Zernike coefficient for the defocus mode as a function of wavelength. There is a linear trend between the wavelength and the magnitude of the defocus term.

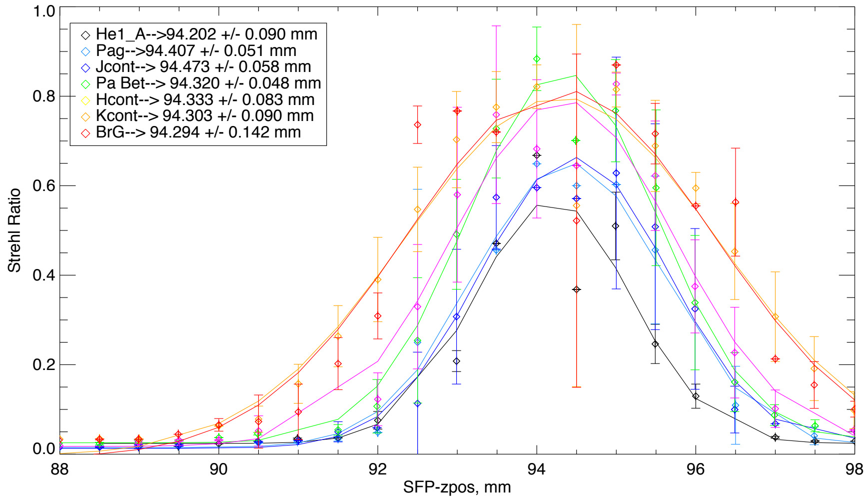

Figure 4.12 Strehl ratio plotted as a function of z-position for a variety of narrow- and medium-band filters. Since all of the Gaussian bell curves have consistent peak positions (as shown in the legend), it does not appear as though there is a focal offset for any of the filters. Each point consists of three images taken in a given band at a given z-position; the plotted point is the average and the associated error bar is the standard deviation of the points.

we obtain in our multi-wavelength data could arise from our method of data collection and the fact that we do not take any positive-out of focus data.

In addition to looking for any focal offset, it is necessary to make sure that any Fe II data we take will be usable at K-band wavelengths. To do a direct comparison of the field extrema at different wavelengths, we took data both in the Fe II narrow-band filter and the Br-γ narrow-band filter, as the Br-γ filter's central wavelength lies within the K' filter that we typically use for Galactic Center observations. Further, taking phase diversity data in the K' filter was not practical for the extrema points as even with the shortest integration times the detector saturated. We were able to subarray down, but that would not cover the extrema points that we needed.

We subtracted out the respective center reference phase maps from the extrema phase maps at for each set of wavelengths. We compared the Br-γ and Fe II optical path differences and decomposed the phase maps into Zernike coefficients, as shown in Figure 4.13. The Br-γ

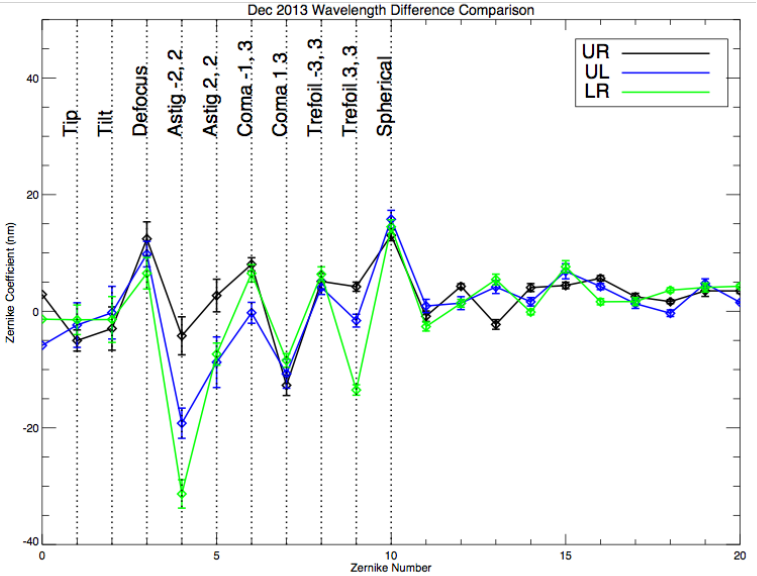

Figure 4.13 Zernike decomposition of the optical path differences between Br γ and Fe II at three of the field extrema. The low-order terms dominate the overall wavefront error, and the differences are low comparable to the overall signal.

and Fe II Zernike terms are comparable to within ~80 nm RMS, which is still small relative to the overall wavefront error present in the grid itself. While we could not obtain similar data at K', we did subarray the view to be 320 × 312 centered around the central pixel. We obtained phase diversity data a the "extrema" of this subarray and decomposed this data into Zernike coefficients after subtracting off the reference phase map (taken at the same place the reference maps were taken in Br-γ and Fe II). Fe II data were also taken at these exact points for comparison, and the Zernike decomposition of this comparison is shown in Figure 4.14. The difference between Fe II and K' is, at most 50.9 nm RMS. It is reasonable that this is much lower than the Fe II to Br-γ comparison, as the data for K' are taken much closer to the reference position than the data at Br-γ.

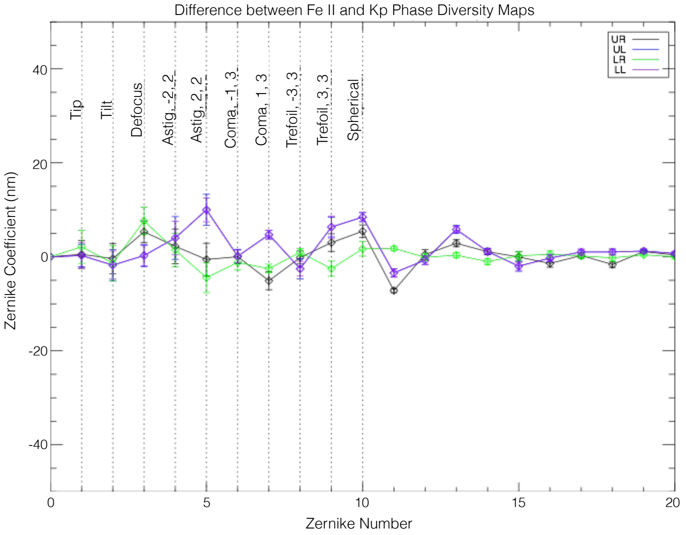

Figure 4.14 Zernike decomposition of the optical path differences between K' and Fe II at positions fairly close to the center of the detector that stayed in the 320 × 312 subarray of the detector. The lower-order terms again dominate the overall wavefront error.

4.5 NIRC2 Optical Realignment: the need for a new grid

Chromatic elongation of the PSF on NIRC2 has been a long-term issue, and it is most problematic at L' due to the large bandpass of the filter ($\lambda_0 = 3.776$ μm; $\Delta\lambda = 0.7$ μm; see KAON 1075), which is also the filter through which a majority of the science data presented Chapters 2 and 3 are taken. The primary cause of this elongation comes from the dispersion of the infrared dichroic, which was installed improperly with the side of maximum thickness rotated by 180° of what was intended (see left panel of Figure 4.15). Additionally, the secondary obscurations as misaligned from the pupil mask, an achromatic effect (see right panel of Figure 4.15).

Both issues were fixed by adjusting two off-axis parabola mirrors (OAPs) as shown in Figure 4.16. The first mirror in the K-mirror setup was also adjusted to minimize pupil nutation to get it within 100 mm on the primary (1% of the pupil), the original Keck requirement. Prior to the adjustment, the pupil nutation was a little over 2%; the minimum Keck requirement was originally 1%. Figure 4.17 shows the L' PSF after these adjustments

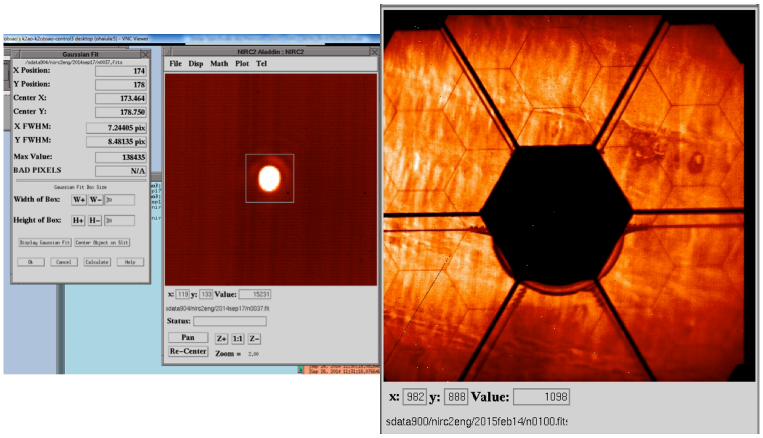

/sdata904/nirc2eng/2014sep17/n0037.fits
X Position: 174
Y Position: 178
Center X: 173.464
Center Y: 178.750
X FWHM: 7.24405 pix
Y FWHM: 8.48135 pix
Max Value: 138435
BAD PIXELS N/A
Width of Box: 30
Height of Box: 30

x: 119 y: 133 Value: 15231
sdata904/nirc2eng/2014sep17/n0037.fit
Status:
Zoom = 2.00

x: 982 y: 888 Value: 1098
sdata900/nirc2eng/2015feb14/n0100.fits

Figure 4.15 *Left:* NIRC2 snapshot showing the elongation of the L' core elongation in the y-direction. The FWHM in y is over 5 pixels (50 mas) longer than the FWHM in the x direction. *Right:* Image of the misaligned pupil before any hardware adjustment. It is evident that the pupil and the obscuration are not coincident with each other.

on the left-hand panel; the right-hand panel shows the secondary obscuration in alignment with the pupil. However, these adjustments cause high levels of astigmatism (∼200 nm) on the deformable mirror when image sharpening.

As there were changes made to the optical path, we acquired phase diversity data prior to the realignment and after the realignment. The comparison is shown in Figure 4.18. Not only are the changes in the RMS wavefront error high (at most 60.50 nm RMS), but there is some apparent structure in the phase maps in the bottom half. There are also random assortments of very bright pixels in the maps themselves (which could be heavily contributing to the high RMS values). While the general structure of the phase maps remain the same (see figure 4.18), there is a slight displacement between the two maps where the December 2014 data are shifted up and down a few pixels compared to the May 2015 data.

In addition, the flux of the fiber decreased compared to the setup outlined in table 4.1. As evident in the comparison in Figure 4.19, it was necessary to increase the exposure times of the data. The left panel of figure 4.18 shows the differences in the data after the fluxes had been adjusted in the extrema points. The new integration times are shown in Table 4.4.

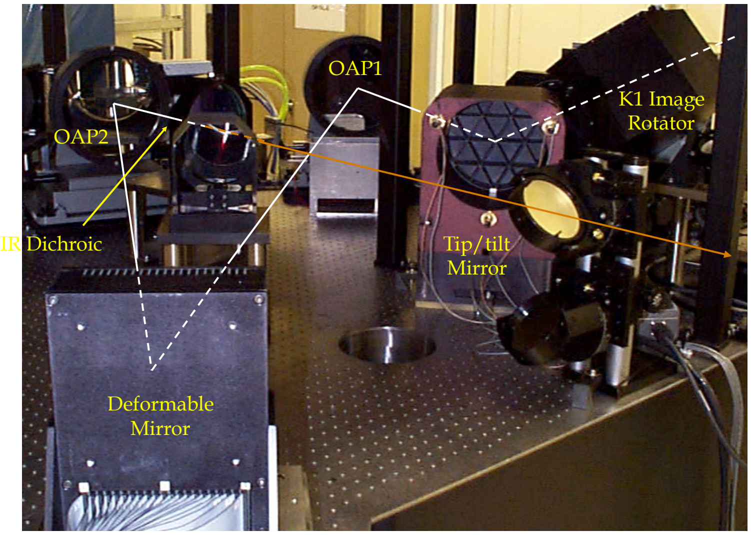

Figure 4.16 Optical bench of Keck I (which is the mirror image of the optical bench of Keck II). Both OAP1 and OAP2 were adjusted in order to decrease the elongation at L' and to adjust the secondary obscuration. The infrared dichroic was also rotated 180°, and the K-mirror was adjusted to minimize pupil nutation.

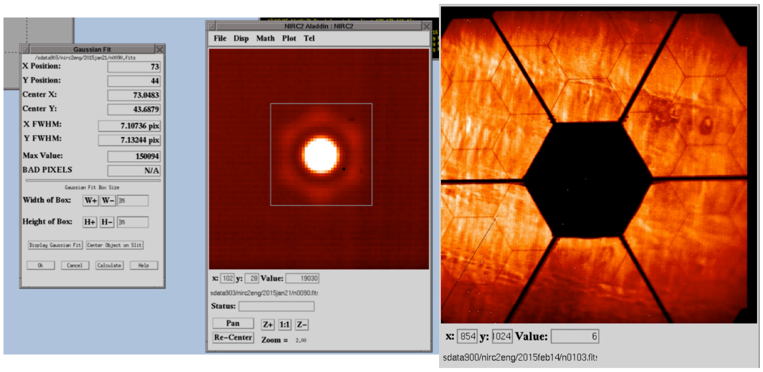

/sdata903/nirc2eng/2015jan21/n0090.fits

X Position: 73

Y Position: 44

Center X: 73.0483

Center Y: 43.6879

X FWHM: 7.10736 pix

Y FWHM: 7.13244 pix

Max Value: 150094

BAD PIXELS N/A

Width of Box: 35

Height of Box: 35

x: 102 y: 28 Value: 19030

sdata903/nirc2eng/2015jan21/n0090.fits

Status:

Zoom = 2.00

x: 854 y: 1024 Value: 6

sdata900/nirc2eng/2015feb14/n0103.fits

Figure 4.17 *Left:* L' image of the lit fiber in the focal plane of NIRC2. After the necessary optical path adjustments, the core is now symmetric in both x and y. *Right:* Secondary obscuration and pupil plane are aligned after making optical path adjustments.

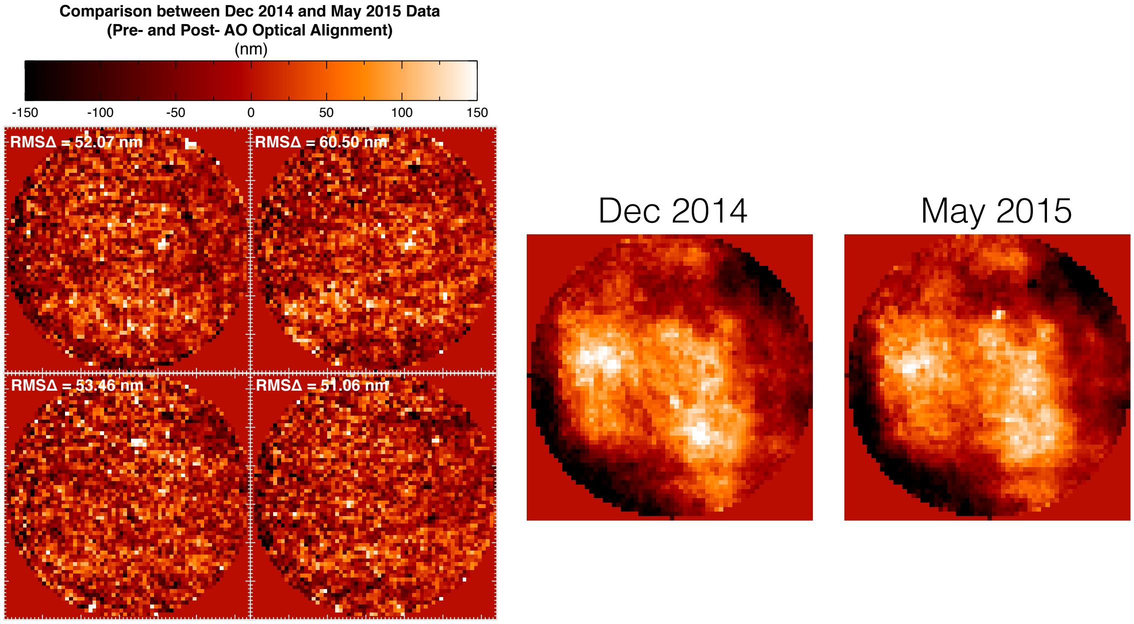

Figure 4.18 *Left:* Comparison of four extrema points between pre- and post-alignment setups. There is a cloudy white band going across the bottom of the difference phase maps, and clumps of bright pixels may contribute to the overall fairly high levels of changes between the two sets of data. The data taken after the alignment were with the adjusted integration times. *Right:* Comparison of lower left maps with pre-(December 2014) and post-(May 2015) alignment setups.

However, the flux of the fiber changes regularly (as within the last two data acquisition runs it is changed significantly), and it is not clear why that is the case. It is therefore necessary to check the total integration times at the beginning of each phase diversity data acquisition run. The individual exposures must not be saturated, as it creates systematic errors and introduces unusual structure to the phase maps.

Table 4.4 Adjusted Integration Times after Optical Alignment

Δz (mm)	t_{int} (sec)	n_{coadds}	n_{reads}
-2	1.15	20	CDS
-4	4.0	8	16
-6	5.75	4	16

4.6 Interpolation Modeling

While we collected two dense grids of phase diversity data and associated phase maps to characterize the instrumental non-common path errors, this is still a discrete sampling and does not give the phase of the aberrations at an arbitrary field point. This is a requirement for our project, as it will be integrated into AIROPA (**A**nisoplanatic and **I**nstrumental **R**econstruction of **O**ff-axis **P**SFs for **AO**), our final software package that combines *StarFinder*, the atmospheric description of the anisoplanatism (both for natural guide stars and laser guide stars), and the instrumental aberrations to account for spatial variation of the PSF.

It was absolutely essential to obtain a virtually continuous model of the instrumental aberrations in order to avoid sudden changes in the behavior of the instrumental PSF. We decomposed each phase map into the Zernike basis, as it is a series of orthogonal, independent terms and interpolated each Zernike term across the field of view of the detector so that we had a continuous description of each Zernike coefficient as a function of position. Before implementing this in the AIROPA package, we needed to check to see if interpolating across the field of view would yield phase maps that were consistent with our measurements, so we

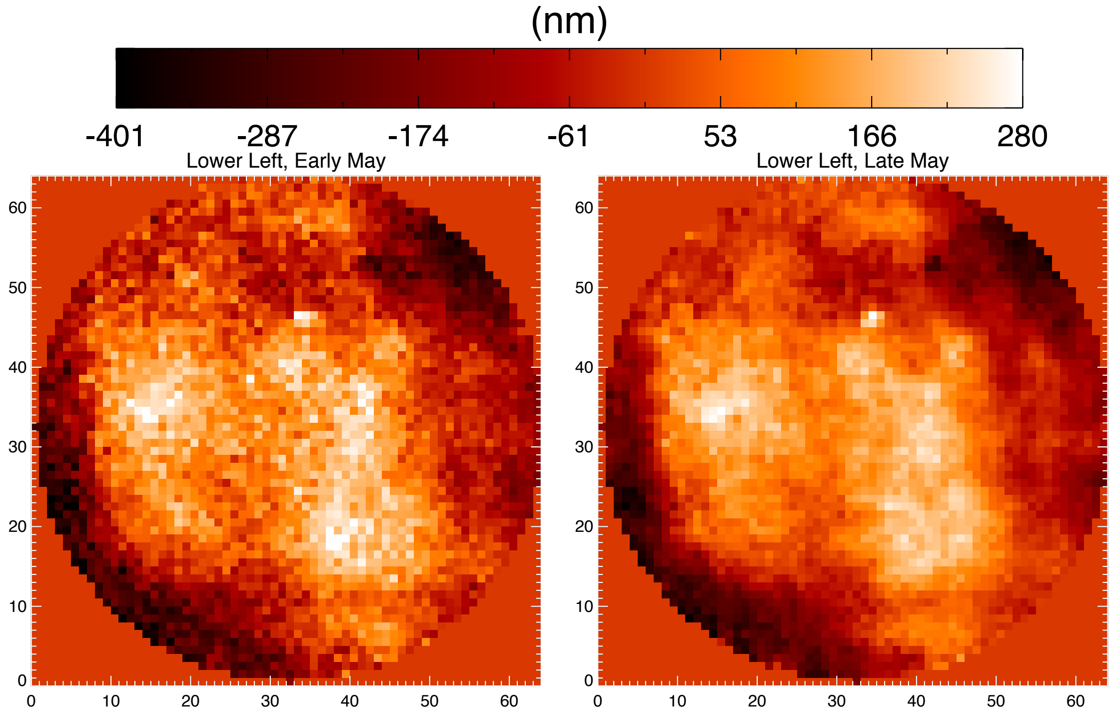

Figure 4.19 Change of the flux of the fiber after the realignment in April of 2015. The left panel shows the data taken using the setup outlined in table 4.1, while the right panel shows an increase in the integration times of the out-of-focus images so that they are closer to 10,000 DN/coadd. The RMSΔ between these two maps is 50.28 nm. The pixel-to-pixel noise variation is clearly evident on the left panel, while the right panel is more continuous and smooth.

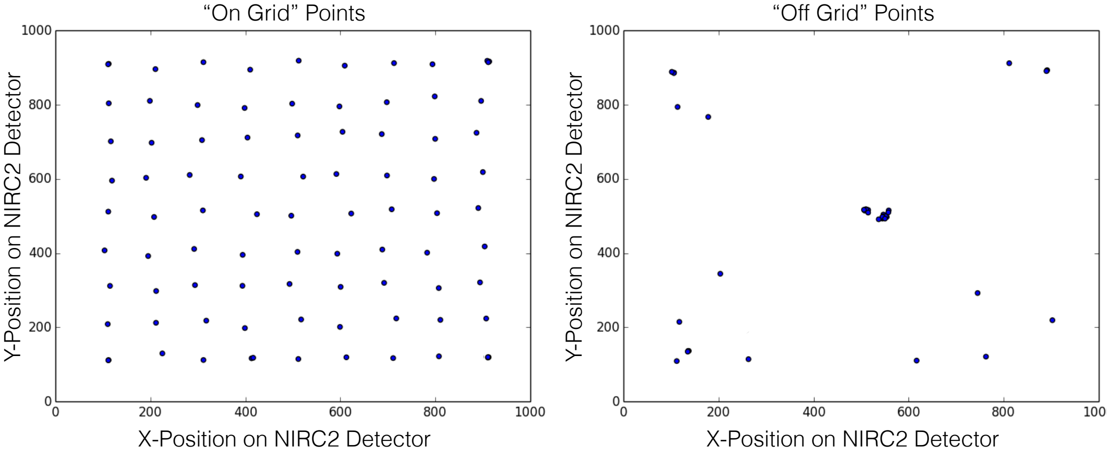

Figure 4.20 *Left*: Positions of the "on-grid" points across the NIRC2 detector. These points are used to establish an interpolation model tested on the "off-grid" points that already have measured phase maps to check the fidelity of the interpolated maps. *Right*: Positions of the "off-gird" points on the NIRC2 detector. These data have measured phase maps, so artificial phase maps were constructed at these positions from our interpolated model to determine if they matched the measured phase maps.

interpolated out to the first 251 individual Zernike terms. This was motivated by plotting the RMS difference between the data and the interpolated model as a function of Zernike radial orders included; the unmodeled power corresponds to ∼30 nm RMS in the extrema (which is roughly on par with our repeatability measurements over the course of one measurement acquisition; see Figure 4.26). We took a series of "on grid" phase maps from our pre-alignment grid that roughly made a 9×9 grid with phase maps spaced ∼100 pixels in x and y (see left panel of Figure 4.20). The goal of this experiment was to determine if constructing a phase map from most of the data (i.e., "on-grid" data) would yield a phase map at any of the "off-grid" points that was consistent with the phase maps measured at those positions.

To construct an interpolated model, we use a third order bivariate spline in x and y. The 2D spline is a function of x and y, which are the detector coordinates, and the spline models the coefficient of a single Zernike coefficient across the detector. We did a similar analysis using the nearest neighbor approach, where Zernike coefficients were taken from the nearest Zernike phase map, but that does cause some discontinuity between the coefficients, particularly if the position in question lies on the edge between two phase maps. The difference between the spline interpolated model and the measured Zernike coefficients of the "off-grid" positions are shown in Figure 4.21. It is evident that the difference between the model and the data is very small overall (∼40 nm RMS difference at most in the 251-term Zernike coefficient decomposition; see Figure 4.22). This modeling difference is very small compared to the 190 nm corner-to-edge wavefront error difference measured in the pre-alignment grid; therefore, it is better to use the Zernike interpolated model to reconstruct the phase maps than to not correct for spatial variation of the instrumental point spread function at all.

As discussed above, a nearest neighbor interpolation was applied to the "off-grid" maps to compare to the third order bivariate spline to see if that model was more accurate in reconstructing the measured phase map at the "off-grid" points. Our analysis is shown in Figure 4.23. While the two models have comparable accuracy in reconstructing the phase maps, the third order bivariate spline model did marginally better than the nearest neighbor model, as the average difference between the reconstructed map and modeled map for the spline model was 33.6 nm RMS, while the average difference of the nearest neighbor reconstruction and measured map was 35.2 nm RMS.

We performed a similar analysis for the post-alignment grid. To test a model on previously-acquired phase maps, we constructed our model from similar "on grid" locations depicted in Figure 4.20, but had many more "off-grid" positions in our post-alignment grid. The breakdown of the difference between the model and extracted Zernike coefficients from our measured phase maps is depicted in Figure 4.24 and is similar in behavior to the pre-alignment decomposition depicted in Figure 4.21. The total RMS of the difference between the modeled phase maps and the measured phase maps for the post-alignment grid is shown in Figure 4.25.

For our description of the instrumental PSF, we wanted to increase the Zernike radial order out to which we interpolated in order to decrease the overall wavefront error. Therefore, we generated a model using all available data (both the "on-grid" and "off-grid" data) and

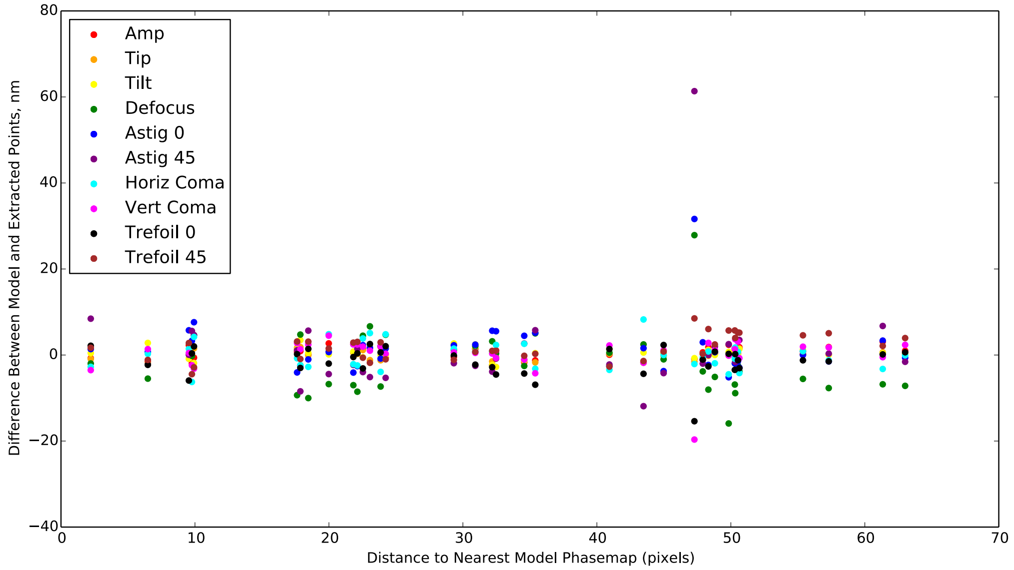

Figure 4.21 RMS difference between the bivariate spline interpolated model at the “off-grid” points and the measured phase maps as a function of distance to the nearest phase map included in the model (as shown in Figure 4.20) broken down by Zernike coefficient. Only the lower-order terms are shown to see if there is significant power in these terms, as those modes contribute more to the overall power in each map than the high-order terms. The difference between the low-order terms is small, and there is only one position which has a large overall error.

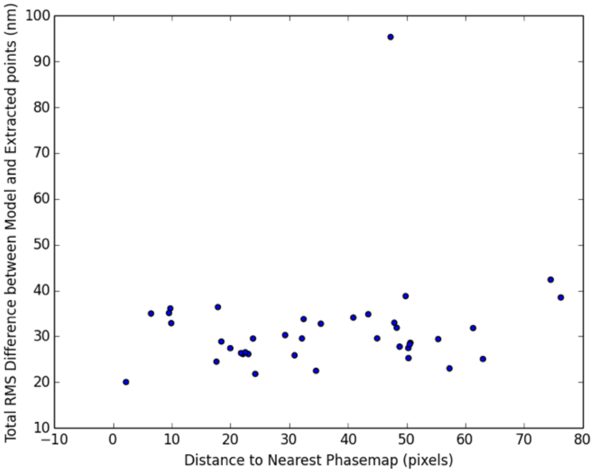

Figure 4.22 Total RMS difference between the bivariate spline interpolated model at the "off-grid" points and the measured phase maps as a function of distance to the nearest phase map included in the model. This is very similar to Figure 4.21, except added in quadrature over each position and across all 251 Zernike terms.

generated grids where a phase map was computed every 5 pixels in x and y (see below). We extracted the model maps that are spatially nearest to the corner positions and compared both the visible structures present in the maps and the RMS of the differences. Both of these are shown in Figure 4.26. After the 21st radial order, which consists of 251 Zernike coefficients, strange structures start appearing in the reconstructed maps, and the RMS values start increasing again. The 349-actuator deformable mirror on Keck is expected to be Nyquist-sampled at ∼247 Zernike coefficients, which is in the same (21st) radial order. We therefore generate our model with the first 21 radial orders.

Our current tests show that our Zernike extraction, which consists of taking a dot product of the Zernike polynomials to our observed phase maps, does not always agree very well with our interpolation. Figure 4.27 shows a plot of the difference between our extracted mode and our extracted Zernike mode; as is evident from Figure 4.28. Some of our modes clearly have sudden changes across the field of view, which may be why neither our linear nor cubic interpolation schemes are recovering the extracted Zernikes.

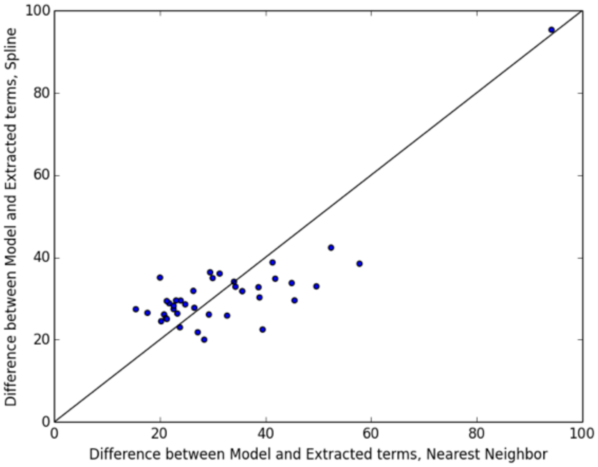

Figure 4.23 Comparison of the difference between the third order bivariate spline model and the nearest neighbor model compared to the measured phase maps. A 1:1 line is also overplotted; points above the line favor the nearest neighbor model, while points below the line favor the spline model. The average difference between the model and extracted points for the spline is 33.6 nm RMS, while the average difference between the model and extracted terms for the nearest neighbor model is 35.2 nm RMS.

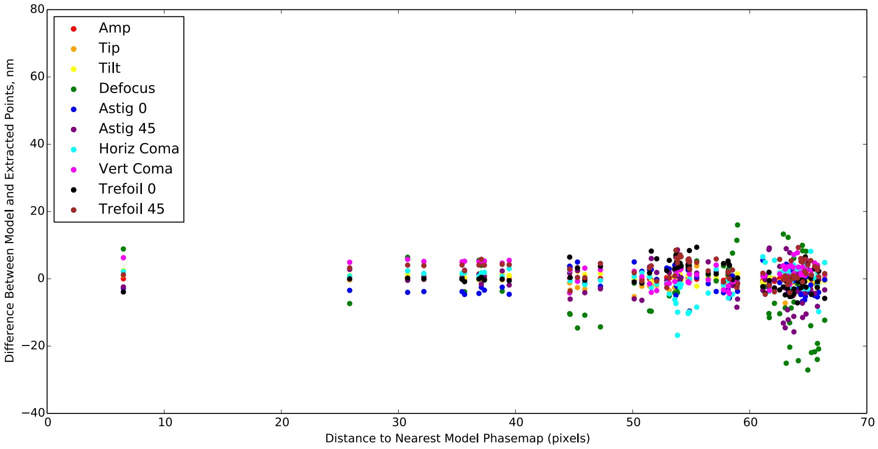

Figure 4.24 RMS difference between the bivariate spline interpolated model at the "off-grid" points and the measured phase maps as a function of distance to the nearest phase map included in the model broken down by Zernike coefficient. The difference between the low-order terms is small, and there is only one position which has a large overall error. This figure is similar to Figure 4.21, but is for the post-alignment grid.

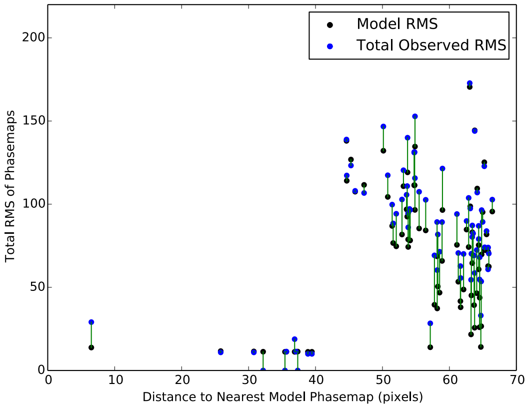

Figure 4.25 Total RMS of phase maps plotted as a function for distance to the nearest phase map for the "off-grid" points in the post-alignment grid. This figure is similar to figure 4.22 for the pre-alignment grid. The blue points show the total RMS of the measured phase maps, while the black points shown the total RMS of the model; the green lines connect data points for the same field position.

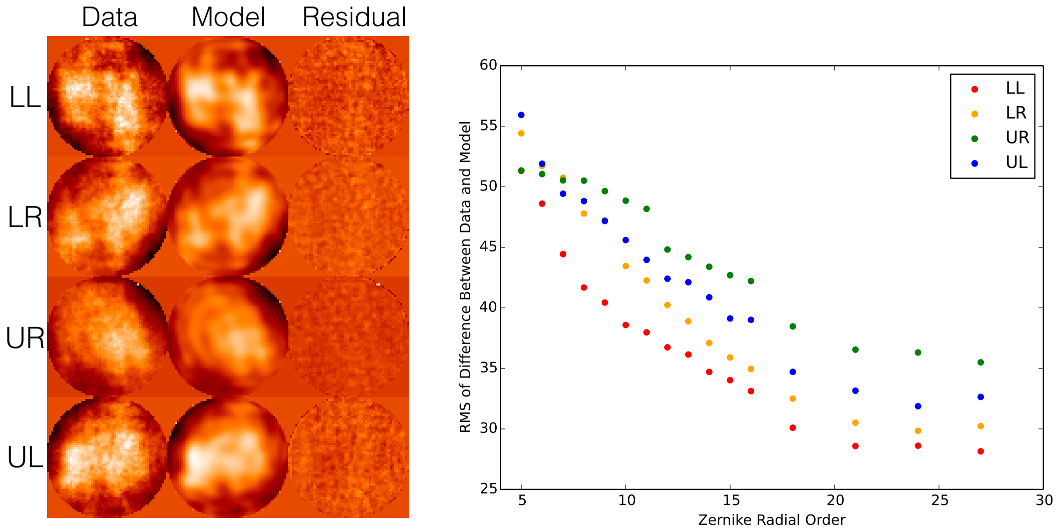

Figure 4.26 *Left:* Difference between our observed phase maps at the extrema points (UR = Upper Right, UL = Upper Left, LL = Lower Left, LR = Lower Right) compared to the reconstructed phase maps from 21 radial orders. The residuals are very minimal and consist just of pixel-to-pixel noise. *Right*: Plot of RMS of the difference between the data and the reconstructed phase maps as a function of radial order used in the reconstruction. After 21st radial order, noise is added to the phase maps, which is why we decided to stop at the 21st order. Each point signifies that if anything after the order on the x-axis is not included, the amount of noise on the y-axis will be present.

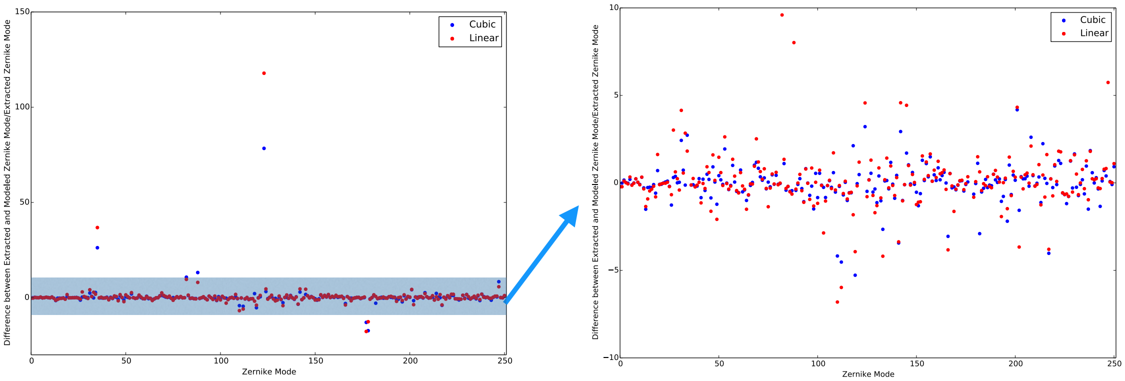

Figure 4.27 *Left*: Plot of the difference between extracted and modeled Zernike coefficients normalized by the extracted Zernike mode. If the value is around 0, the mode has been recovered well. *Right*: Same as left, but zoomed into the blue shaded region on the left. It isn't clear if linear or cubic bivariate spline interpolation is better.

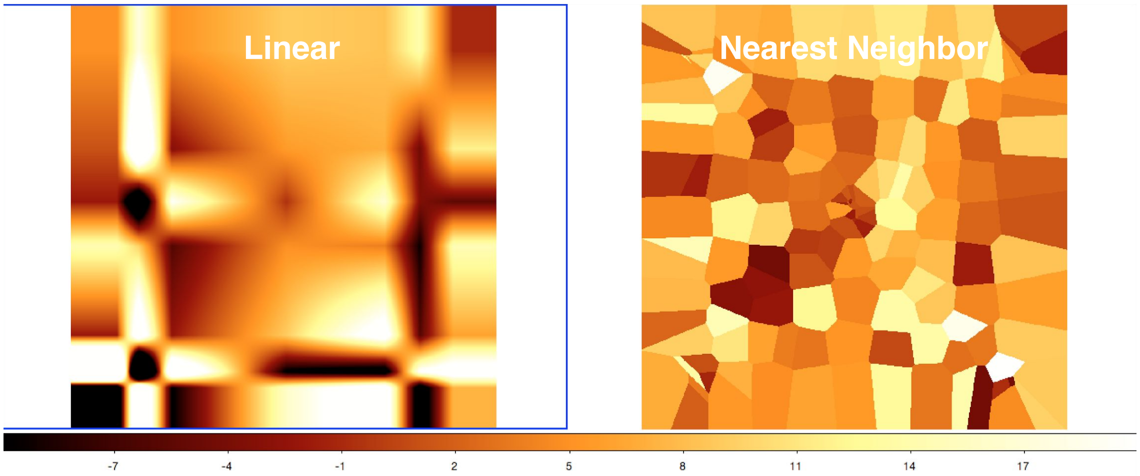

Figure 4.28 *Left*: Linear Bivariate Spline interpolated forty-first Zernike Mode. *Right*: The same as left, but with a nearest neighbor interpolation. It is evident that there are clear, very fast changes across the field of view of the interpolation.

4.7 Dissemination

We have created two grids of phase diversity data–one with all Fe II data taken prior to the NIRC2 alignment, and one with all Fe II data taken after the NIRC2 alignment. The time variability of this grid is small compared to overall extrema measurements, both before and after the alignment, and potential errors, such as sampling and time variability, are small. We have used this phase diversity data to generate an interpolated, continuous model to describe the non-common path aberrations internal to our instrumentation contributing to spatial variation of the point spread function and have demonstrated that the model reconstructs the phase maps on a level where the differences between what we measure and what we reconstruct are small.

With this interpolated model, we have constructed a grid of phase maps constructed every 5 pixels in x and y that are described by 21 radial orders of Zernike terms. This has been delivered to the AIROPA team, as has all the data. The phase diversity pipeline to reduce any acquired phase diversity data has also been put into a repository, documented, and delivered to the AIROPA team. The phase map data will become available to the public once AIROPA is released.

4.8 On-Sky Tests

We have set up some tests with large-separation binary stars to validate the accuracy of the instrumental PSF reconstruction. To do this, we took a series of data at W. M. Keck Observatory where atmospheric conditions were favorable (seeing = blah) and the isoplanatic angle was large so that spatial variation of the point spread function was clearly dominated by the instrumental contribution.

4.9 OSIRIS Phase Diversity Data: Predicting Integral Field Spectrograph PSFs with Imager PSFs

The OSIRIS (**O**H-**S**uppressing **I**nfra**R**ed **I**maging **S**pectrograph) integral field spectrograph (IFS) (Larkin et al., 2006) is a valuable scientific instrument in that every spatial pixel (short: spaxel) has an associated spectrum. In a crowded field like the Galactic Center where it would be difficult to differentiate the spectra of several stars along a slit, it is a powerful tool that has been used to determine the spectral type of stars (e.g., Do et al. 2009a, Bartko et al. 2009b), refine orbital fitting with the additional of radial velocity data (e.g., Ghez et al. 2008, Gillessen et al. 2009, Yelda et al. 2014), and determine the metallicities of stars at the GC (Do et al., 2015). However, the PSF of the OSIRIS spectrograph is not well-determined. When *StarFinder* (see Section 2.3.1.1) is run on OSIRIS images, a PSF is determined by averaging over a few bright stars in the vicinity. Similarly to NIRC2, there is spatial variability across the field of view for OSIRIS that has not been taken into account.

OSIRIS also has an imager mode that will be upgraded in late 2016/early 2017 (see Larkin et al. 2006 for information about the imager mode and Fitzgerald et al. 2016 for information regarding the upgrade). The imager is a cryogenically cooled instrument on the same optical bench as the IFS that has a 20 mas/pixel plate scale. As it has a significantly larger field of view ($20\farcs4$ arcsec × $20\farcs4$ arcsec) than the spectrograph (at most $4\farcs8 \times 6\farcs4$ but is highly dependent on the filter and plate scale selected) and is offset by $19\farcs4$ from the pointing of the spectrograph, one of the original motivations for having the imager was to monitor changes in the PSF over the course of the night (OSIRIS manual). However, due to high background levels, the original OSIRIS imager was most effective at H-band, so the Hn3 narrow-band filter has historically been used for the image sharpening procedure ($\lambda_0 = 1.635$ μm, $\Delta\lambda = 0.088$ μm; OSIRIS manual). This has been run prior to any adaptive optics OSIRIS IFS or imager run, as there was at least a few percent increase in the Strehl ratio when the image sharpening procedure was run on the OSIRIS imager (J. Lyke, private communication). Out-of-focus images are taken at Δz positions of +2.5, −2.5, and −5 mm from the in-focus position and run through the a modified Gerchberg-Saxton algorithm

Table 4.5. Data Characteristics for Image Sharpening

Instrument	Band	Plate scale (mas/pixel)	Pupil Size
NIRC2	Fe II	0.010	11.14
OSIRIS Imager	Hn3	0.02034	10.94
OSIRIS Spectrograph	Kn3	0.035	11.30

to extract the phase map at a given position (Atcheson et al., 2003). To determine the field variation of the OSIRS imager, J. Lyke and I took a 5 × 5 grid spanning the central ∼900 pixels. The reference phase map, in this case taken at the center of the detector, was subtracted out from all other maps to create optical path differences. Prior phase map retrieval shows that there is at least 90 nm RMS variation between the reference position phase maps and the corners. Therefore, instrumental variations need to be characterized on the imager as well. Our initial grid of phase maps are shown in Figure 4.29.

Image sharpening has only somewhat been developed on the OSIRIS spectrograph mode (J. Lyke and J. Larkin, private communication). Since the spectrograph is an IFU, a different procedure is necessary to extract phase diversity information than what is typically used on the imager. Image sharpening is performed on the imager, and the fiber source is centered on the spectrograph where the Kn3 filter and a 20 mas/pixel plate scale is used. The fiber source is set to a 1% transmission using a series of ND filters in front of the illuminated fiber. The 2D data are reduced into 3D data cubes and processed by subtracting off a background and dividing by a normalized flat field, and the cubes are collapsed into a 2D image (averaging along the wavelength axis). As this process is under development, we have been taking the data at $\Delta z = +2$, -2, and -4 mm from the in-focus position just to make sure the image sharpening routine works on the data. There are some variations between the imager, spectrograph, and NIRC2; namely, the plate scales and the pupil sizes need to be adjusted. These are shown in the table below. Figure 4.30 shows a phase map taken from out-of-focus data on the spectrograph after image sharpening had been performed on the imager.

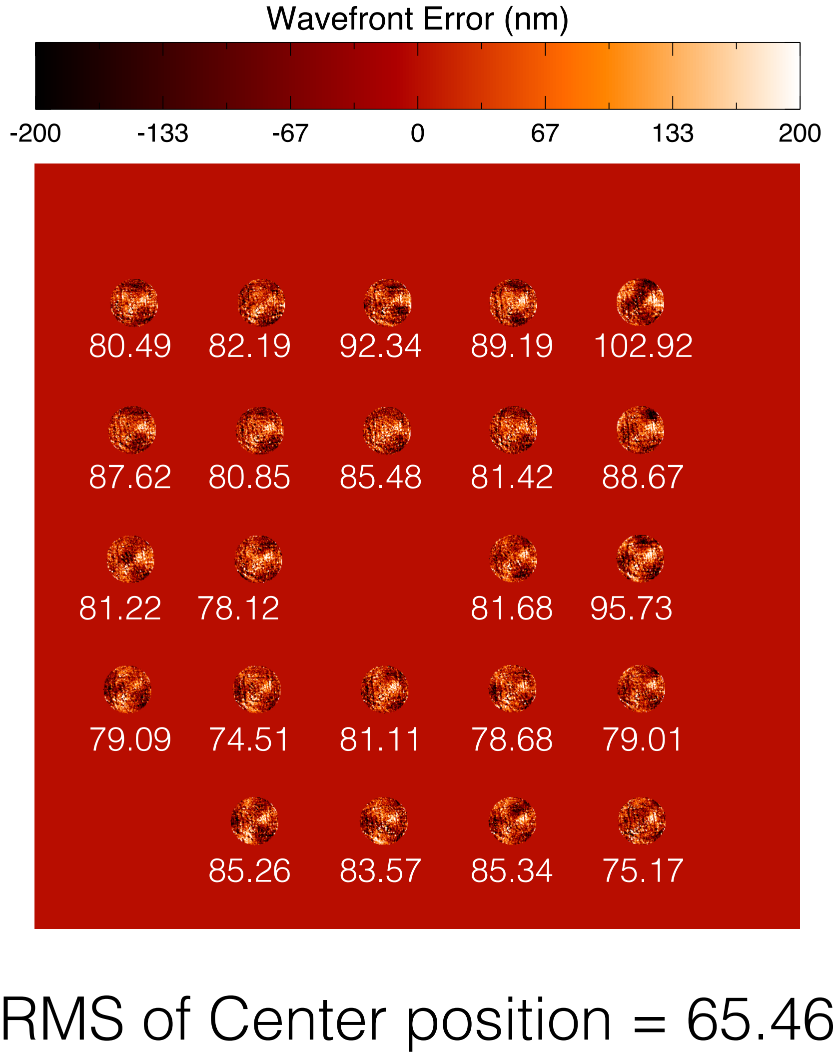

Figure 4.29 Our first OSIRIS imager phase diversity grid. The center map was subtracted, and the white numbers indicate the RMS of the difference between a phase map taken at a given field position and at the center position in nanometers. The phase maps have a significant amount of structured error, something that is currently being looked into with J. Lyke at Keck Observatory.

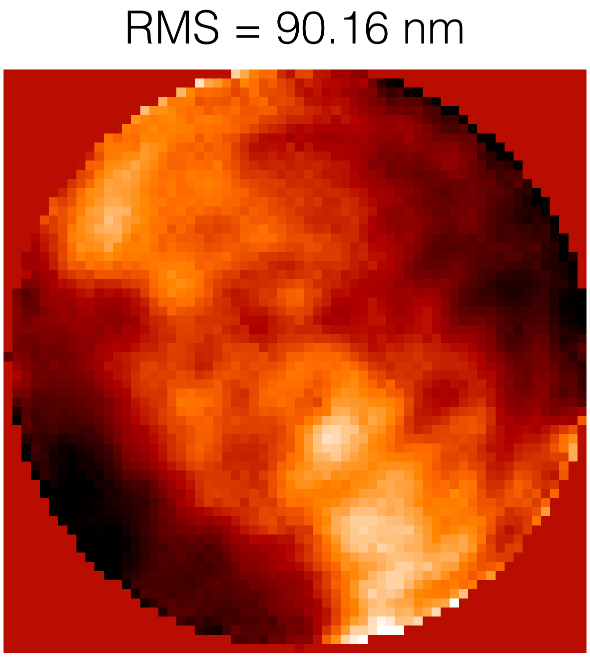

Figure 4.30 Phase diversity map derived from out-of-focus data taken on the OSIRIS Integral Field Spectrograph. Image sharpening was first performed on the imager, then data was taken on the spectrograph. There is very clearly astigmatism left over from the image sharpening procedure on the imager, suggesting it might be beneficial to image sharpen on the spectrograph. Future additional measurements will explore whether an additional astigmatism term could be applied on the spectrograph when image sharpening is done on the OSIRIS imager to obtain a sharpened PSF.

CHAPTER 5

Conclusions

This thesis characterizes several infrared excess sources found in the Galactic Center. These sources are very interesting because they: (1) are very cold and intrinsically large sources that exist in a chaotic environment; (2) interact with Sgr A* directly (in the case of G1 and G2); (3) this might be a new class of sources found at the heart of our Galaxy; (4) these objects may have originated from the young stars, but not all come from the young stellar disk.

G1 is very similar to G2–it lies a highly eccentric orbit and recently passed through periapse passage (2001.3), but unlike G2, its observations have only been performed after periapse passage. These observations paint a very interesting picture: G1 shows clear size evolution as a function of time, and its L' flux also decreases by nearly a factor of 5 during the 10 years of observation. It lies on a similar orbital plane to G2, but follows a different trajectory than G2. G1's continued survival 14 years after periapse, along with its compactness in epochs further from the time of periapse, suggests that this source is stellar in nature and may be consistent with a black-hole driven binary merger product.

We present an orbital analysis of another source, G3, which has nearly identical observational properties to G1 but lies further away from Sgr A* and does not have nearly as large as a tidal interaction with the black hole. G3 does not lie on a similar orbital plane to G1 or G2 at all, suggesting that these objects do not necessarily all come from the same region in the sky. G3 is also resolved at L', similarly to G1, suggesting that it likely has an optically thin shell surrounding a gas envelope, which is external to an optically thick dust shell and compact stellar object. That is, G3 likely follows a similar model to what we adopt for G1 in Chapter 2.

Our infrared excess sources consist of cold, sometimes resolved, objects. Many of them have Br-γ emission, suggesting that they have gas envelopes that are being externally ionized by the radiation field from the Galactic Center; some of of these also have collisionally-ionized [Fe III] emission that may stem from interaction with very high levels of radiation, like that coming from the fast wind with whatever formed the mini-cavity reason (Lutz et al., 1993) or perhaps the nearby IRS 13 region.

The members of our sample are preferentially located south of Sgr A*, but there are some sources to the north that are morphologically interesting. For instance, G15 is an extremely red, very extended object that has a triangle-shape. We speculate that it could perhaps be a bow-shock source interacting with IRS 16C, but modeling of that is beyond the scope of this thesis.

Proper motion measurements of our sample are consistent with those in Eckart et al. (2013). Using the astrometry and radial velocity data for several of our sources, we were able to determine the orientation of their orbital planes to see if they are either consistent with the clockwise disk of young stars or G1 and G2. We found that there is no preferential direction for the orientation of their orbital planes, but these sources could still come from the young stars, as $\sim$80% of young stars are off the clockwise disk.

All of our data are affected by anisoplanatism, which is a major contribution to our astrometric errors. The last chapter of this thesis describes a way to correct for instrumental non-common path aberrations through the use of phase diversity data. This methodology was shown to be applicable to both narrow-band data and broadband data with an acceptable error. This is currently being incorporated into the AIROPA software package, which also incorporates the atmospheric response to the AO system's anisoplanatism. This will be applied to all Galactic Center data taken at all wavelengths in the next few years, and it is already being applied to cluster data for the derivation of a field-dependent PSF distortion solution by collaborators at the Institute for Astronomy at the University of Hawaii.

BIBLIOGRAPHY

Aharonian, F., Akhperjanian, A. G., Aye, K.-M., et al. 2004, A&A, 425, L13

Ajello, M., Albert, A., Atwood, W. B., et al. 2016, ApJ, 819, 44

Allen, D. A., Hyland, A. R., & Hillier, D. J. 1990, MNRAS, 244, 706

Anninos, P., Fragile, P. C., Wilson, J., & Murray, S. D. 2012, ApJ, 759, 132

Antonini, F. 2014, ApJ, 794, 106

Archer, A., Barnacka, A., Beilicke, M., et al. 2014, ApJ, 790, 149

Atcheson, P. D., Acton, S., & Lightsey, P. A. 2003, in Proceedings of SPIE, Vol. 4839, Adaptive Optical System Technologies II, ed. P. L. Wizinowich & D. Bonaccini, 228–239

Baganoff, F. K., Bautz, M. W., Brandt, W. N., et al. 2001, Nature, 413, 45

Bahcall, J. N., & Wolf, R. A. 1976, ApJ, 209, 214

—. 1977, ApJ, 216, 883

Ballone, A., Schartmann, M., Burkert, A., et al. 2013, ApJ, 776, 13

Bartko, H., Martins, F., Fritz, T. K., et al. 2009a, ApJ, 697, 1741

—. 2009b, ApJ, 697, 1741

Bautista, M. A., & Pradhan, A. K. 1998, ApJ, 492, 650

Boehle, A., Ghez, A. M., & et al. 2016, Under Review

Britton, M. C. 2006, PASP, 118, 885

Buchholz, R. M., Schödel, R., & Eckart, A. 2009, Astronomy and Astrophysics, 499, 483

Burkert, A., Schartmann, M., Alig, C., et al. 2012, ApJ, 750, 58

Clénet, Y., Rouan, D., Gratadour, D., et al. 2005, Astronomy and Astrophysics, 439, L9

Clénet, Y., Rouan, D., Gendron, E., et al. 2004, Astronomy and Astrophysics, 417, L15

Dale, J. E., Davies, M. B., Church, R. P., & Freitag, M. 2009, MNRAS, 393, 1016

Diolaiti, E., Bendinelli, O., Bonaccini, D., et al. 2000, Astronomy and Astrophysicss, 147, 335

Do, T., Ghez, A. M., Morris, M. R., et al. 2009a, ApJ, 703, 1323

—. 2009b, ApJ, 691, 1021

Do, T., Kerzendorf, W., Winsor, N., et al. 2015, ApJ, 809, 143

Do, T., Lu, J. R., Ghez, A. M., et al. 2013a, ApJ, 764, 154

Do, T., Martinez, G. D., Yelda, S., et al. 2013b, ApJl, 779, L6

Draine, B. T. 2003, Annual Review of Astron and Astrophys, 41, 241

Duchêne, G., & Kraus, A. 2013, Annual Review of Astron and Astrophys, 51, 269

Eckart, A., & Genzel, R. 1996, Nature, 383, 415

—. 1997, MNRAS, 284, 576

Eckart, A., Genzel, R., Krabbe, A., et al. 1992, Nature, 355, 526

Eckart, A., Baganoff, F. K., Schödel, R., et al. 2006, Astronomy and Astrophysics, 450, 535

Eckart, A., Mužić, K., Yazici, S., et al. 2013, Astronomy and Astrophysics, 551, A18

Eisenhauer, F., Schödel, R., Genzel, R., et al. 2003, ApJl, 597, L121

Eisenhauer, F., Genzel, R., Alexander, T., et al. 2005, ApJ, 628, 246

Fitzgerald, M. P., Witzel, G., Britton, M. C., et al. 2012, in Society of Photo-Optical Instrumentation Engineers (SPIE) Conference Series, Vol. 8447, Society of Photo-Optical Instrumentation Engineers (SPIE) Conference Series, 24

Fitzgerald, M. P., Aliado, T., Arriaga, P., et al. 2016, in Society of Photo-Optical Instrumentation Engineers (SPIE) Conference Series

Gao, J., Li, A., & Jiang, B. W. 2013, Earth, Planets, and Space, 65, 1127

Gautam, A. K., Ghez, A. M., & et al. 2016, in preparation

Geballe, T. R., Rigaut, F., Roy, J.-R., & Draine, B. T. 2004, ApJ, 602, 770

Genzel, R., Eisenhauer, F., & Gillessen, S. 2010, Reviews of Modern Physics, 82, 3121

Genzel, R., Thatte, N., Krabbe, A., Kroker, H., & Tacconi-Garman, L. E. 1996, ApJ, 472, 153

Genzel, R., Schödel, R., Ott, T., et al. 2003, ApJ, 594, 812

Gerhard, O. 2001, ApJl, 546, L39

Ghez, A. M., Klein, B. L., Morris, M., & Becklin, E. E. 1998, ApJ, 509, 678

Ghez, A. M., Morris, M., Becklin, E. E., Tanner, A., & Kremenek, T. 2000, Nature, 407, 349

Ghez, A. M., Salim, S., Hornstein, S. D., et al. 2005a, ApJ, 620, 744

Ghez, A. M., Duchêne, G., Matthews, K., et al. 2003, ApJl, 586, L127

Ghez, A. M., Wright, S. A., Matthews, K., et al. 2004, ApJl, 601, L159

Ghez, A. M., Hornstein, S. D., Lu, J. R., et al. 2005b, ApJ, 635, 1087

Ghez, A. M., Salim, S., Weinberg, N. N., et al. 2008, ApJ, 689, 1044

Gillessen, S., Eisenhauer, F., Trippe, S., et al. 2009, ApJ, 692, 1075

Gillessen, S., Genzel, R., Fritz, T. K., et al. 2012, Nature, 481, 51

—. 2013a, ApJ, 763, 78

—. 2013b, ApJ, 774, 44

Haggard, D., Baganoff, F. K., Ponti, G., et al. 2014, in AAS/High Energy Astrophysics Division, Vol. 14, AAS/High Energy Astrophysics Division, 100.04

Hansen, B. M. S., Kalogera, V., & Rasio, F. A. 2003, ApJ, 586, 1364

Hornstein, S. D., Matthews, K., Ghez, A. M., et al. 2007, ApJ, 667, 900

Hurley, J. R., Pols, O. R., & Tout, C. A. 2000, MNRAS, 315, 543

Jolissaint, L., Ragland, S., Wizinowich, P., & Bouxin, A. 2014, in , 91484S–91484S–9

Kim, S. S., & Morris, M. 2003, ApJ, 597, 312

Kozai, Y. 1962, Astrophysical Journal, 67, 591

Kunneriath, D., Eckart, A., Vogel, S. N., et al. 2012, Astronomy and Astrophysics, 538, A127

Larkin, J., Barczys, M., Krabbe, A., et al. 2006, in Society of Photo-Optical Instrumentation Engineers (SPIE) Conference Series, Vol. 6269, Society of Photo-Optical Instrumentation Engineers (SPIE) Conference Series

Lau, R. M., Herter, T. L., Morris, M. R., Becklin, E. E., & Adams, J. D. 2013, ApJ, 775, 37

Lau, R. M., Herter, T. L., Morris, M. R., Li, Z., & Adams, J. D. 2015, Science, 348, 413

Levin, Y., & Beloborodov, A. M. 2003, ApJl, 590, L33

Lidov, M. L. 1962, Planetary Space Science, 9, 719

Lu, J. R., Do, T., Ghez, A. M., et al. 2013, ApJ, 764, 155

Lu, J. R., Ghez, A. M., Hornstein, S. D., et al. 2009, ApJ, 690, 1463

Lutz, D., Krabbe, A., & Genzel, R. 1993, ApJ, 418, 244

Madigan, A.-M., Hopman, C., & Levin, Y. 2011, ApJ, 738, 99

Madigan, A.-M., McCourt, M., & O'Leary, R. 2016, ArXiv e-prints, arXiv:1602.02760

Madigan, A.-M., Pfuhl, O., Levin, Y., et al. 2014, ApJ, 784, 23

McCourt, M., & Madigan, A.-M. 2015, ArXiv e-prints, arXiv:1503.04801

Merritt, D., Alexander, T., Mikkola, S., & Will, C. M. 2010, Review D, 81, 062002

Meyer, L., Witzel, G., Longstaff, F. A., & Ghez, A. M. 2014, ApJ, 791, 24

Meyer, L., Ghez, A. M., Schödel, R., et al. 2012, Science, 338, 84

Meyer, L., Ghez, A. M., Witzel, G., et al. 2013, ArXiv e-prints, arXiv:1312.1715

Miralda-Escudé, J. 2012, ApJ, 756, 86

Morris, M. 1993, ApJ, 408, 496

Morsony, B., Gracey, B., Workman, J., & Yoon, D. 2015, ArXiv e-prints, arXiv:1508.00384

Murray-Clay, R. A., & Loeb, A. 2012, Nature Communications, 3, arXiv:1112.4822

Mužić, K., Eckart, A., Schödel, R., et al. 2010, Astronomy and Astrophysics, 521, A13

Najarro, F., Krabbe, A., Genzel, R., et al. 1997, Astronomy and Astrophysics, 325, 700

Nakano, S., Nishiyama, K., Kabashima, F., et al. 2008, IAU Cirulars, 8972

Naoz, S. 2016, ArXiv e-prints, arXiv:1601.07175

Naoz, S., & Fabrycky, D. C. 2014, ApJ, 793, 137

Nicholls, C. P., Melis, C., Soszyński, I., et al. 2013, MNRAS, 431, L33

Paumard, T., Genzel, R., Martins, F., et al. 2006a, ApJ, 643, 1011

—. 2006b, ApJ, 643, 1011

Pfalzner, S., Steinhausen, M., & Menten, K. 2014, ApJl, 793, L34

Pfuhl, O., Gillessen, S., Eisenhauer, F., et al. 2015, ApJ, 798, 111

Phifer, K., Do, T., Meyer, L., et al. 2013, ApJl, 773, L13

Ponti, G., De Marco, B., Morris, M. R., et al. 2015, ArXiv e-prints, arXiv:1507.02690

Prodan, S., Antonini, F., & Perets, H. B. 2015, ApJ, 799, 118

Ragland, S., Jolissaint, L., Wizinowich, P., & Neyman, C. 2014, in , 91480S–91480S–11

Rudy, R. J., Lynch, D. K., Russell, R. W., et al. 2008a, IAU Cirulars, 8976

—. 2008b, IAU Cirulars, 8997

Sana, H., & Evans, C. J. 2011, in IAU Symposium, Vol. 272, IAU Symposium, ed. C. Neiner, G. Wade, G. Meynet, & G. Peters, 474–485

Schartmann, M., Burkert, A., Alig, C., et al. 2012, ApJ, 755, 155

Schödel, R., Morris, M. R., Muzic, K., et al. 2011, Astronomy and Astrophysics, 532, A83

Schödel, R., Najarro, F., Muzic, K., & Eckart, A. 2010, Astronomy and Astrophysics, 511, A18

Schödel, R., Ott, T., Genzel, R., et al. 2003, ApJ, 596, 1015

—. 2002, Nature, 419, 694

Scoville, N., & Burkert, A. 2013, ApJ, 768, 108

Serivce, M., Lu, J. R., Campbell, R. D., et al. 2016, PASP

Shields, E. A. 2012, Opt. Lett., 37, 2463

Sitarski, B., Do, T., Witzel, G., et al. 2014, in American Astronomical Society Meeting Abstracts, Vol. 223, American Astronomical Society Meeting Abstracts #223, 238.05

Sitarski, B. N., Morris, M. R., Lu, J. R., et al. 2013, ApJ, 770, 134

Sitarski, B. N., Witzel, G., & et al. 2016, In Preparation

Sitarski, B. N., Witzel, G., Fitzgerald, M. P., et al. 2014, in Society of Photo-Optical Instrumentation Engineers (SPIE) Conference Series, Vol. 9148, 91486T–91486T–9

Sitarski, B. N., Witzel, G., Lu, J. R., et al. 2016, in Society of Photo-Optical Instrumentation Engineers (SPIE) Conference Series, Vol. 9909, Society of Photo-Optical Instrumentation Engineers (SPIE) Conference Series

Stephan, A., Naoz, S., & et al. 2016, In Preparation

Stolte, A., Morris, M. R., Ghez, A. M., et al. 2010, ApJ, 718, 810

Stolte, A., Hußmann, B., Morris, M. R., et al. 2014, ApJ, 789, 115

Tielens, A. G. G. M., McKee, C. F., Seab, C. G., & Hollenbach, D. J. 1994, ApJ, 431, 321

Tokunaga, A. T. 2000, Infrared Astronomy, ed. A. N. Cox, 143

Trippe, S., Gillessen, S., Gerhard, O. E., et al. 2008, Astronomy and Astrophysics, 492, 419

Tylenda, R., Hajduk, M., Kamiński, T., et al. 2011, Astronomy and Astrophysics, 528, A114

Tylenda, R., Kamiński, T., Udalski, A., et al. 2013, Astronomy and Astrophysics, 555, A16

Valencia-S., M., Eckart, A., Zajaček, M., et al. 2015, ApJ, 800, 125

van Dam, M. A., Le Mignant, D., & Macintosh, B. A. 2004, Applied Optics, 43, 5458

van Dam, M. A., Sasiela, R. J., Bouchez, A. H., et al. 2006, in Society of Photo-Optical Instrumentation Engineers (SPIE) Conference Series, Vol. 6272, Society of Photo-Optical Instrumentation Engineers (SPIE) Conference Series

Williams, M. J., Bureau, M., & Cappellari, M. 2010, MNRAS, 409, 1330

Witzel, G., Lu, J. R., Ghez, A. M., et al. 2012a, in Society of Photo-Optical Instrumentation Engineers (SPIE) Conference Series, Vol. 8447, Society of Photo-Optical Instrumentation Engineers (SPIE) Conference Series, 24

Witzel, G., Eckart, A., Bremer, M., et al. 2012b, ApJs, 203, 18

Witzel, G., Ghez, A. M., Morris, M. R., et al. 2014, ArXiv e-prints, arXiv:1410.1884

Wizinowich, P. L., Chin, J., Johansson, E., et al. 2006, in Society of Photo-Optical Instrumentation Engineers (SPIE) Conference Series, Vol. 6272, Society of Photo-Optical Instrumentation Engineers (SPIE) Conference Series

Yelda, S., Ghez, A. M., Lu, J. R., et al. 2014, ApJ, 783, 131

Yelda, S., Lu, J. R., Ghez, A. M., et al. 2010, ApJ, 725, 331